Model Improvement for SAR Altimetry

Heft 55
Schriftenreihe der Fachrichtung Geodäsie
Fachbereich Bau- und Umweltingenieurwissenschaften
Technische Universität Darmstadt
ISBN 978-3-935631-44-0

Darmstadt, September 2019

TECHNISCHE
UNIVERSITÄT
DARMSTADT

Heft 55

Darmstadt, September 2019

Christopher Buchhaupt

Model Improvement for SAR Altimetry

Schriftenreihe
Fachrichtung Geodäsie
Fachbereich Bau- und Umweltingenieurwissenschaften
Technische Universität Darmstadt

ISBN 978-3-935631-44-0

Schriftenreihe Fachrichtung Geodäsie der Technischen Universität Darmstadt

Online unter: http://tuprints.ulb.tu-darmstadt.de/id/eprint/9015
URN: urn:nbn:de:tuda-tuprints-90156

Verantwortlich für die Herausgabe der Schriftenreihe:

Der Sprecher der Fachrichtung Geodäsie
im Fachbereich Bau- und Umweltingenieurwissenschaften
der Technischen Universität Darmstadt

Bezugsnachweis:

Technische Universität Darmstadt
Institut für Geodäsie
Franziska-Braun-Str. 7
64287 Darmstadt

ISBN: 978-3-935631-44-0

Model Improvement for SAR Altimetry

Vom Fachbereich Bau- und Umweltingenieurwissenschaften
der Technischen Universität Darmstadt
zur Erlangung des akademischen Grades eines
Doktor-Ingenieurs (Dr.-Ing.) genehmigte Dissertation

vorgelegt von
Christopher Buchhaupt
aus Seeheim-Jugenheim

Referent: Prof. Dr.-Ing. Matthias Becker
1. Korreferent: P.D. Dr.-Ing. habil. Luciana Fenoglio-Marc
2. Korreferent: Prof. Dr. Chris Ray
Tag der Einreichung: 22. January 2019
Tag der mündlichen Prüfung: 15. March 2019

Darmstadt - D17

Acknowledgements

First and foremost, I want to thank my Ph.D. advisor, Professor Dr.-Ing. Matthias Becker, for his guidance and his support during the last months of the finishing process. Otherwise, I would had difficulties to finish the thesis in time. I always enjoined our strategy meetings, which helped me a lot to keep on track.

I also want to thank my mentor, P.D. Dr.-Ing habil. Luciana Fenoglio-Marc, who introduced me to the scientific community of radar altimetry. She helped me a lot with her comments and questions to improve this thesis with respect to scientific claims, completeness and clearness.

Special thanks go to Professor Dr. Chris Ray who has thankfully volunteered to be part of the examination board and to undertake the travel to Darmstadt to personally attend the disputation. His comments made it possible to identify last errors, which could therefore be corrected in time.

Additionally, I want to thank my colleagues at PSG TU Darmstadt. The meetings and coffee breaks were always interesting and a lot of fun. It was a pleasure to work with all of you and I hope we manage to keep in touch.

Last but not least, I want to thank my close family, namely my parents Holger and Brigitte Buchhaupt, my sister Isabelle Zimmermann, my uncle Klaus Forster and my grandmother Mathilde Gertrude Forster, who always mentally supported me.

Zusammenfassung

Während der letzten Jahrzehnte wurde Radar Altimetrie zu einem wichtigen Werkzeug für die Beobachtung der Meeresoberfläche bezüglich der Höhe der Meeresoberfläche und des Seegangs. Seit dem Start der CryoSat-2 Mission existiert eine neue Technik, namens SAR Altimetrie, welche das Signal zu Rauschverhältnis der gewonnenen geophysikalischen Parameter verbessert und durch den kleineren Footprint entlang des Tracks ist eine bessere Performanz in Küstennähe erreichbar. In den letzten Jahren wurden mehrere neue Prozessierungsmöglichkeiten entwickelt und getestet wie reduziertes SAR (RDSAR), der Modus geringer räumlicher Auflösung mit angebrachter Streckenmigrationskorrektur (LRMC) und voll fokussiertes SAR um das Potential dieser neuen Technik voll auszunutzen. Das Ziel dieser Studie ist es, die Schätzung geophysikalischer Parameter zu verbessern durch die Entwicklung eines neuen Stapel- und Wellenformmodels, welches in der Lage ist eine allgemeinere Meeresoberflächendarstellung zu berücksichtigen und zusätzlich Vertikalbewegungen der Wellenpartikel mit einbezieht. Dieses neue Model wird in verschiedenen Retrackingschemata implementiert, um zu untersuchen wie die gewonnenen geophysikalischen Parameter sich in Bezug auf Präzision und Genauigkeit verhalten.

Es wird gezeigt, dass eine 20 Hz SAR Prozessierung, welche in offiziellen Level 2 Datensätzen verwendet wird, eine Unterabtastung der Meeresoberfläche verursacht und dass eine Abtastrate von 40 Hz in einem geringeren pinken Grundrauschen resultiert und die Präzision der gewonnenen geophysikalischen Parameter sich verbessert. Auf der anderen Seite profitieren die anderen zwei alternativen Prozessierungsmodi LRMC und RDSAR nicht von einer höheren Abtastrate.

Ein weiterer Beitrag dieser Arbeit ist die Untersuchung des Einflusses von Oberflächensteigungen und Krümmungen auf RDSAR, LRMC und unfokussierter SAR Prozessierung. Es kann zusammengefasst gesagt werden, dass der Einfluss dieser Größen auf RDSAR und SAR gering ist, während in LRMC systematische Fehler in der geschätzten signifikanten Wellenhöhe von bis zu drei Metern und in der geschätzten Meereshöhe Fehler zwischen minus zwanzig und plus zwanzig Zentimetern auftreten. Auf der anderen Seit ist LRMC in der Lage konsistente und präzise Parameter zu liefern, wenn Steigungen und Krümmungen der Oberfläche korrekt berücksichtigt werden.

Im letzten Teil dieser Arbeit wird gezeigt, dass die Standardabweichung der vertikalen Wellenbewegung ein schätzbarer Parameter ist, der eine hohe Korrelation zu Modell und In-Situ-Daten aufweist. Zusätzlich reduziert eine Einbringung dieses Parameters in das Retracking die Inkonsistenz zwischen RDSAR und SAR geschätzten signifikanten Wellenhöhen für hohe Seegänge, welche bisher zwanzig Zentimeter betrug. Allerdings treten bei signifikanten Wellenhöhen kleiner als zwei Meter zusätzliche Differenzen in der Meeresspiegelhöhe von bis zu sieben Zentimeter und in der signifikanten Wellenhöhe von bis zu einem Meter auf. Dies bedeutet, dass immer noch ein Verbesserungsbedarf vorhanden ist für kleine Wellenhöhen, welche in weiteren Studien behandelt werden sollten.

Abstract

During recent decades, radar altimetry has become an important tool to observe the sea surface with respect to sea level and sea state. Since the launch of CryoSat-2, a new technique called SAR altimetry has improved the signal-to-noise ratio of retrieved geophysical parameters and due to the smaller along-track footprint a better performance in coastal zones is reached. In the recent years, several new processing modes have been developed and tested to improve the understanding of this new technique, such as reduced SAR (RDSAR), low resolution mode including range cell migration correction (LRMC) and fully-focused SAR processing. The scope of this work is to improve the retrieval of geophysical parameters by developing a new stack and waveform model capable of including a more general sea surface representations such as the geoid and introducing vertical wave particle motion. This new model will be included in different retracking schemes to investigate accuracy and precision of the retrieved geophysical parameters.

It is shown that 20 Hz SAR processing, which is used in the official level two data products, results in an aliasing of the sea surface and that a surface sampling rate of 40 Hz yields a lower pink noise floor and more precise retrieved parameters. The other two considered processing modes RDSAR and LRMC do not benefit from a higher sampling rate.

Another contribution of this work is to investigate of possible effects of sea surface slopes and curvatures on RDSAR, LRMC and unfocused SAR processing. It can be concluded that the impact of these quantities is small in RDSAR and SAR processing, whereas in LRMC processing significant wave height biases up to three metres and sea level biases between minus twenty and plus twenty centimetres can occur if the surface slopes and curvatures are not considered correctly in the signal processing and parameter retrieval process. On the other hand, LRMC estimates geophysical parameters consistent to the other two considered processing modes with a precision better than unfocused SAR.

In the final part, it will be shown that the standard deviation of vertical wave particle velocities is an estimable parameter with a high correlation with respect to model and in-situ data. Additionally, considering this geophysical parameter in the retracking can lead to consistent wave height estimations with RDSAR at high sea states. This was an open issue given that mean differences up to twenty centimetres occurred between these two processing modes. However, at small sea states the accuracy is poor due to differences in significant wave height up to one metre and sea level differences up to seven centimetres. This means that there remains a need for further improvements between zero to two metres significant wave heights, which needs to be addressed in further studies.

Contents

List of Tables

List of Symbols

Latin Symbols

A estimated amplitude of the waveform.

a_e semi major axis of the reference ellipsoid.

B PTR bandwidth.

b_e semi minor axis of the reference ellipsoid.

c speed of light.

$\bar{C}_{mn}$ fully-normalized cosine spherical harmonics coefficients.

D length of the synthetic antenna.

f_B burst repetition frequencye.

f_c central frequency of emitted pulse.

f_D Doppler frequency.

f_p pulse repetition frequency.

f_r frequency component of range compression Fourier transform.

g norm of the gravitational acceleration vector.

G antenna gain function.

g_0 tracker reference gate.

G_0 nominal antenna gain.

GM gravity mass constant.

h_s platform altitude with respect to the reference surface.

h_{mss} mean sea surface level with respect to the reference surface.

h_N nominal orbit altitude above reference ellipsoid.

H_s significant wave height.

h_{SSH} sea surface height with respect to the reference surface.

K average Gaussian curvature within a finit surface area.

$M_k^{(\Omega)}$ k'th order absolute moment of the one sided frequency spectrum.

$M_k^{(K)}$ k'th order absolute moment of the one sided wavenumber spectrum.

N geoid undulation.

n_A average number of scatterers within a finit surface area.

N_p numper of pulses per burst.

N_s numper of samples per echo.

N_t time delay window widening factor.

N_x azimuth window widening factor.

P_X vector containing retracking output.

r euclidean distance between the platform centre of mass and a scattering surface element.

R_c nominal local earth curvature radius.

r_{trk} distance associated with the reference gate of the retrieved waveform at burst 0.

R retracked distance between the satellite and the sea level.

s chirp slope.

s sea surface slope vector.

s_k modelled waveform sample with index k.

$\bar{S}_{mn}$ fully-normalized sine spherical harmonics coefficients.

$S_{\eta\eta}$ wavenumber-frequency spectra of the sea surface elevation.

s_o^2 mean square sea surface slope.

t time.

t_0 time difference between the tracking gate and the point of closest approach.

T_{01} mean wave period.

T_{02} mean zero up-crossing wave period.

T_{24} mean peak to peak wave period.

t_f fast time.

t_s slow time.

V gravity potential.

V_0 gravity potential of the reference ellipsoid.

v_h vertical velocity component perpendicularly to the reference surface.

v_N nominal magnitude of satellite velocity.

v_p velocity component in the direction of the maximum curvature.

v_q velocity component in the direction of the minimal curvature.

$v_r(t_s)$ relative velocity between the platform and the scattering surface element.

v_s horizontal velocity component of the satellite with respect to the reference surface.

v_x along-track velocity component parallel to the reference surface.

x along-track coordinate of a scattering surface element.

x_D along-track coordinate of focused point minus along track surface slope shift.

x_s along-track satellite corrdinate at t_s=0.

y across-track coordinate of a scattering surface element.

y_k measured waveform sample with index k.

z realization of the elevation of a wave particle at an epoch t and position x,y.

z_t realization of the vertical velocity of a wave particle at an epoch t and position x,y.

z_{tt} realization of the vertical acceleration of a wave particle at an epoch t and position x,y.

z_x realization of the partial derivative of the sea surface elevation in upwind direction.

z_{xx} realization of the second-order partial derivative of the sea surface elevation in upwind direction.

z_{xy} realization of the mixed partial derivative of the sea surface elevation in upwind and crosswind direction.

z_y realization of the partial derivative of the sea surface elevation in crosswind direction.

z_{yy} realization of the second-order partial derivative of the sea surface elevation in crosswind direction.

α_0 auxiliary variable releated with the mean square surface slope.

α spherical curvature coefficient.

α_x along-track curvature coefficient.

α_{xy} mixed curvature coefficient.

α_y across-track curvature coefficient.

γ_0 normal gravity.

Δ_h height error due to surface slopes.

Δh_{corr} range offset caused by geophysical and atmospheric effects.

Δh_{app} range offset caused by geophysical and atmospheric effects applied for validation with tide gauge.

Δh_{iono} height offset caused by ionospheric path delay.

Δh_{dry} height offset caused by dry tropospheric path delay.

Δh_{wet} height offset caused by wet tropospheric path delay.

Δh_{set} height offset caused by solid earth tides.

Δh_{pole} height offset caused by pole tides.

Δh_{load} height offset caused by ocean loading tides.

Δh_{ssb} height offset caused by the sea state bias.

ΔR reference frame range offset of the satellite.

η Random variable of the elevation of a wave particle at an epoch t and position x,y.

η_t Random variable of the vertical velocity of a wave particle at an epoch t and position x,y.

η_{tt} Random variable of the vertical acceleration of a wave particle at an epoch t and position x,y.

η_x Random variable of the partial derivative of the sea surface elevation in upwind direction.

η_{xx} Random variable of the second order partial derivative of the sea surface elevation in upwind direction.

η_{xy} Random variable of the mixed partial derivative of the sea surface elevation in upwind and crosswind direction.

η_y Random variable of the partial derivative of the sea surface elevation in crosswind direction.

η_{yy} Random variable of the second order partial derivative of the sea surface elevation in crosswind direction.

θ polar angle of the antenna coordiante system.

θ_i incidence angle of electromagnetic wave.

Θ_{3dBx} half power beamwidth along-track.

Θ_{3dBy} half power beamwidth across-track.

κ_1 maximal principal curvature.

κ_2 mimimal principal curvature.

λ longitude of an ellipsoidal coordinate system.

λ_c carrier wavelength of the transmitted pulse.

μ integral measure of wave steepness.

ξ_r roll mispointing angle.

ξ_p pitch mispointing angle.

ξ_y yaw mispointing angle.

ϱ autocorrelation function of the sea surface elevation.

σ_z standard deviation of the wave particle elevation.

σ_v standard deviation of the vertical wave particle velocity.

σ_a standard deviation of the vertical wave particle acceleration.

σ_0 radar cross section at nadir.

σ^0 radar cross section function.

σ_s estimated parameter related with the significant wave height.

σ_t estimated parameter related with the standard deviation of the vertical velocities of scattering surface elements.

σ_{tt} estimated parameter related with the standard deviation of the vertical accelerations of scattering surface elements.

σ_x standard deviation of the sea surface slopes in upwind direction.

σ_y standard deviation of the sea surface slopes in crosswind direction.

τ_b burst duration.

τ_p pulse duration.

τ_r time delay.

τ_u usable pulse length.

φ latitude of an ellipsoidal coordinate system.

φ_d depression angle.

ω azimuth angle of the antenna coordiante system.

E expected value: $E[f(X)] = \int_{-\infty}^{\infty} f(x)p(x)dx$, with X being a random variable, f a measurable function of X and p the probability density function of X.

Cov covariance: $Cov[X,Y] = E[XY] - E[X]E[Y]$, with X and Y being random variables.

Var variance: $Var[X] = E[X^2] - E[X]^2$, with X being a random variable.

erf error function: $\operatorname{erf}(x) = \frac{2}{\sqrt{\pi}} \int_{-\infty}^{x} e^{-t^2} dt$.

sinc normalized sine cardinale function: $\operatorname{sinc}(x) = \dfrac{\sin(\pi x)}{\pi x}$.

$\sqcap$ rectangular pulse: $\sqcap(x) = \begin{cases} 1 & \text{, if } |x| < 1/2 \\ 0 & \text{, else} \end{cases}$.

U heaviside step function: $U(x) = \begin{cases} 1 & \text{, if } x \geq 0 \\ 0 & \text{, else} \end{cases}$.

sgn signum function: $sgn(x) = \begin{cases} 1 & \text{, if } x \geq 0 \\ -1 & \text{, else} \end{cases}$.

$\bigwedge$ triangular pulse: $\bigwedge(x) = \begin{cases} 1 - |x| & \text{, if } |x| < 1 \\ 0 & \text{, else} \end{cases}$.

AGC Automatic Gain Control

CA Conventional Altimetry

CF Characteristic Function

cpkm cycles per kilometre

DDA Delay Doppler Altimetry

ECMWF European Centre for Medium-Range Weather Forecasts

EIGEN European Improved Gravity model of the Earth by New techniques

ESA European Space Agency

ESRIN European Space Research Institute

FBR Full Bit Rate

FFT Fast Fourier Transform

FSSR Flat Sea Surface Response

G-POD Grid Processing on Demand

GNSS Global Navigation Satellity System

GSHHG Global Self-consistent, Hierarchical, High-resolution Geography Database

ICGEM International Centre for Global Earth Models

LRM Low Resolution Mode

LRMC Low Resolution Mode with Range Cell Migration Correction

MSS Mean Sea Surface

NaN Not a Number

NEA North East Atlantic

PDF Probability Density Function

PRF Pulse Repetition Frequency

PSD Power-Spectral-Density

PTR Point Target Response

RAM Random-Access Memory

RADS Radar Altimeter Data System

RIP Range Integrated Power

RMC Range Migration Correction

RDSAR Reduced SAR Altimetry

SAMOSA SAR Altimetry Mode Studies and Applications over Ocean, Coastal Zones and Inland Water

SAR Synthetic-Aperture Radar

SINC Signal Model involving fast Numerical Convolutions

SINC2 SINC based conventional altimetry retracker

SINCS SINC based unfocused SAR altimetry retracker

SINCS-OV SINC based unfocused SAR altimetry retracker including orbital velocities of wave particles

SLA Sea Level Anomaly

SNR Signal-to-Noise-Ratio

SSH Sea Surface Height

SWH Significant Wave Height

ZSK Zero Skewness

1 Introduction

Over the last 25 years, radar altimetry has become an important tool to better understand the sea surface by providing information about sea level, wave height and wind speed. CryoSat-2, which was launched in April 2010, is the first mission of a new generation of space-borne altimeters capable of transmitting phase coherent pulses with a high Pulse Repetition Frequency (PRF) allowing delay Doppler processing. This technique, called Delay Doppler Altimetry (DDA) - first mentioned by Raney [1998] - is based on forming a synthetic antenna with length D out of a discrete antenna array using the Fourier transform method, also referred to as beam shaping (see Balanis [2005, Section 7.4]). There are two main benefits in Synthetic-Aperture Radar (SAR) altimetry.

1. The footprint size is that from the formed beams instead of the whole pulse, giving a higher spatial resolution when these beams are focused to dedicated surface locations.

2. A higher signal-to-noise ratio of the retrieved waveform is achievable, resulting in more precise estimated geophysical parameters.

The along-track spatial resolution depends on orbital altitude, platform velocity and the length of the synthetic antenna D where this quantity is chosen in state-of-the-art processing that the illuminated surface is located in the far field of the signal fulfilling $r > \frac{D^2}{\lambda_c}$ (see Balanis [2005, Section 2.2.4]). Here, r is the distance from the antenna to the surface and λ_c the wavelength of the emitted pulse. This processing scheme is called unfocused SAR. For longer synthetic antennas, additional phase terms need to be applied to compensate for the near field characteristic of the signal leading to fully-focused SAR processing (see Egido and Smith [2016]).

In the past, several processing techniques for DDA were developed for different applications such as

- Reduced SAR Altimetry (RDSAR), described in Smith and Scharroo [2015] as a proxy for Conventional Altimetry (CA) waveform processing in SAR mode. This mode is used as a reference to validate SAR mode data.

- Unfocused SAR as the standard processing mode, mentioned in Raney [1998].

- Fully focused SAR, described in Egido and Smith [2016] which synthesises a longer antenna to gain a higher along track resolution.

- LRMC, developed by Boy et al. [2017], which creates Doppler beams without focusing them to a dedicated surface location, leading to a pulse limited footprint size.

In this work, all processing modes are discussed, except fully-focused SAR, which needs knowledge about burst-to-burst phase differences gained by transponder overflies (see Egido and Smith [2016] for further details).

The focus of this work lies on how SAR altimetry can benefit detecting short- and large-scale geophysical signals in the open ocean. A new waveform model for both CA and DDA is introduced considering large-scale signals such as the spatial variability of geoid undulations and short-scale signals such as wave slopes and curvatures. Additionally, vertical wave particle velocities and accelerations of scattering sea surface elements are included in the Probability Density Function (PDF). This enables estimating second- and fourth-order spectral moments which is a novum as currently only the zeroth-order moment is retrieved by radar altimetry.

The whole processing starting with raw observations will be performed with version 1.4 of the TUDaBo FBR processor prototype (see Fenoglio and Buchhaupt [2017]), publicly available at the Grid Processing on Demand (G-POD) service run by European Space Agency (ESA). Although Sentinel-3A and B data is available, this study focuses on CryoSat-2 data only. However, all contributions presented in this work are kept general and are adaptable to other satellite missions.

In chapter 2, the theoretical background is discussed, distributed in three sections. Section 2.1 provides an overview of CA and SAR altimetry considering the different processing modes and transmitting schemes, whereby in section 2.2 the derivation of a locally best-fitting reference surface derived with elemental differential geometry is discussed. In this study, the geoid calculated by using the European Improved Gravity model of the Earth by New techniques (EIGEN)-6C4 spherical harmonics coefficients described in Förste et al. [2014] will be used as an approximation of the sea surface in open ocean, as it allows the analytical computation of spatial derivatives to order two and higher. The resulting manifold best approximating the local sea surface is given by a torus. Section 2.3 describes the stochastic representation of the sea surface displacement in space and time and how this affects radar altimetry waveforms.

In chapter 3, the derivation of a CA and SAR waveform model considering all of the effect discussed in chapter 2 is demonstrated by starting with the transmitting of phase coherent echoes from one burst. All processing steps that need to be considered in the model are analytically shown and discussed. Calibration steps such as pulse-to-pulse amplitude and phase corrections are not examined.

Chapter 4 provides an overview of the CryoSat-2 mission parameters used and the computation of the geophysical parameters of interest in this study. Additionally, the validation metrics are described.

Chapter 5 briefly discusses the surface sampling rate, which can be 20 Hz, 40 Hz and 80 Hz for CryoSat-2 RDSAR, LRMC and SAR waveforms. It will be shown that 40 Hz is the best choice for SAR to derive short-scale geophysical parameters as this frequency fulfils the Nyquist-Shannon sampling theorem (see Papoulis [1977, Section 5-1] for further information), whereas for RDSAR and LRMC 20 Hz surface sampling is sufficient.

The impact of geoid curvatures and slopes locally approximated by a best-fitting torus will be examined in chapter 6 by comparing the retracking results of RDSAR, LRMC and SAR waveforms in the area of the Marianna trench using the following local surface approximations

- A sphere that is widely used in radar altimetry as a surface approximation.
- A sphere whose origin is translated to account for surface slopes.
- A torus that approximates the geoid locally within the area of the altimeter footprint.

It will be shown how the estimated geophysical parameter differs for the different modes depending on along track curvature and slopes.

In chapter 7, the estimation of the second-order spectral moment related to the mean zero up-crossing wave period and the standard deviation of the vertical wave particle velocity is presented. This relationship is discussed in section 2.3. It will be shown how introducing this new parameter influences surface elevation, wave height and backscatter coefficient biases between the three considered processing modes. A validation of all four estimated parameters against the global European Centre for Medium-Range Weather Forecasts (ECMWF) wave model in the north east Atlantic and in-situ data coming from tide gauges and buoys is performed.

2 Theoretical Background

2.1 Conventional and Delay Doppler Altimetry

Covering approximately 71 % of the earth's surface, the oceans are an important habitat for many species and crucial for the ecological system. They are also a trading and transport route connecting the seven continents. However, the oceans underlie short- and long-term changes and variabilities such as climate warming, weather or crustal motions, making it necessary to observe these changes to gain a better understanding of oceanic processes. Some parameter characterizing these include the sea level height, statistical wave parameters such as the Significant Wave Height (SWH) and the wind. Whereas tide gauges and buoys provide information such as sea level height, statistics about waves and wind with a high temporal resolution and precision, the spatial resolution is limited by the density of the tide-gauge/buoy network. Space-borne radar altimetry missions aim to improve the global coverage of sea surface observations at the cost of a lower temporal resolution.

2.1.1 Principle of Conventional Altimetry and Delay Doppler Altimetry

The principle of radar altimetry is based on emitting micro wave frequency modulated pulses which are reflected by the sea surface, whereby the travel time of the signal is tracked. The following equations are based on the assumption that the reflecting surface is located in the far field. Analytically, an emitted chirp modulated pulse can be described as:

$$\chi(t) = \sqrt{G(\theta,\omega)}\exp\left\{2\pi i(f_c - \tfrac{1}{2}st)t\right\} \sqcap \left(\tfrac{t}{\tau_p}\right) \tag{2.1}$$

with G as the antenna gain function depending on the angles θ and ω in the spherical antenna coordinate system. f_c describes the central frequency, t the time, s the chirp slope, $\sqcap$ the rectangular impulse function and τ_p the pulse duration.

This pulse is reflected by a scatterer on the sea surface at a distance of r, where due to platform motion r is a function of time. Due to the law of energy conservation, the equation is divided by $2\sqrt{\pi}r$ to apply that the power over the whole transmitted pulse remains constant for each epoch (see chapter 5 in Klausing and Holpp [2000]).

The reflected pulse χ_r is then:

$$\chi_r(t) = \frac{\sqrt{G(\theta,\omega)\sigma^0(\theta,\omega)}}{2\sqrt{\pi}r}\exp\left\{2\pi i[f_c - \tfrac{1}{2}s(t-\tfrac{r}{c})](t-\tfrac{r}{c})\right\} \sqcap \left(\tfrac{t-r/c}{\tau_p}\right) \tag{2.2}$$

where σ^0 is the function describing how much intensity is reflected by a scattering surface element and c the speed of light.

This reflected signal is then received by the antenna again, which has switched from transmitting to receiving mode. Additionally, it is multiplied by a complex conjugate copy of the transmitted signal before it left the antenna. This technique is called chirp deramping (see Chelton et al. [1989]).

$$\begin{aligned} S(t) &= \frac{\lambda_c G(\theta,\omega)\sqrt{\sigma^0(\theta,\omega)}}{\sqrt{(4\pi)^3 r^2}}\exp\left\{2\pi i[f_c - \tfrac{1}{2}s(t-\tfrac{2r^*}{c})](t-\tfrac{2r^*}{c})\right\}\exp\left\{-2\pi i(f_c - \tfrac{1}{2}st)t\right\} \sqcap \left(\tfrac{t}{\tau_u}\right) \\ &= \frac{\lambda_c G(\theta,\omega)\sqrt{\sigma^0(\theta,\omega)}}{\sqrt{(4\pi)^3 r^2}}\exp\left\{2\pi i\left[\frac{2r^*}{c}s\left(t-\frac{r^*}{c}-\frac{f_c}{s}\right)\right]\right\} \sqcap \left(\tfrac{t}{\tau_u}\right) \end{aligned} \tag{2.3}$$

with $r^* = r - r_{trk}$ describing the difference of distance between the platform and scatterer and the tracking reference range r_{trk} and τ_u being the usable pulse length Chelton et al. [1989].

In the case of the Low Resolution Mode (LRM) being the processing mode in CA Eq. 2.3 would be sufficient, although for the unfocused SAR mode processing all pulses in one burst need to be considered. Figure 2.1 shows the transmitting and receiving pattern of CryoSat-2 using a closed burst transmission and receiving scheme.

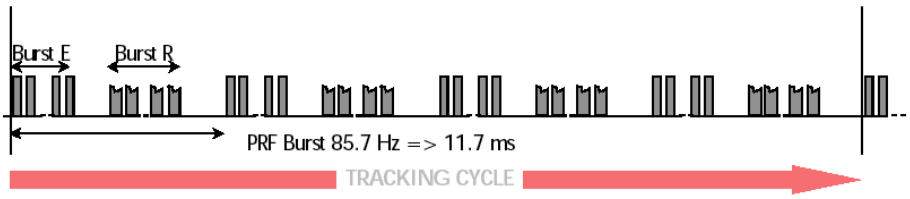

Figure 2.1: CryoSat-2 transmitting and receiving pattern [Rosmorduc et al., 2016, Figure 5.52]

CroySat-2 emits one full burst each containing 64 Ku-band pulses and changes afterwards to receiving mode. This is repeated four times as one tracking cycle. It is important to note that one tracking cycle always contains four bursts without any jumps or gaps. Sentinel-3 also operates in closed burst loops, whereby the only difference is that it is a dual frequency altimeter with one C-band pulse at the start and the end of each burst [Rosmorduc et al., 2016, Figure 5.53]. Contrary to this, in open burst mode the antenna switches after each pulse from transmitting to receiving mode [Rosmorduc et al., 2016, Figure 5.54]. This approach will be introduced in Jason-CS, allowing LRM and SAR processing together.

This can be introduced to Eq. 2.3 for one burst by defining two time scales. The fast time t_f gives the time within one pulse and the slow time t_s which gives the pulse-to-pulse epochs, leading to:

$$S(t_f, t_s) = \frac{\lambda_c G(\theta,\omega)\sqrt{\sigma^0(\theta,\omega)}}{\sqrt{(4\pi)^3 r^2}} \exp\left\{2\pi i \left[\frac{2r^*}{c} s\left(t_f + t_s - \frac{r^*}{c} - \frac{f_c}{s}\right)\right]\right\} \sqcap\left(\tfrac{t_f}{\tau_u}\right) \sqcap\left(\tfrac{t_s}{\tau_b}\right) \tag{2.4}$$

with τ_b the burst duration.

As the horizontal satellite motion does not significantly affect the range to the scatterer, it can be approximated by:

$$r \approx r(t_s) + v_r(t_s) t_f \tag{2.5}$$

with $v_r(t_s)$ being the relative velocity between the platform and the surface element.

Inserting Eq. 2.5 into Eq. 2.4 and ignoring small terms yields the basis for the waveform model derived in chapter 3:

$$S(t_f, t_s) \approx \frac{\lambda_c G(\theta,\omega)\sqrt{\sigma^0(\theta,\omega)}}{\sqrt{(4\pi)^3 r^2}} \exp\left\{2\pi i \left[\frac{2r(t_s) - 2r_{trk}}{c}(s t_f - f_c) - \frac{2v_r(t_s)}{\lambda_c} t_f\right]\right\} \sqcap\left(\tfrac{t_f}{\tau_u}\right) \sqcap\left(\tfrac{t_s}{\tau_b}\right) \tag{2.6}$$

This burst is onboard the satellite normalized in power by the Automatic Gain Control (AGC) loops, low-pass filtered and discretely equidistantly sampled. The uniformly spaced samples are defined by

$$\Re(S(m\Delta t_f, n\Delta t_s)) \quad \mapsto \quad \Re(S_{m,n}) = I_{m,n} \tag{2.7}$$

$$\Im(S(m\Delta t_f, n\Delta t_s)) \quad \mapsto \quad \Im(S_{m,n}) = Q_{m,n} \tag{2.8}$$

whereby $\Re$ describes the real part, $\Im$ the imaginary part, m and n being integer values and $I_{m,n}$ the in-phase and $Q_{m,n}$ the quadrature part. These quantities are stored onboard the satellite as level 0 data. This product is down-linked to the ground station where it is further processed. Table 2.1 provides an overview of the different product levels for CA and DDA data of CryoSat-2.

Product Type	User Distribution	Mode	Description
L0	No	CA	The average of 91 pulses in the range domain computed onboard the satellite.
		DDA	Multiple bursts containing 64 complex echoes each in fast- time domain.
L1A	YES	Both	L0 plus calibrated platform orientation and timing.
L1B	YES	CA	Calibrated L1A product.
		DDA	Calibrated multi-looked waveforms and orientation parameter.
L2	YES	Both	Geophysical parameter retrieved from L1B product.

Table 2.1: Overview of Cryosat-2 product levels for CA and DDA adapted from Cullen et al. [2007, Table 2-1]. From L1B to L2 data the table assumes the standard processing modes which are LRM for CA and unfocused SAR for DDA.

The backscattered power from one surface area, the distance between the platform and the scattering surface elements and their relative velocity are random variables discussed in section 2.3. However, it can be assumed that the number of backscattering elements is sufficiently large to justify normally-distributed samples due to the central limit theorem. The I/Q samples can then be described by two independent normally-distributed random variables with zero mean and variance $\sigma^2_{m,n}$ for each sample.

In order to retrieve a waveform, it is necessary to perform a range compression step, which is outlined for LRM in the following equations. All steps for unfocused SAR are discussed analytically in chapter 3. It is assumed that the echoes are already vertically aligned and calibrated. An overview for the calibration of CryoSat-2 data can be found in Scagliola and Fornari [2016].

First a Fast Fourier Transform (FFT) is performed in fast time direction:

$$\hat{S}_{k,n} = FFT(S_{m,n}) = FFT(I_{m,n} + iQ_{m,n}) \tag{2.9}$$

The waveform is formed afterwards by adding the squared real and imaginary parts and performing a summation over the slow time domain:

$$P_k = \sum_n Re(\hat{S}_{k,n})^2 + Im(\hat{S}_{k,n})^2 \tag{2.10}$$

The retrieval of geophysical parameters from a waveform is achieved by retracking, which comprises two parts.

1. A functional model describing the waveform depending on parameters such as time delay with respect to reference epoch t_0, SWH and the amplitude A.

2. An inversion algorithm including a stochastic model of the fitted waveform. In this work a normal distribution is assumed and a Levenberg-Marquardt algorithm is used as a solver of the inversion problem (see Marquardt [1963]).

The noise of radar altimetry waveforms follows a Gamma distribution with good approximation, although a Levenberg-Marquardt minimizer using a least squares approach assumes a normal distribution of the signal. This leads the minimization problem to find the minimum of the negative log-likelihood function for a multivariate normal distribution [Bjerhammar, 1973, Section 2.19]

$$\mathbf{P}_X \rightarrow \min_{\mathbf{P}_X} \sum_{k=1}^{N_s} (y_k - s_k)^2 \tag{2.11}$$

with N_s the number of considered waveform samples, y_k the measured waveform sample with index k and s_k the modelled waveform sample as a function of parameter vector $\mathbf{P}_X$.

Figure 2.2 shows an example of a processed oversampled RDSAR waveform (blue line) and the best fit found by the minimization algorithm (red line). Here, only 208 samples are considered as the first and last 24 bins are corrupted by aliasing caused by the low-pass filter.

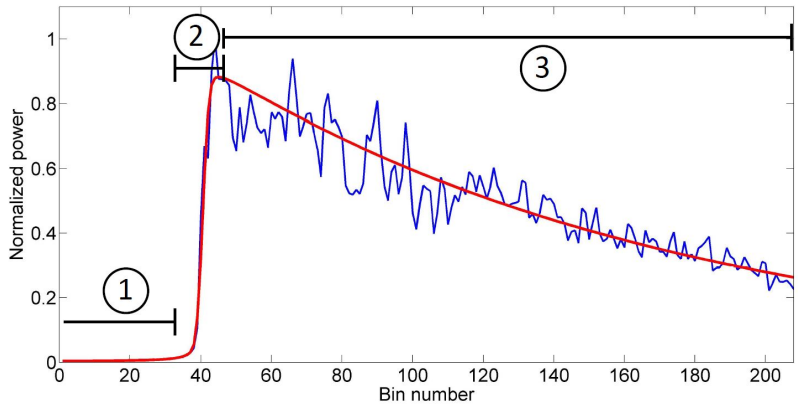

Figure 2.2: Retracking of a L1B waveform

As shown in Figure 2.2, a L1B waveform can be divided into three parts

1. The thermal noise area, which is dominated by additive sensor noise

2. The leading edge including the point of closest approach. Its width is related to the SWH and the maximum power with the estimated amplitude A.

3. The trailing edge mainly effected by the orientation of the antenna and the mean square slope which is discussed in section 2.3.

2.1.2 Considered Processing Modes

The available processing mode mainly depends on the mode in which the instrument is operating. Whereas in CA the whole L1B processing is performed onboard the satellite, in DDA only the deramping, low-pass filtering and sampling is performed. The complex echoes are then transmitted and further processed at the ground station to level 1A, which gives the level 0 data plus calibrated platform orientation and timing. This data is distributed to user communities, which can apply their own processing schemes to generate L1B, L2 and higher level data.

The main difference between CA and DDA is the PRF used where for CryoSat-2 CA the PRF is 1.971 kHz, it is 18.182 kHz for DDA. The reason behind this is located in the Walsh limit (see Walsh [1982]) giving that for CryoSat-2 LRM the upper bound for the PRF is approximately 2.000 kHz for SWH of 2m (more details can be found in Smith [2011]). This means that for SWH < 2 m increasing the PRF will not result in a higher signal-to-noise ratio, whereas for larger waves it does, albeit with a different upper bound for the PRF. This also applies for unfocused SAR, although the upper bound is higher than for LRM (see Giles et al. [2013]).

Another difference is that for SAR mode it is necessary to have phase coherent pulses or at least the phase differences between them needs to be known; otherwise, the azimuth FFT would result in erroneous beams. This requirement does not apply for LRM.

In DDA several processing modes are available, whereas in CA the whole waveform processing is performed onboard which leaves no choice for users. The three considered SAR modes in this work are RDSAR, Low Resolution Mode with Range Cell Migration Correction (LRMC) and unfocused SAR, which are described in the following parts.

The main difference in the processing modes lies in the footprints shown in Figure 2.3. While RDSAR behaves like LRM, LRMC and SAR form Doppler cells along-track by using the Doppler effect. This means that for LRM the illuminated area evolves in annuli of equal area after the maxima is reached whereas in SAR the footprint evolves within each beam, as highlighted by the green area in the right of Figure 2.3. The darker parts in both sides give the maximal area illuminated which is achieved when the whole pulse length first reached the sea surface (see Chelton et al. [1989]).

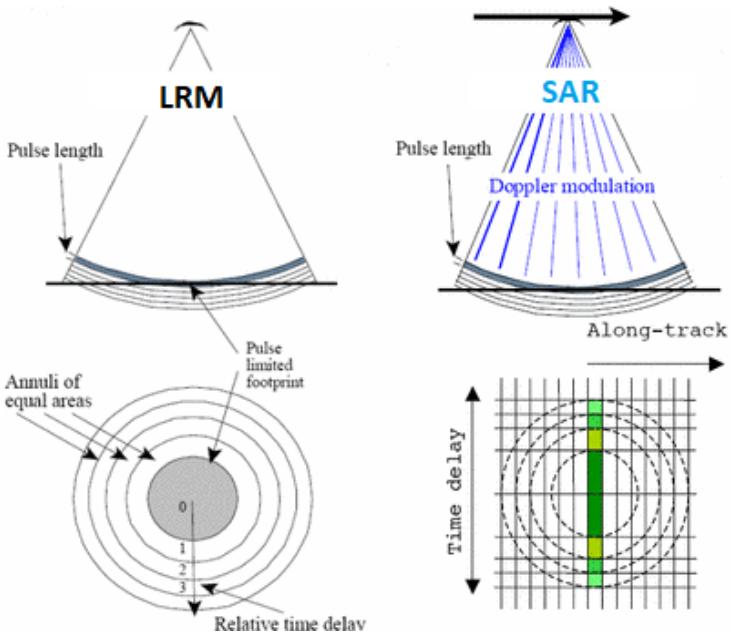

Figure 2.3: Different illuminated areas for LRM and SAR, adapted from [Rosmorduc et al., 2016, Figure 5.21]

RDSAR

The RDSAR mode describes the use of a LRM processing scheme in SAR mode which due to the gaps between consecutive bursts leads to a lower signal-to-noise-ratio as fewer pulses are transmitted and received compared with LRM. This processing mode is therefore necessary as a validation reference for SAR as LRM like waveforms are very well known by the scientific community for over 25 years.

The processing can be divided into three steps which are described in detail in Fenoglio and Buchhaupt [2017]

1. Calibration of the complex echoes of each burst
2. Horizontal and vertical alignment of the pulses
3. Range compression and incoherent averaging of all pulses

This results in RDSAR waveforms, which can afterwards be retracked to retrieve geophysical parameters. Although this processing scheme is only a proxy for real LRM, it behaves in the same way in terms of the illuminated area and sensitivity to geophysical effects. Accordingly, it is possible to retrack these waveforms with state-of-the-art CA waveform models.

Unfocused SAR and LRMC

The main idea of SAR processing is to form Doppler beams to increase the spatial resolution and the signal-to-noise-ratio [Skolnik, 2008, Chapter 21]. This is based on the Doppler effect, given that a frequency shift f_D applies due to relative velocities between two objects $v_r(t_s)$ [Skolnik, 2008, Section 14.2]

$$f_D = \frac{2v_r(t_s)}{\lambda_c} \tag{2.12}$$

Assuming a frozen sea surface, each Doppler frequency f_D can be related to an along-track coordinate x_D by using $v_r(t_s) = v_s \sin\varphi_d$ and $\sin\varphi_d \approx \frac{x_D}{h}$, which leads for a bent surface to

$$x_D = \frac{ch}{2\alpha_x f_c v_x} f_D \tag{2.13}$$

with depression angle φ_d, h_s the platform altitude with respect to the reference surface, v_s the horizontal satellite velocity with respect to the reference surface, $v_x = \frac{v_s}{\alpha_x}$ the along-track velocity component of the satellite and α_x the along-track curvature coefficient, which will be defined in chapter 3 Eq. 3.40. Note that in Eq. 2.13 it is assumed that the vertical velocity of the satellite is zero.

Assuming phase coherent echoes, it is possible to transform a burst from slow time t_s to Doppler frequency f_D domain using Fourier transforms. Accordingly, for each along-track position the backscattered power is retrievable. However, the achievable spatial resolution for unfocused SAR is limited by the length of the synthetic antenna, which in turn is limited by the far field relation. This will be discussed in chapter 5.

In the Doppler beam-forming process there are two possibilities which are outlined in Figure 2.4

1. SAR: Steer the beams to dedicated surface location. This means that from each burst one Doppler beam is steered to a location with known coordinates outlined in Figure 2.4b.
2. LRMC: Calculate the FFT only. This gives the Doppler fan of one burst, which will not be steered (see Figure 2.4a).

In both cases afterwards a Range Migration Correction (RMC) is applied to vertically align all the beams. Whereas in SAR processing the range migration is well known as the surface location is fixed and platform positions are determined

precisely, this is not the case for LRMC, where only the central position is known. This means that spatial information about the neighbourhood of this position is necessary to apply the RMC correctly (see chapter 6).

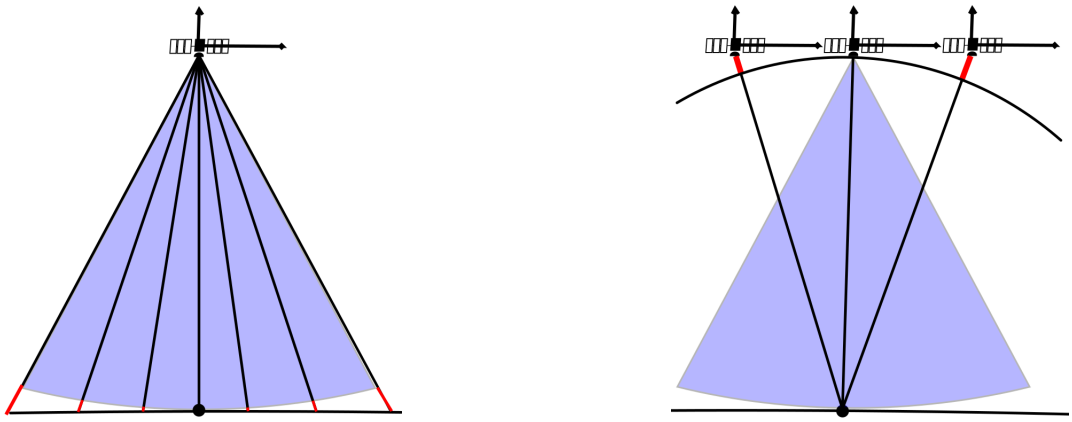

(a) LRMC case (b) SAR case

Figure 2.4: Geometrical principle of LRMC and SAR beam-forming and range cell migration correction (highlighted in red). The arrows describe the vertical and horizontal velocity components and the satellites represent burst locations. The black filled circle gives the central burst location projected onto the sea surface.

The following enumeration provides an overview of the processing steps to calculate unfocused SAR waveforms. Of course, it is possible to stop the processing after the stacking step, which gives the stack as an output (referred as L1B-S).

1. Calibrate echoes of each burst
2. Calculate Doppler frequencies associated with dedicated surface locations
3. Align bursts vertically and horizontally
4. Perform azimuth Fourier transform
5. Apply range cell migration correction and perform range compression
6. Stack the beams and calculate the waveform by multi-looking

A detailed analytical step-by-step processing scheme is shown in chapter 3. The pros and cons of both modes will be discussed in chapter 5.

2.2 Local Description of the Earth Surface

Over the last 25 years the illuminated sea surface has mostly been considered as a sphere, although in Sandwell and Smith [2014] it was shown that surface slopes can contribute to significant errors in radar altimetry sea level estimations. This error Δ_h can be quantified by using the squared L2-norm of the surface slope vector with respect to the reference ellipsoid $\mathbf{s}$ as

$$\Delta_h = \frac{\|\mathbf{s}\|_2^2 h_s}{2} \tag{2.14}$$

where Δ_h needs to be subtracted from the sea surface height to correct it.

As Sandwell and Smith [2014] consider geometrical effects of slopes on CA estimated surface heights, it is necessary to extend this study to LRMC and SAR processing modes. For the sake of completeness, not only slopes but also

curvatures are examined. These quantities will also be included in the L1B processing and the waveform model.

This section is divided in two parts. First, an introduction to elemental differential geometry is provided, including how it can be used to find a good local surface approximation. Second, the geoid that will be used to describe the sea surface on a global scale is used as an input to the derived algorithm.

2.2.1 Introduction to Elemental Differential Geometry

The formulas and notations in this section are based on chapter 3 of Patrikalakis [2002]. They are adapted to be used for remote sensing applications such as radar altimetry.

To use differential geometry for a manifold, it is required to be regular, meaning that the following applies

1. For every point on the surface, one smooth projection F from an open subset $\mathbf{V} \in \mathbb{R}^3$ to $\mathbf{U} \in \mathbb{R}^2$ exists.

2. F and its inversion are continuous.

3. $\mathbf{U}$ and $\mathbf{V}$ are linearly independent from each other.

These conditions apply for most surfaces that are at least two times steadily differentiable and do not self-intersect.

Following the earth surface $\mathbf{S} \subset \mathbb{R}^3$ being regular, it is possible to describe a small surface element $\mathbf{dS} \in \mathbf{S}$ around a point $\mathbf{X} \in \mathbf{S}$ with elemental differential geometry by using the first and second fundamental form. The idea behind this is to transfer the measure of distances and angles or position depended length characteristics into a two-dimensional sub-manifold.

In geodesy, an ellipsoidal coordinate system (h_s, λ, φ) is chosen to describe positions $\mathbf{X}$ by:

$$X_1 = (N_\varphi + h)\cos\varphi\cos\lambda \tag{2.15}$$
$$X_2 = (N_\varphi + h)\cos\varphi\sin\lambda \tag{2.16}$$
$$X_3 = (\tfrac{b^2}{a^2}N_\varphi + h)\sin\varphi \tag{2.17}$$

Accordingly, the earth surface can be described as a regular surface by introducing a dependency of $h(\lambda, \varphi)$. The tangential plane $\mathbf{T}_p$ at a point $\mathbf{p} \in \mathbb{R}^2$ is then:

$$\mathbf{T}_p(u, v) = \mathbf{X}(\mathbf{p}) + u\mathbf{X}_\lambda(\mathbf{p}) + v\mathbf{X}_\varphi(\mathbf{p}) \tag{2.18}$$

with $\mathbf{X}_\lambda$ the partial derivative of $\mathbf{X}(\lambda, \varphi)$ by λ and $\mathbf{X}_\varphi$ respectively. Its normalized normal vector $\mathbf{n} \in \mathbb{R}^3$ pointing to the centre of curvature is then:

$$\mathbf{n} = \frac{\mathbf{X}_\varphi \times \mathbf{X}_\lambda}{\|\mathbf{X}_\varphi\|_2 \cdot \|\mathbf{X}_\lambda\|_2} \tag{2.19}$$

To describe the geometry $\mathbf{dS}$. it holds interest how the direction of $\mathbf{n}$ changes after travelling a distance $s \in \mathbb{R}$ in direction $\mathbf{t} \in \mathbb{R}^2$ on $\mathbf{dS}$. This is described by the normal curvature κ_n whose extreme values also called principal curvatures are defined to be the eigenvalues of the shape operator $\mathbf{S}_p$ by

$$\kappa_{1,2} = \tfrac{S_{1,1}+S_{2,2}}{2} \pm \sqrt{\tfrac{(S_{1,1}+S_{2,2})^2}{4} - S_{1,1}S_{1,2} + S_{1,2}S_{2,1}} \tag{2.20}$$

with κ_1 the maximal curvature, κ_2 the minimal curvature and

$$\mathbf{S}_p = \begin{pmatrix} S_{1,1} & S_{1,2} \\ S_{2,1} & S_{2,2} \end{pmatrix} = \frac{1}{EG - F^2} \begin{pmatrix} LG - MF & MG - NF \\ ME - LF & NE - MF \end{pmatrix} \tag{2.21}$$

where the parameters E, F, G belong to the first fundamental form computed with

$$E = \mathbf{X}_\varphi \cdot \mathbf{X}_\varphi \tag{2.22}$$
$$F = \mathbf{X}_\lambda \cdot \mathbf{X}_\varphi \tag{2.23}$$
$$G = \mathbf{X}_\lambda \cdot \mathbf{X}_\lambda \tag{2.24}$$

and L, M, N to the second fundamental form

$$L = \mathbf{n} \cdot \mathbf{X}_{\varphi\varphi} \tag{2.25}$$
$$M = \mathbf{n} \cdot \mathbf{X}_{\varphi\lambda} \tag{2.26}$$
$$N = \mathbf{n} \cdot \mathbf{X}_{\lambda\lambda} \tag{2.27}$$

The principal directions $\mathbf{t}_{k1}$ and $\mathbf{t}_{k2}$ in $\mathbf{T}_p$ are then the corresponding eigenvectors of $\mathbf{S}_p$ computed by

$$\mathbf{t}_{ki} = \begin{cases} S_{1,2} \cdot \mathbf{e}_1 + (\kappa_i - S_{1,1}) \cdot \mathbf{e}_2 & , S_{2,1} = 0 \\ \mathbf{e}_i & , S_{2,1} = S_{1,2} = 0 \\ (\kappa_i - S_{2,2}) \cdot \mathbf{e}_1 + S_{2,1} \cdot \mathbf{e}_2 & , \text{otherwise} \end{cases} \tag{2.28}$$

where $\mathbf{e}_1 = (1,0)^T$, $\mathbf{e}_2 = (0,1)^T$ and $i \in [1,2]$.

With this information, it is possible to describe the earth surface locally by another regular surface with the same tangential plane and the same principal curvatures and directions. In this study, a torus is chosen. A position vector $\mathbf{Y}$ in torus coordinates (h, p, q) is defined by

$$Y_1 = (R_t + (r_t + h)\cos p)\cos q \tag{2.29}$$
$$Y_2 = (R_t + (r_t + h)\cos p)\sin q \tag{2.30}$$
$$Y_3 = (r_t + h)\sin p \tag{2.31}$$

For the sake of simplification, all points on the surface around a point p and the coordinates of the satellite are transformed to fulfil the following conditions:

1. $\mathbf{X}(\mathbf{p}) \mapsto \mathbf{Y}(\mathbf{0}) = (R_t + r_t) \cdot \mathbf{i} = \dfrac{\mathbf{i}}{\kappa_2}$, with $\mathbf{i} = (1,0,0)^T$.
2. $\mathbf{n} \mapsto \mathbf{e}_h$
3. $\dfrac{(\mathbf{X}_\varphi, \mathbf{X}_\lambda) \cdot \mathbf{t}_{k1}}{\|(\mathbf{X}_\varphi, \mathbf{X}_\lambda) \cdot \mathbf{t}_{k1}\|_2} \mapsto \mathbf{e}_p$

The second principal direction is not considered as it forms - per definition - an orthogonal basis together with the first principal direction and the normal vector. Condition 3 is chosen to match $\mathbf{e}_p = \mathbf{e}_\varphi$ if the earth surface is represented by a reference ellipsoid.

In the following, $\mathbf{p}$ is chosen as the orthogonal projection of the satellite position on the reference ellipsoid. This has the benefit that in further calculations at $\mathbf{Y}(\mathbf{0})$ the antenna gain has its maximum when no mispointing would occur.

Conditions 1 to 3 are fulfilled after the following transformation steps:

1. Translation with respect to torus centre $\mathbf{M}$:
   $\mathbf{X} \mapsto \mathbf{X} - \mathbf{M}$ with $\mathbf{M} = \mathbf{X}(\mathbf{p}) + \dfrac{\mathbf{n}}{\kappa_2}$

2. Rotation around z- and y-axis to fulfil condition 2:
   $\mathbf{X} \mapsto \mathbf{R}_z(\bar{\lambda}) \cdot \mathbf{R}_y(\bar{\varphi}) \cdot \mathbf{X}$
   $\mathbf{X}_\varphi \mapsto \mathbf{R}_z(\bar{\lambda}) \cdot \mathbf{R}_y(\bar{\varphi}) \cdot \mathbf{X}_\varphi$
   $\mathbf{X}_\lambda \mapsto \mathbf{R}_z(\bar{\lambda}) \cdot \mathbf{R}_y(\bar{\varphi}) \cdot \mathbf{X}_\lambda$
   with $\bar{\lambda} = -\arctan 2(-n_1/\kappa_2, -n_2/\kappa_2)$
   and $\bar{\varphi} = \arcsin(-n_3)$

3. Apply rotation around x-axis by $\bar{\alpha}$ to make e_p parallel to new z-axis
   with $\bar{\alpha} = \arctan 2(\sqrt{u_1^2 + u_2^2}, u_3)$
   and $\mathbf{u} = \dfrac{(\mathbf{X}_\varphi, \mathbf{X}_\lambda) \cdot \mathbf{t}_{k1}}{\|(\mathbf{X}_\varphi, \mathbf{X}_\lambda) \cdot \mathbf{t}_{k1}\|_2}$

These three steps are applied to the satellite state vector $\mathbf{P}$ and its velocity vector $\mathbf{V}$ given in earth-centred-earth-fixed Cartesian coordinates.

$$\mathbf{P} \mapsto \mathbf{R}_x(\bar{\alpha}) \cdot \mathbf{R}_z(\bar{\lambda}) \cdot \mathbf{R}_y(\bar{\varphi}) \cdot (\mathbf{P} - \mathbf{M}) \tag{2.32}$$

$$\mathbf{V} \mapsto \mathbf{R}_x(\bar{\alpha}) \cdot \mathbf{R}_z(\bar{\lambda}) \cdot \mathbf{R}_y(\bar{\varphi}) \cdot \mathbf{V} \tag{2.33}$$

The transformation from Cartesian to torus coordinates of the satellite position (h_2, p_2, q_2) is computed with

$$h_2 = \sqrt{\left(\sqrt{P_1^2 + P_2^2} - R_t\right)^2 + P_3^2} - r_t \tag{2.34}$$

$$p_2 = \arcsin\left(\frac{P_3}{h_2 + r_t}\right) \tag{2.35}$$

$$q_2 = \arctan 2(P_2, P_1) \tag{2.36}$$

where the index 2 is used here for the satellite position. The velocity vector is transformed using Eq. 2.37 to 2.39:

$$v_h = \frac{1}{h_2 + r_t}\left[\left(1 - \frac{R_t}{\sqrt{P_1^2 + P_2^2}}\right)(P_1 V_1 + P_2 V_2) + P_3 V_3\right] \tag{2.37}$$

$$v_p = \frac{1}{\sqrt{(h_2 + r_t)^2 - P_3^2}}\left[V_3 - \frac{P_3 v_h}{h_2 + r_t}\right] \tag{2.38}$$

$$v_q = \frac{P_1 V_2 - P_2 V_1}{P_1^2 + P_2^2} \tag{2.39}$$

For the velocity vector, no point identification indexes are necessary as the components of the surface velocity are not considered here. However, they will be discussed in section 2.3.

2.2.2 Choice of a Surface Representation

An open issue is the choice of a regular surface representation of the ocean. As this study is pioneer work, it makes sense to start with a simplified case using a static ocean representation. This means that dynamic effects such as tides, storms or atmospheric circulations are not considered, although naturally it is possible to include them if their representation are steadily differentiable up to order two. Following these considerations, possible representations are:

- The Mean Sea Surface (MSS), which includes the geoid undulations and the mean dynamic topography
- The geoid undulations, given as the height difference between the reference equipotential surface and the reference ellipsoid

Although the MSS is the better surface representation as it includes mean dynamics such as currents, the geoid is used in the further study. The reason behind this is that the MSS such as DTU18 (see Anderson et al. [2018]) is distributed as one arc-minute grids, which means that the derivatives need to be calculated numerically in a way that they are steady up to order two.

For the geoid - which can be calculated fully analytically with spherical harmonics - this restriction does not apply. As a good approximation over open ocean, the geoid N undulation can be calculated as follows (see Losch and Seufer [2003]):

$$N = \frac{V - V_0}{\gamma_0} \tag{2.40}$$

with γ_0 the normal gravity being a latitude-dependent quantity, V the total gravity potential and V_0 the potential of the reference ellipsoid.

V is calculated with spherical harmonics as

$$V = \frac{GM}{r} \sum_{m=0}^{\infty} \sum_{n=0}^{\infty} \left(\frac{a_e}{r}\right)^n \left[\bar{C}_{mn} \cos(m\lambda) + \bar{S}_{mn} \sin(m\lambda)\right] \bar{P}_{mn}(\cos\bar{\varphi}) \tag{2.41}$$

with GM the earth gravity mass constant, r, $\bar{\varphi}$, λ spherical coordinates, a_e the equatorial radius, $\bar{C}_{mn}$, $\bar{S}_{mn}$ fully-normalized spherical harmonics coefficients and $\bar{P}_{nm}$ fully-normalized associated Legendre polynomials.

GM, a_e and $\bar{C}_{mn}$, $\bar{S}_{mn}$ can be extracted from gfc files distributed by the International Centre for Global Earth Models (ICGEM). A detailed step-by-step instruction about evaluating Eq. 2.41 in a numerical stable manner is given in Kuga and Carrara [2013], whereas in Losch and Seufer [2003] the calculation of geoid undulations for radar altimetry applications is discussed.

With this, it is possible to define for each surface location a best-fitting torus coordinate system by inserting Eq. 2.40 into Eq. 2.15-2.17. In this study, the spherical harmonics coefficients of the EIGEN-6C4 model are used. This model contains coefficients up to degree and order 2190, giving a spatial resolution of about ten kilometres. A detailed discussion of EIGEN-6C4 is given in Förste et al. [2014].

As the spherical harmonics computation is computationally costly, the undulation and the derivatives up to order two of Eq. 2.15 to 2.17 are precomputed and stored in a one arc-minute spatial resolution grid file. The calculation of the torus coordinate systems for each surface location are then performed during the processing of the L1A data on the fly from the gridded values.

Figure 2.5 shows the the global geoid undulations for open ocean using EIGEN-6C4 spherical harmonics coefficients in a relief structure, which means that the colour bar is not perfectly correct as it does not account for the shadow effects. However, this presentation makes it easier to see trenches and sea mountains such as the Marianna trench which is discussed in chapter 6.

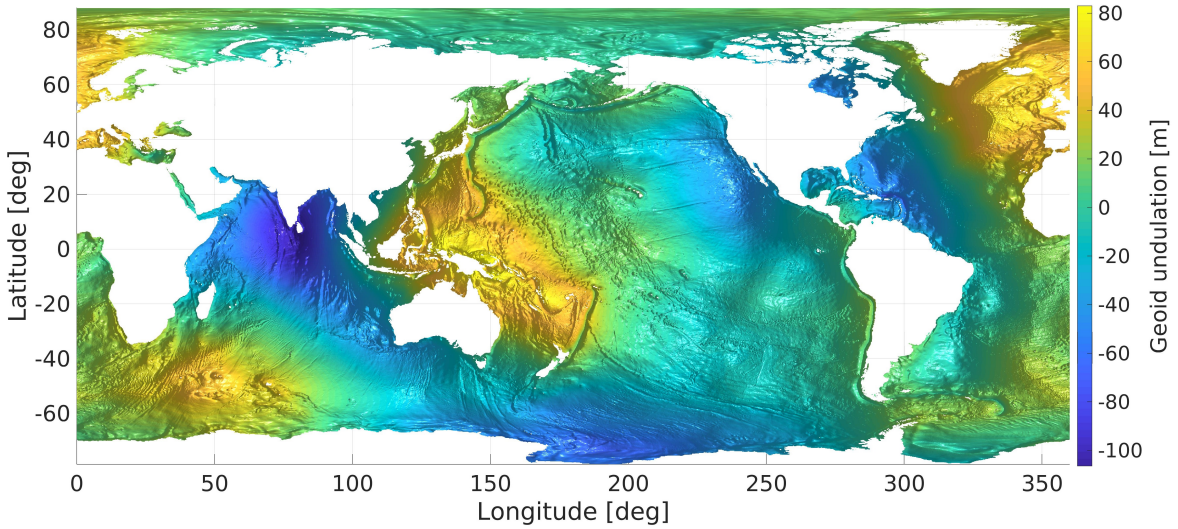

Figure 2.5: Global geoid undulations over ocean calculated with EIGEN-6C4 spherical harmonics coefficients

As mentioned in Sandwell and Smith [2014], the slopes of the surface affect estimated sea level heights. Figure 2.6 shows the absolute angle between the normal vector of the reference ellipsoid $\mathbf{n}_{ell}$ and the geoid $\mathbf{n}_{geoid}$ shown in Figure 2.5 given as:

$$\measuredangle(\mathbf{n}_{ell}, \mathbf{n}_{geoid}) = \arccos(\mathbf{n}_{ell} \cdot \mathbf{n}_{geoid}) \tag{2.42}$$

Of course, the slopes will be introduced as direction dependent quantities. Figure 2.6 only shows the magnitude of these measures being approximately the absolute deflection from vertical over the ocean. The angles vary between zero and seventy-five arc seconds which - according to Eq. 2.14 - would lead to a height error of up to 4.8 cm for CryoSat-2.

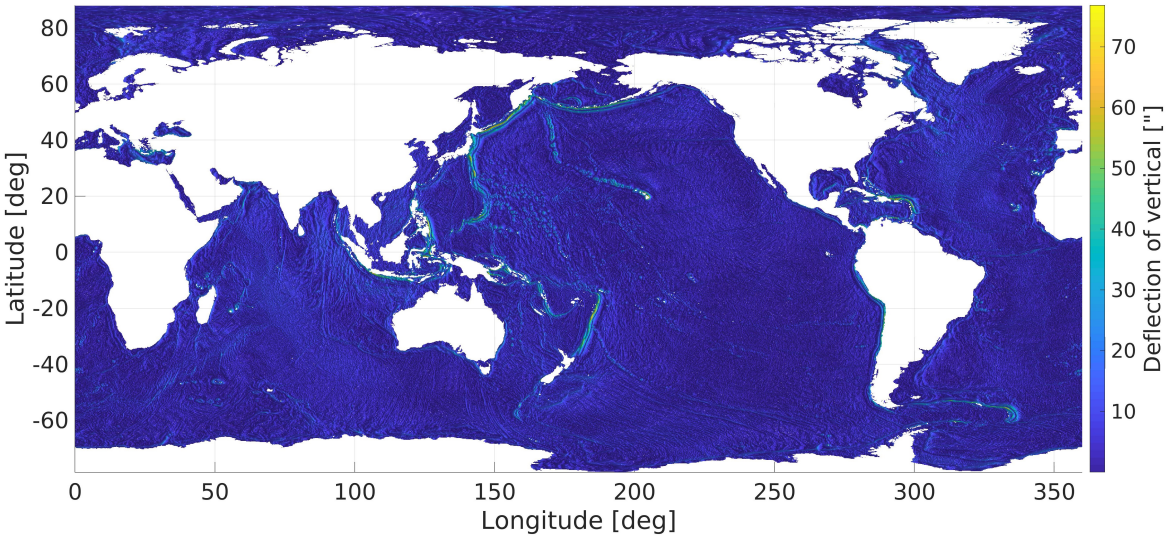

Figure 2.6: Global absolute deflection of the vertical over ocean calculated with EIGEN-6C4 spherical harmonics coefficients

An open question that has not been studied concerns the variation of curvatures on the geoid and how it affects radar altimetry signals. Figure 2.7 shows the difference between the two principal curvatures with respect to the Gaussian curvature of the reference ellipsoid K, given as

$$K = \frac{{a_e}^2 \cos^2 \varphi + {b_e}^2 \sin^2 \varphi}{{a_e}^2 b_e} \tag{2.43}$$

with b_e the semi-minor axis of the reference ellipsoid.

The relative differences shown in Fig. 2.7 vary between zero and eighteen percent, which is significant. It is important to note that the relative differences are often maximal when the slope in Fig. 2.6 gets close to zero and contrary. This means that curvatures and slopes need to be considered together to describe the sea surface correctly.

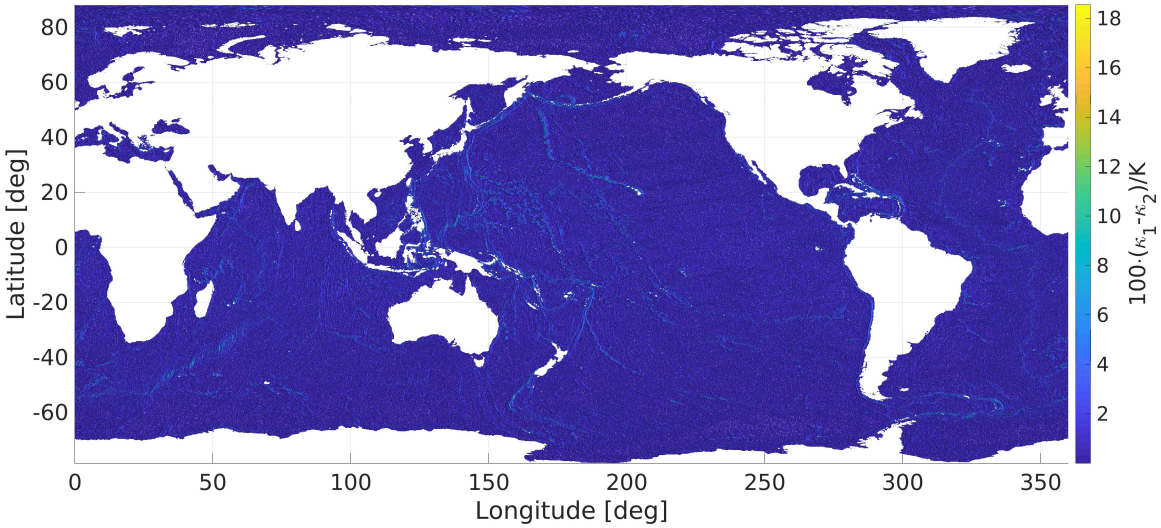

Figure 2.7: Global principal curvature differences over ocean calculated with EIGEN-6C4 spherical harmonics coefficients relative to the Gaussian curvature of the reference ellipsoid

2.3 Stochastic Description of the Sea State

The retrieval of geophysical parameters by radar altimetry is based on fitting a waveform or a stack with a modelled functional representation of it. To achieve this, two pieces of information are needed for each scattering area element.

1. Its location within the processed stack, which depends on its distance and relative velocity to the platform.
2. The power backscattered to the antenna.

Whereas the relative distance and velocity defining the position of a scattering area element in the stack can be described by the sea surface elevation η and its temporal derivatives, according to Barrick [1968] the backscattered power is related to the spatial derivatives. To quantify these, it is necessary to understand how a surface area element behaves in space and time. According to chapter 8 of Trujillo and Thurman [2010] water waves are energy in motion, whereas the water does not travel at all; instead water particles oscillates in so-called orbits. This movement is described in Figure 2.8 for a wave approaching the beach. The shape of an orbit mainly depend on the wavelength, the depth of a water particle and the water depth. For deep water, the orbits are circular shaped whereby their radius decreases with an increasing water depth. The water particle motion below a depth of half the wavelength is sufficiently small to be ignored, which means that then no wave surface interaction exists. If the water depth decreases the orbits interact with the sea floor leading them to gain an elliptical shape. This leads to a reduction of the wavelength and an increasing wave height. The waves

become more steep until they eventually break close to the beach. This study assumes that all waves are located in the deep water, as otherwise non-linear effects need to be considered.

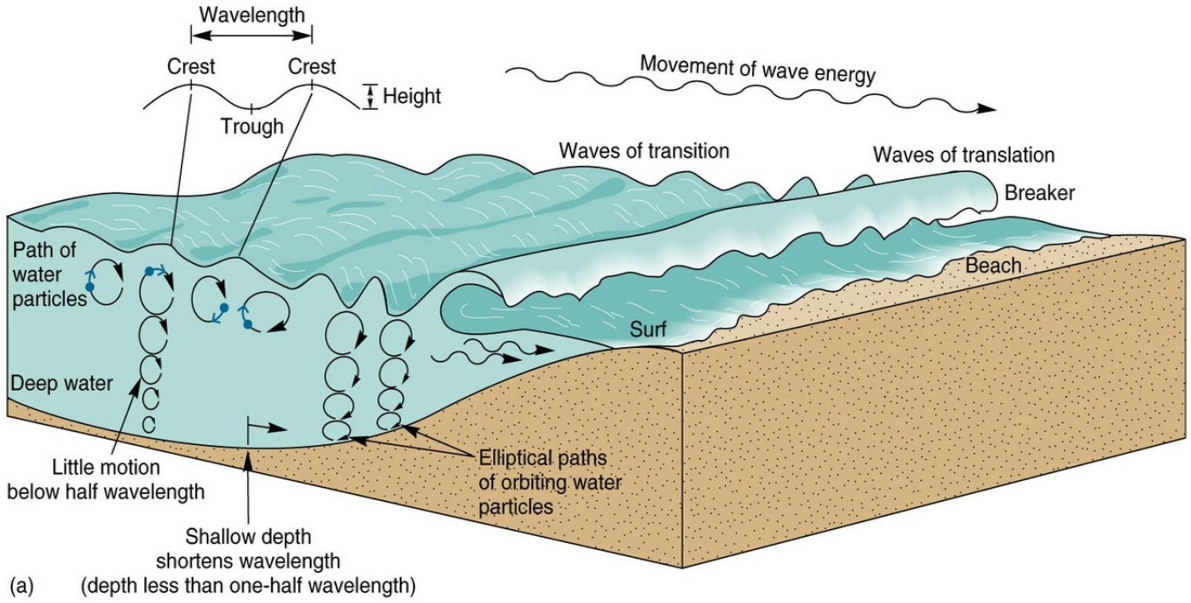

Figure 2.8: Wave particle motion of ocean waves in deep water and during approaching the coast. Source of the graphic: WAVES (https://www.thegeographeronline.net/uploads/2/6/6/2/26629356/1398548_orig.jpg) by Steven Heath, licenced under CC BY-NC-SA 4.0 (https://creativecommons.org/licenses/by-nc-sa/4.0/), both links were accessed on 10th of June 2019.

As the elevation and motion of each scattering water particle on the wave is not known, the surface of the wave field is described by a stochastic process, which needs to be defined first. According to Banner [1990], the sea surface elevation η is representable by a homogenous stationary random process with PDF $p_\eta(z)$ and autocorrelation function $\varrho(\tau, \mathbf{r})$, where τ is the time delay of two epochs and $\mathbf{r}$ the spatial separation vector.

Another useful function to describe the sea surface is its power density spectra, also called the wavenumber-frequency-spectrum $S_{\eta\eta}$. This is widely used in oceanography as it describes the mean distribution of wave energy in spatial and temporal domain [Banner, 1990]. $S_{\eta\eta}$ is defined as

$$S_{\eta\eta}(\omega, \mathbf{k}) = \sigma_z^2 \iiint_{\mathbb{R}^3} \varrho(\tau, \mathbf{r}) e^{i\omega\tau - i\mathbf{k}\mathbf{r}} d\mathbf{r} d\tau = \| \hat{\eta}(\omega, \mathbf{k}) \|_2^2 \tag{2.44}$$

with $\mathbf{k}$ the wavenumber vector, ω the angular frequency and σ_z^2 the variance of the surface elevation. $\hat{\eta}(\omega, \mathbf{k})$ denotes the Fourier transform of $\eta(t, \mathbf{x})$. $S_{\eta\eta}$ is per definition a real and even function. For convenience, often the one sided spectrum $G_{\eta\eta}$ is used which is defined for positive arguments only.

The autocorrelation function ϱ is defined as the normalized covariance of two neighboured points

$$\varrho(\tau, \mathbf{r}) = \frac{Cov\left[\eta(t_0, \mathbf{x}), \eta(t_0 + \tau, \mathbf{x} + \mathbf{r})\right]}{\sigma_z^2} = \frac{E\eta(t_0, \mathbf{x})\eta(t_0 + \tau, \mathbf{x} + \mathbf{r})}{\sigma_z^2} \tag{2.45}$$

with t_0 an arbitrary epoch and $\mathbf{x}$ a position vector. Due to η being a stationary random process, t_0 and $\mathbf{x}$ are arbitrary. $\varrho(\tau, \mathbf{r})$ is by definition one at its origin.

In oceanography many sea state-related parameter are expressed as a function of absolute spectral moments, defined as

$$M_k^{(\Omega)} = \int_{-\infty}^{\infty}\int_{-\infty}^{\infty} |\omega^k| S_{\eta\eta}(\omega, \mathbf{k}) d\omega d\mathbf{k} = \int_0^{\infty}\int_0^{\infty} \omega^k G_{\eta\eta}(\omega, \mathbf{k}) d\omega d\mathbf{k} \tag{2.46}$$

With $M_k^{(\Omega)}$ the absolute moment of the one-sided frequency spectrum. For the spatial case the absolute moments $M_k^{(K)}$ are defined as

$$M_k^{(K)} = \int_{-\infty}^{\infty}\int_{-\infty}^{\infty} |\mathbf{k}^k| S_{\eta\eta}(\omega, \mathbf{k}) d\omega d\mathbf{k} = \int_0^{\infty}\int_0^{\infty} \mathbf{k}^k G_{\eta\eta}(\omega, \mathbf{k}) d\omega d\mathbf{k} \tag{2.47}$$

In table 2.2, the relations between some ocean parameters and spectral moments are shown, extracted from Kitano et al. [2002], Jean-Raymond [2016] and Myrhaug [2018].

Symbol	Description	Formula
H_s	Mean of the highest third of wave heights	$H_s = 4\sqrt{M_0^{(\Omega)}} = 4\sigma_z$
s_o^2	Mean square sea surface slope	$s_o^2 = {\sigma_x}^2 = {\sigma_y}^2 = M_2^{(K)}$
T_{01}	Reciprocal of the mean frequency of the wave spectra	$T_{01} = 2\pi \frac{M_0^{(\Omega)}}{M_1^{(\Omega)}}$
T_{02}	Mean time interval between zero up-crossings	$T_{02} = 2\pi \sqrt{\frac{M_0^{(\Omega)}}{M_2^{(\Omega)}}}$
T_{24}	Mean time interval between two local maxima	$T_{24} = 2\pi \sqrt{\frac{M_2^{(\Omega)}}{M_4^{(\Omega)}}}$
μ_m	Spectral wave steepness	$\mu_m = \frac{2\pi H_s}{g {T_{02}}^2}$
μ	Expected value of wave steepness within a wave field	$\mu \approx 0.611 \mu_m$

Table 2.2: Summary of statistical wave parameters.

The symbols in table 2.2 are σ_z as the standard deviation of the wave particle elevations, σ_x the standard deviation of surface slopes in upwind direction, σ_y the standard deviation of surface slopes in crosswind direction and g describing the norm of the gravitational acceleration vector. The up-crossing period is defined as the time span that a wave particle needs to cross the mean sea level twice being up-crossing at both zero crossing epochs [Trujillo and Thurman, 2010]. A wave particle is up-crossing if its vertical velocity is positive. On the other hand, the wave steepness is defined as the wave height divided by the wavelength.

It is worth mentioning that the wave period parameters in table 2.2 are often referred to as the mean period for T_{01}, the mean zero up-crossing period for T_{02} and the mean peak-to-peak period for T_{24} [Kitano et al., 2002].

The derivatives of ϱ evaluated at zero relate to the spectral moments by [Papoulis, 1977, example 9-2]

$$\varrho_t^{(k)}(0) = \int_{-\infty}^{\infty}\int_{-\infty}^{\infty} (i\omega)^k S_{\eta\eta}(\omega, \mathbf{k}) d\omega d\mathbf{k} = i^k M_k^{(\Omega)} \tag{2.48}$$

whereat $\varrho_t^{(k)}$ is the k'th derivative of the autocorrelation function for the time domain. Whereas the absolute moments are always greater than zero, the moments of odd order are zero due to $S_{\eta\eta}$ being an even function.

The next sections deal with the derivation of temporal and spatial joint PDF in the case of weekly non-linear Gaussian waves. For the sake of convenience η is assumed to be isotropic, which means that no direction dependencies exist. Of course, the following probability density functions may be extended to allow direction dependencies.

2.3.1 Sea Surface Elevation PDF

Before dealing with the PDF of temporal and spatial derivatives, it is necessary to examine the elevation η first. In Socquet-Juglard et al. [2005], η is described with an infinite series as

$$\eta = \bar{\eta} + \frac{1}{2}\left(Be^{i\theta} + B_2 e^{2i\Theta} + B_3 e^{3i\theta} + ...c.c.\right) \tag{2.49}$$

with $\bar{\eta}$ the mean sea surface elevation, which is a function of higher order than two with mean wave steepness μ and B, B_1 and B_2 are functions of space and time. $\theta = \mathbf{k}_p\mathbf{x} - \omega_p t$ with $\mathbf{k}_p$ the peak wave number vector, $\mathbf{x}$ the position vector, ω_p the peak angular frequency and t the time.

Truncating Eq. 2.49 after the linear steepness terms and setting $B_2 = \frac{\mu}{2}B^2$ (see Socquet-Juglard et al. [2005]) yields

$$\begin{aligned} \eta &= \frac{1}{2}\left(Be^{i\theta} + \frac{\mu}{2}B^2 e^{2i\theta}\right) + \mathcal{O}(\mu^2) \\ &\approx a\cos(\theta+\psi) + \frac{\mu}{2}a^2\cos(2\theta+2\psi) \\ &= a\cos(\theta+\psi) + \frac{\mu}{2}a^2\cos^2(\theta+\psi) - \frac{\mu}{2}a^2\sin^2(\theta+\psi) \end{aligned} \tag{2.50}$$

whereat in the second part $B = ae^{i\psi}$ was set with ψ being a random phase following a uniform distribution over an interval of 2π. Setting $\eta_1 = a\cos(\theta+\psi)$, $\eta_2 = a\sin(\theta+\psi)$ and scaling η by the standard deviation of the surface elevation σ_z leads to

$$\eta = \sigma_z\eta_1 + \frac{\sigma_z\mu}{2}\eta_1^2 - \frac{\sigma_z\mu}{2}\eta_2^2 = \frac{\sigma_z\mu}{2}\left[\left(\eta_1 + \frac{1}{\mu}\right)^2 - \eta_2^2 - \frac{1}{\mu^2}\right] \tag{2.51}$$

$\eta_1 \sim N(0,1)$ and $\eta_2 \sim N(0,1)$ are independent random variables.

It is often more convenient to perform calculations using the Characteristic Functions (CFs) φ [Papoulis and Pillai, 2002, Chapter 5-5], which are defined as

$$\varphi_X(u) = E\left[e^{iX}\right] = \int_{-\infty}^{\infty} p_X(x)e^{iux}dx \tag{2.52}$$

with $p_X(x)$ a probability density function of a random variable X. One property is that the summation of independent random variable leads to a multiplication of the CFs instead of a convolution of the PDFs

$$p_{X+Y}(x) = p_X(x) * p_Y(x) \tag{2.53}$$

$$\varphi_{X+Y}(u) = \varphi_X(u)\cdot\varphi_Y(u) \tag{2.54}$$

This can be used to calculate the CF of η, whereas its PDF does not have an elementary solution. The CF of η φ_η is given by

$$\varphi_\eta(u) = \frac{1}{\sqrt{1+\sigma_z^2\mu^2u^2}}\exp\left\{-\frac{\sigma_z^2u^2}{2(1-i\mu\sigma_z u)}\right\} \tag{2.55}$$

where for zero steepness $\varphi_\eta(u)$ becomes a normal distribution.

The central and standardized moments of interest can now be computed using cumulants κ_n, which are defined as

$$\kappa_n = \frac{1}{i^n} \frac{\partial^n \ln(\varphi(u))}{\partial u^n}\bigg|_{u=0} \tag{2.56}$$

leading to an expected value of $E[\eta] = 0$, a variance of $Var[\eta] = {\sigma_z}^2(1+\mu^2)$ a skewness of $Skew[\eta] = \frac{\kappa_3}{\sqrt{\kappa_2^3}} \approx 3\mu$ and an excess kurtosis being $Excess[\eta] = \frac{\kappa_4}{\kappa_2^2} \approx 12\mu^2$. Following Socquet-Juglard et al. [2005], it is safe to assume $\mu < 0.1$ leading to an excess of η smaller than 0.12 when the skewness is lower than 0.3.

2.3.2 Velocities and Accelerations

As shown in subsection 2.1.2, the position of the backscattered power coming from a surface area within a SAR stack depends on the distance and the relative velocity between the platform and the scattering area. The relative velocity can be separated in two parts:

1. The velocity of the platform.

2. The velocity of the scattering surface area.

The platform velocity is well known due to precise orbit determination techniques and is extracted from the L1A data. By contrast, the vertical wave particle velocities are unknown. Just like the surface elevation, this quantity is introduced as a random variable for each scattering surface element and as a stationary process for the whole illuminated sea surface. Additionally, the acceleration is considered in this subsection.

By definition the vertical wave particle velocity is defined as the derivative of the elevation with respect to the time delay τ, which can be written as a differential quotient (see Barrick [1968]):

$$\eta_t = \lim_{\tau \to 0} \frac{\eta(\tau, \mathbf{0}) - \eta(0, \mathbf{0})}{\tau} \tag{2.57}$$

The same approach can be used for the vertical wave acceleration η_{tt}:

$$\eta_{tt} = \lim_{\tau \to 0} \frac{\eta(\tau, \mathbf{0}) - 2\eta(0, \mathbf{0}) + \eta(-\tau, \mathbf{0})}{\tau^2} \tag{2.58}$$

The variances and covariances can then be calculated by using several properties of expected values and variances. $Var[\eta_t]$ is computed by using

$$Var[X - Y] = Var[X] + Var[Y] - 2Cov[X, Y] \tag{2.59}$$

$$Cov[X, Y] = E[XY] - E[X]E[Y] \tag{2.60}$$

with X and Y being arbitrary dependent random variables. For sea surface elevations and their derivatives, the expected values are per definition zero.

$$Var[\eta_t] = \lim_{\tau \to 0} Var\left[\frac{\eta(\tau, \mathbf{0}) - \eta(0, \mathbf{0})}{\tau}\right] = -\sigma_z^2 \lim_{\tau \to 0} \frac{\varrho_t(\tau) - 2\varrho_t(0) + \varrho_t(-\tau)}{\tau^2} = -\sigma_z^2 \varrho_t^{(2)}(0) = M_2^{(\Omega)} = {\sigma_v}^2 \tag{2.61}$$

This gives the variance of the vertical wave particle velocity to be the second-order spectral moment. Using the same approach for the acceleration yields:

$$Var[\eta_{tt}] = \sigma_z^2 \lim_{\tau \to 0} \frac{\varrho_t(-2\tau) - 4\varrho_t(-\tau) + 6\varrho_t(0) - 4\varrho_t(\tau) + \varrho_t(2\tau)}{\tau^4} = \sigma_z^2 \varrho_t^{(4)}(0) = M_4^{(\Omega)} = {\sigma_a}^2 \tag{2.62}$$

The final non-zero stochastic measure of order two is the covariance between the surface elevation and the acceleration given by:

$$Cov[\eta, \eta_{tt}] = \sigma_z^2 \lim_{\tau \to 0} \frac{\varrho_t(\tau) - 2\varrho_t(0) + \varrho_t(-\tau)}{\tau^2} = \sigma_z^2 \varrho_t^{(2)}(0) = -M_2^{(\Omega)} = -{\sigma_v}^2 \tag{2.63}$$

In summary, the vertical wave particle velocities and accelerations can be described by the second- and fourth-order moment of the wave spectra. A negative covariance between the elevation and the accelerations exists, which leads to positive accelerations at negative elevations. An interesting result is that $Cov(\eta, \eta_{tt}) = -Var(\eta_t)$ which allows estimating these quantities together as one variable during retracking.

As this study considers fast convolution-based retrackers, it is crucial to know the joint characteristic function for all three random variables. This is achieved by starting with the difference quotients shown earlier and insert them in Eq. 2.52. For the sake of completeness, in the following the joint PDF of the standard normal distributed elevations are shown.

First a vector is defined containing the arguments of the PDF

$$\mathbf{z}^T = [z_m, z_0, z_p] \tag{2.64}$$

with z_m the elevation at epoch $t_0 - \tau$, z_0 the elevation at epoch t_0 and z_p at the at epoch $t_0 + \tau$. The covariance matrix of $\mathbf{z}$ and its inverse are then

$$\Sigma = \begin{bmatrix} 1 & \rho & \omega \\ \rho & 1 & \rho \\ \omega & \rho & 1 \end{bmatrix} \Rightarrow \Sigma^{-1} = \frac{1}{\det \Sigma} \begin{bmatrix} 1-\rho^2 & \rho(\omega-1) & \rho^2-\omega \\ \rho(\omega-1) & 1-\omega^2 & \rho(\omega-1) \\ \rho^2-\omega & \rho(\omega-1) & 1-\rho^2 \end{bmatrix} \tag{2.65}$$

with $\rho = \varrho_t(\tau)$ and $\omega = \varrho_t(2\tau)$ being auxiliary variables and the determinant $\det \Sigma = 1 + 2\rho^2(\omega - 1) - \omega^2$.

The PDF of $\mathbf{z}$ is defined as a standard normal distribution by

$$p_{\eta_i}(\mathbf{z}) = \frac{1}{\sqrt{(2\pi)^3 \det \Sigma}} \exp\left\{ -\frac{\mathbf{z}^T \Sigma^{-1} \mathbf{z}}{2} \right\} \tag{2.66}$$

Inserting the difference quotients in Eq. 2.52 together with the PDF of $\mathbf{z}$ yields

$$\begin{aligned} \varphi_{\eta,\eta_t,\eta_{tt}}(u,v,w) &= \lim_{\tau \to 0} \iiint_{\mathbb{R}^3} \exp\left\{ \frac{i\mu}{2} \frac{\lambda z_m + z_m^2 - 2\lambda z_0 - 2z_0^2 + \frac{2}{\mu} z_p + z_p}{\tau^2} w + \frac{i\mu}{2} \frac{\lambda z_p + z_p^2 - \lambda z_0 - z_0^2}{\tau} v + \frac{i\mu}{2} \left(\lambda z_0 + z_0^2\right) u \right\} p_{\eta_i}(\mathbf{z}) d\mathbf{z} \\ &\times \lim_{\tau \to 0} \iiint_{\mathbb{R}^3} \exp\left\{ -\frac{i\mu}{2} \frac{z_m^2 - 2z_0^2 + z_p}{\tau^2} w - \frac{i\mu}{2} \frac{z_p^2 - z_0^2}{\tau} v - \frac{i\mu}{2} z_0^2 u \right\} p_{\eta_i}(\mathbf{z}) d\mathbf{z} \end{aligned} \tag{2.67}$$

with $\lambda = \frac{2}{\mu}$. The partition in two integrals is possible as the two normally-distributed variables in Eq. 2.51 used to derive η are independent.

The integrals can be solved using Gradshteyn and Ryzhik [2007, Eq. 3.323 2.10]. An approximate solution for $\mu \leq 0.2$ is given as:

$$\begin{aligned} \varphi_{\eta,\eta_t,\eta_{tt}}(u,v,w) &\approx \frac{1}{1+\mu^2\sigma_a^2w^2}\frac{1}{\sqrt{(1+\mu^2\sigma_v^2v^2)^2+\mu^2\sigma_a^2w^2+\mu^2\sigma_z^2u^2}} \\ &\times \exp\left\{-\frac{\sigma_z^2u^2+\sigma_v^2v^2-2\sigma_v^2uw+\sigma_a^2w^2}{2(1+i\mu\sigma_aw-i\mu\sigma_zu+\mu^2\sigma_v^2v^2+\mu^2\sigma_a^2w^2)}\right\} \end{aligned} \tag{2.68}$$

As for the elevation, Eq. 2.68 becomes a normal distribution for $\mu = 0$. In table 2.3, an overview is provided of all central moments up to order four. Contrary, the skewness and kurtosis are by definition normalized by the standard deviations.

	η	η_t	η_{tt}
E	0	0	0
Var	$\sigma_z^2(1+\mu^2)$	$\sigma_v^2(1+\mu^2)$	$\sigma_a^2(1+3\mu^2)$
Skew	3μ	0	-3μ
Kurt-3	$12\mu^2$	$12\mu^2$	$12\mu^2$

Table 2.3: Central moments for η, η_t and η_{tt}

With exception of the skewness, all moments are very similar. Whereas for η it is positive, for η_t it is zero meaning that this variable is symmetric. For η_{tt} the skewness becomes negative, which is logical as for positive elevations negative accelerations are expected and in contrary.

To give a first impression on how wave steepness affects the joint PDFs, these are shown in Figure 2.9 and 2.10 for two different cases, whereas Figure 2.9 gives the case for zero steepness Figure 2.10 shows the PDF for a very high value of 0.2 which should not occur for wind waves in the open ocean.

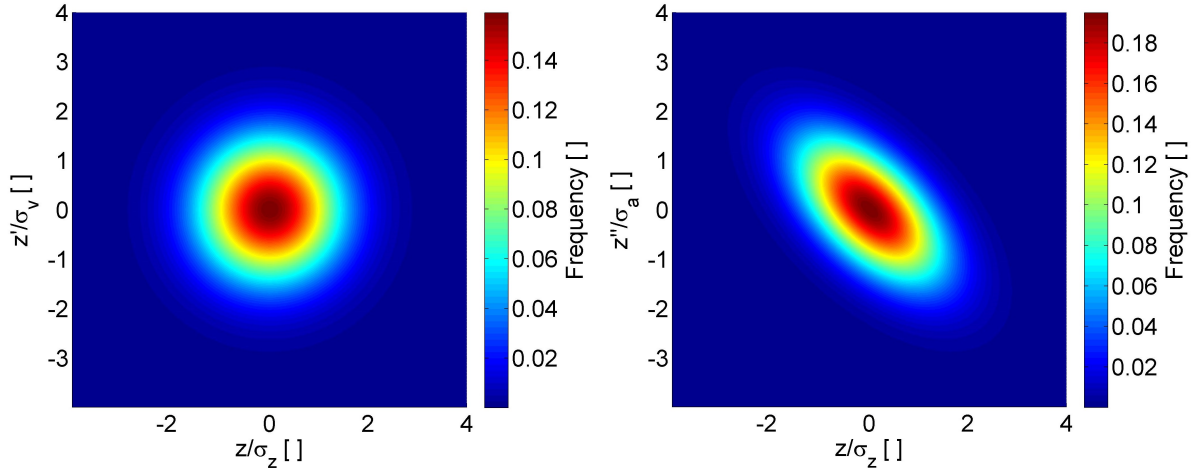

Figure 2.9: Joint PDF for $\mu = 0.0$. On the left for the normalized elevation and the normalized vertical wave particle velocity and on the right for the normalized elevation and the normalized vertical wave particle acceleration.

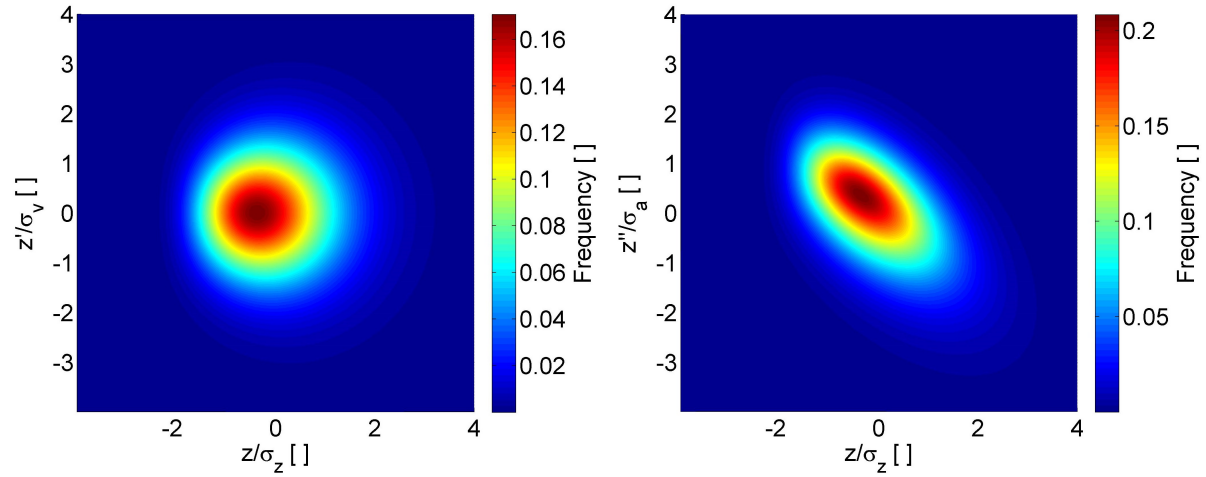

Figure 2.10: Joint PDF for $\mu = 0.2$. On the left for the normalized elevation and the normalized vertical wave particle velocity and on the right for the normalized elevation and the normalized vertical wave particle acceleration.

An interesting aspect of the vertical wave particle velocity - shown on the left side of Figure 2.9 and 2.10 - is that even if it is uncorrelated to the elevation, the variance decreases for negative elevations and contrary. This is caused by the waves being smoother at the troughs, leading to a lower variety of velocities compared to the crest. For waves with zero steepness, this effect is not observed.

For the vertical wave particle accelerations due to its correlation with the elevation, the expected value increases for both cases with negative elevations and contrary. The main difference between both cases besides the skewness is the conditional variance. Where for Figure 2.9 it is constant for the case with high steepness, it is proportional with the elevation as shown in Figure 2.9. This can be explained the same way as for the velocities, meaning smoother troughs lead to less varying vertical wave particle accelerations and the contrary for the crests.

2.3.3 Slopes and Curvatures

In contrast to the surface elevation and vertical wave motion, the slopes and curvatures do not affect the position of the backscattered power coming from a scattering element within the stack but rather its reflected intensity. Following Barrick [1968] and Kodis [1966], the average backscattered cross section - describing how much power is reflected from a finitely small surface area - can be described by

$$\sigma^0(\eta_{xsp}, \eta_{ysp}) = \pi |R(0)|^2 n_A E\left[\frac{1}{|K|}\right] \tag{2.69}$$

with $R(0)$ the Fresnel reflection coefficient for zero incidence, n_A the number of elemental scatterers in an unit area and K the mean Gaussian curvature.

As in Barrick [1968, Eq. 7], the number of scattering elements can be described as

$$n_A = p_{\eta_x,\eta_y|\eta}(z_x, z_y) \int_{-\infty}^{\infty}\int_{-\infty}^{\infty}\int_{-\infty}^{\infty} |z_{xx}z_{yy} - z_{xy}^2| p(z_{xx}, z_{xy}, z_{yy}|z, z_{tt}) dz_{xx} dz_{xy} dz_{yy} \tag{2.70}$$

with $p_{\eta_x,\eta_y|\eta}$ the probability density function of the spatial derivatives of η in the upwind direction η_x and crosswind direction η_y under the condition that the elevation is known. p describes the joint conditional probability density function of the second-order derivatives η_{xx}, η_{yy} and η_{xy}. As in the previous section, the subscripts of the η terms denote the variable after which the partial derivative was performed. For example $\eta_{xx} = \frac{\partial^2 \eta}{\partial x^2}$ gives the elevation twice differentiated

after the upwind coordinate x. Compared with Barrick [1968, Eq. 7], it is already considered that the second-order derivatives are uncorrelated with the slopes but correlated with the elevation and the vertical acceleration of scatterers.

Eq. 2.70 can be rewritten by using the definition of the expected value as:

$$n_A = p_{\eta_x,\eta_y|\eta}(z_x, z_y) E\left[|\eta_{xx}\eta_{yy} - \eta_{xy}^2| \,\middle|\, \eta = z, \eta_{tt} = z_{tt} \right] \tag{2.71}$$

The expected value of absolute curvature can be described in a similar manner following Barrick [1968], giving

$$E\left[\frac{1}{|K|}\right] = \sec^4(\theta_i) E\left[\frac{1}{|\eta_{xx}\eta_{yy} - \eta_{xy}^2|} \,\middle|\, \eta = z, \eta_{tt} = z_{tt} \right] \tag{2.72}$$

with θ_i being the incidence angle of the electromagnetic wave.

In Barrick [1968, Eq. 10], the product of the number of scattering elements and the curvature is simplified to

$$n_A E\left[\frac{1}{|K|}\right] = p_{\eta_x,\eta_y|\eta}(z_x, z_y) \sec^4(\theta_i) E\left[X\right] E\left[\frac{1}{X}\right] \approx p_{\eta_x,\eta_y|\eta}(z_x, z_y) \sec^4(\theta_i) \tag{2.73}$$

with $X = |\eta_{xx}\eta_{yy} - \eta_{xy}^2| \,\middle|\, \eta = z, \eta_{tt} = z_{tt}$ being an auxiliary variable to make the equation easier to read.

Eq. 2.73 gives that the terms including second-order derivatives are cancelling each other. However, by using Eq. 2.60 it can be shown that:

$$E[X]E\left[\frac{1}{X}\right] = E\left[\frac{X}{X}\right] - Cov\left[X, \frac{1}{X}\right] = 1 - Cov\left[X, \frac{1}{X}\right] \geq 1 \tag{2.74}$$

whereas the covariance term needs to be negative as the reciprocal term becomes smaller when the other terms increase, leading to a negative correlation, given that the products need to be greater than one. This means the quality of the approximation shown in Eq. 2.73 needs to be investigated as it is not known how much the product differs from one.

The product $E[X]E\left[\frac{1}{X}\right]$ is numerically evaluated in this work by using Monte-Carlo simulations. The idea is to generate dependent random values of elevations very close to a given location and epoch and use these as an input to the differential quotients. To receive sufficient second-order derivatives, it is necessary to choose small distances and time delays between each surface elevation as otherwise the numerical derivative is not accurate enough. On the other hand, a choice of very small distances would lead to erroneous results due to floating-point errors. In order to minimize this the following calculations were performed in quadruple precision by using the DoubleDouble Matlab library developed by Tom Holden, which is licenced under the GNU General Public License v3.0 and publicly available at https://github.com/tholden/DoubleDouble (accessed on 18/06/2019). As previously discussed all values shall have a dependency on η and η_{tt} which means that conditional random variables are simulated.

To perform the simulations, first a vector is defined containing the arguments of the PDFs, which depend on a upwind distance x, a crosswind distance y and a time delay τ, whereat the vertical acceleration of a wave particle z_{tt} will be represented by $z(0,0,-\tau)$ and $z(0,0,\tau)$.

$$\mathbf{z}^T = \begin{bmatrix} z(-x,0,0) & z(x,0,0) & z(0,-y,0) & z(0,y,0) & z(x,y,0) & z(0,0,-\tau) & z(0,0,\tau) & z(0,0,0) \end{bmatrix} \tag{2.75}$$

As the standard deviations σ_z of the elevations cancel each other out in $E[X]E\left[\frac{1}{X}\right]$, it is sufficient to consider the normalized covariance matrix, which is given by:

$$\Sigma = \begin{bmatrix} 1 & \varrho(2x,0,0) & \varrho(x,y,0) & \varrho(x,y,0) & \varrho(2x,y,0) & \varrho(x,0,\tau) & \varrho(x,0,\tau) & \varrho(x,0,0) \\ \varrho(2x,0,0) & 1 & \varrho(x,y,0) & \varrho(x,y,0) & \varrho(0,y,0) & \varrho(x,0,\tau) & \varrho(x,0,\tau) & \varrho(x,0,0) \\ \varrho(x,y,0) & \varrho(x,y,0) & 1 & \varrho(0,2y,0) & \varrho(x,2y,0) & \varrho(0,y,\tau) & \varrho(0,y,\tau) & \varrho(0,y,0) \\ \varrho(x,y,0) & \varrho(x,y,0) & \varrho(0,2y,0) & 1 & \varrho(x,0,0) & \varrho(0,y,\tau) & \varrho(0,y,\tau) & \varrho(0,y,0) \\ \varrho(2x,y,0) & \varrho(0,y,0) & \varrho(x,2y,0) & \varrho(x,0,0) & 1 & \varrho(x,y,\tau) & \varrho(x,y,\tau) & \varrho(x,y,0) \\ \varrho(x,0,\tau) & \varrho(x,0,\tau) & \varrho(0,y,\tau) & \varrho(0,y,\tau) & \varrho(x,y,\tau) & 1 & \varrho(0,0,2\tau) & \varrho(0,0,\tau) \\ \varrho(x,0,\tau) & \varrho(x,0,\tau) & \varrho(0,y,\tau) & \varrho(0,y,\tau) & \varrho(x,y,\tau) & \varrho(0,0,2\tau) & 1 & \varrho(0,0,\tau) \\ \varrho(x,0,0) & \varrho(x,0,0) & \varrho(0,y,0) & \varrho(0,y,0) & \varrho(x,y,0) & \varrho(0,0,\tau) & \varrho(0,0,\tau) & 1 \end{bmatrix} \tag{2.76}$$

To account for the conditions that the elevation and its vertical acceleration are known, the conditional expected value and the covariance matrix need to be calculated. This can be achieved by using the properties of conditional multivariate normal distributions

$$\boldsymbol{\mu}_{\mathbf{X_1}|\mathbf{X_2}} = \boldsymbol{\mu_1} + \Sigma_{12}\Sigma_{22}^{-1}(\mathbf{X_2} - \boldsymbol{\mu_1}) \tag{2.77}$$

$$\Sigma_{\mathbf{X_1}|\mathbf{X_2}} = \Sigma_{11} - \Sigma_{12}\Sigma_{22}^{-1}\Sigma_{21} \tag{2.78}$$

with $\boldsymbol{\mu}_1$ the vector containing the expected values of the unknown variables $\mathbf{X_1}$, $\mathbf{X}_2$ the values of the known variables and the Σ_{ij} terms the covariance matrix parts corresponding to the known and unknown parameters. For the sake of clearness, $\mathbf{X_1}$ and $\mathbf{X_2}$ are given here:

$$\mathbf{X_1}^T = \begin{bmatrix} z(-x,0,0) & z(x,0,0) & z(0,-y,0) & z(0,y,0) & z(x,y,0) \end{bmatrix} \tag{2.79}$$

$$\mathbf{X_2}^T = \begin{bmatrix} z(0,0,-\tau) & z(0,0,\tau) & z(0,0,0) \end{bmatrix} \tag{2.80}$$

The following equation gives the definition of the covariance matrix parts:

$$\Sigma = \begin{bmatrix} \Sigma_{11} & \Sigma_{12} \\ \Sigma_{21} & \Sigma_{22} \end{bmatrix} \tag{2.81}$$

As in this study $z(0,0,-\tau)$, $z(0,0,\tau)$ and $z(0,0,0)$ shall be the known variables e.g. Σ_{22} is given by:

$$\Sigma_{22} = \begin{bmatrix} 1 & \varrho(0,0,2\tau) & \varrho(0,0,\tau) \\ \varrho(0,0,2\tau) & 1 & \varrho(0,0,\tau) \\ \varrho(0,0,\tau) & \varrho(0,0,\tau) & 1 \end{bmatrix} \tag{2.82}$$

Accordingly, it is possible to calculate $E[X]E\left[\frac{1}{X}\right]$ for each wave steepness value, scatterer elevation and its vertical acceleration with Monte-Carlo simulations by applying the following steps. Whereat the correlation function ϱ is - according to Barrick [1968] - approximated by a Gaussian with

$$\varrho(x,y,\tau) \approx \exp\left\{-\frac{x^2+y^2+\tau^2}{2}\right\} \tag{2.83}$$

This approximation implies that the wave spectrum is also a Gaussian, which is not correct. However, as only values very close to the origin are needed, it should be sufficiently correct.

The calculation of $E[X]E\left[\frac{1}{X}\right]$ can then be performed by the following step:

1. Set small values for x, y and τ. In this study all three are set to 0.01.
2. Set the elevation value $z(0,0,0)$, a vertical wave particle acceleration z_{tt} and a wave steepness μ.
3. Calculate $z(0,0,-\tau) = z(0,0,\tau) = \frac{z_{tt}}{2}\tau^2 + z(0,0,0)$.
4. Calculate $\boldsymbol{\mu}_{\mathbf{X_1}|\mathbf{X_2}}$ and $\Sigma_{\mathbf{X_1}|\mathbf{X_2}}$.
5. Simulate a sufficiently large number of two independent, identically distributed random variable vectors $\bar{\mathbf{X}}_\mathbf{1}|\bar{\mathbf{X}}_\mathbf{2}$ and $\tilde{\mathbf{X}}_\mathbf{1}|\tilde{\mathbf{X}}_\mathbf{2}$ following a multivariate Normal distribution with expected values $\boldsymbol{\mu}_{\mathbf{X_1}|\mathbf{X_2}}$ and covariance matrix $\Sigma_{\mathbf{X_1}|\mathbf{X_2}}$. In this work 10000 values are simulated for each variable.
6. To receive a vector of elevations including wave steepness calculate $\mathbf{X_1}|\mathbf{X_2} = \bar{\mathbf{X}}_\mathbf{1}|\bar{\mathbf{X}}_\mathbf{2} + \frac{\mu}{2}\left(\bar{\mathbf{X}}_\mathbf{1}|\bar{\mathbf{X}}_\mathbf{2}^{②} - \tilde{\mathbf{X}}_\mathbf{1}|\tilde{\mathbf{X}}_\mathbf{2}^{②}\right)$. With ② denoting element-wise squaring
7. Use $\mathbf{X_1}|\mathbf{X_2}$ to compute the spatial derivatives of the elevation
   - $z_{xx} = \dfrac{z(-x,0,0) - 2z(0,0,0) + z(x,0,0)}{x^2}$
   - $z_{yy} = \dfrac{z(0,-y,0) - 2z(0,0,0) + z(0,y,0)}{y^2}$
   - $z_{xy} = \dfrac{z(x,y,0) - z(x,0,0) - z(0,y,0) + z(0,0,0)}{xy}$
8. Calculate $|z_{xx}z_{yy} - z_{xy}^2|$ and its reciprocal. For the sake of numerical precision only keep values if $\dfrac{1}{|z_{xx}z_{yy} - z_{xy}^2|}$ is smaller than one hundred times the upper quartile of the whole population.
9. Compute the mean of $|z_{xx}z_{yy} - z_{xy}^2|$ and its reciprocal separately.
10. Store the product of both expected values.

It can be observed in Figure 2.11 that $E[X]E\left[\frac{1}{X}\right]$ does not depend on vertical accelerations, which allows computing the average values in the z_{tt} direction, leading to Figure 2.12.

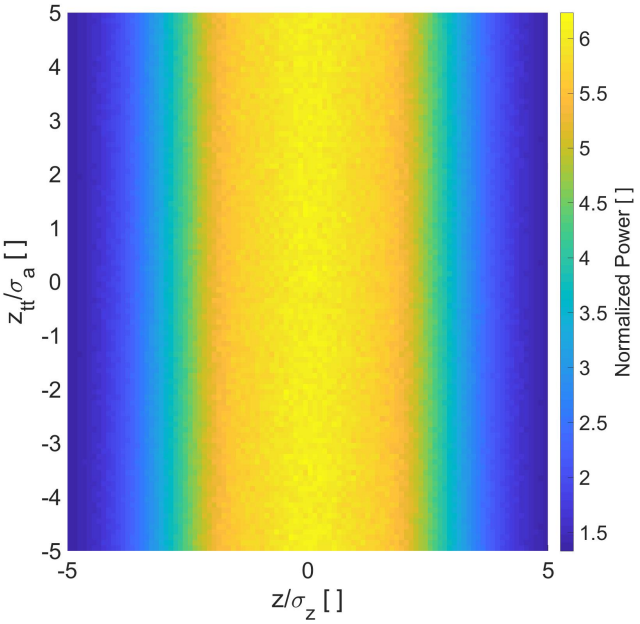

Figure 2.11: Product of E[|X|] and E[1/|X|] for different normalized elevations and vertical accelerations generated by Monte-Carlo simulations.

The curves in Figure 2.12 show the result of averaging Figure 2.11 in the z_{tt} direction resulting to a representation of the reflected power dependent on the elevation of a scattering surface element. In the case of zero steepness, the backscattering decreases slowly between minus two and plus two metre, whereas for absolutely higher elevations the backscattering reduces faster. If a high steepness of 0.1 is anticipated, the reflected power decreases faster for negative elevations than for positive elevations.

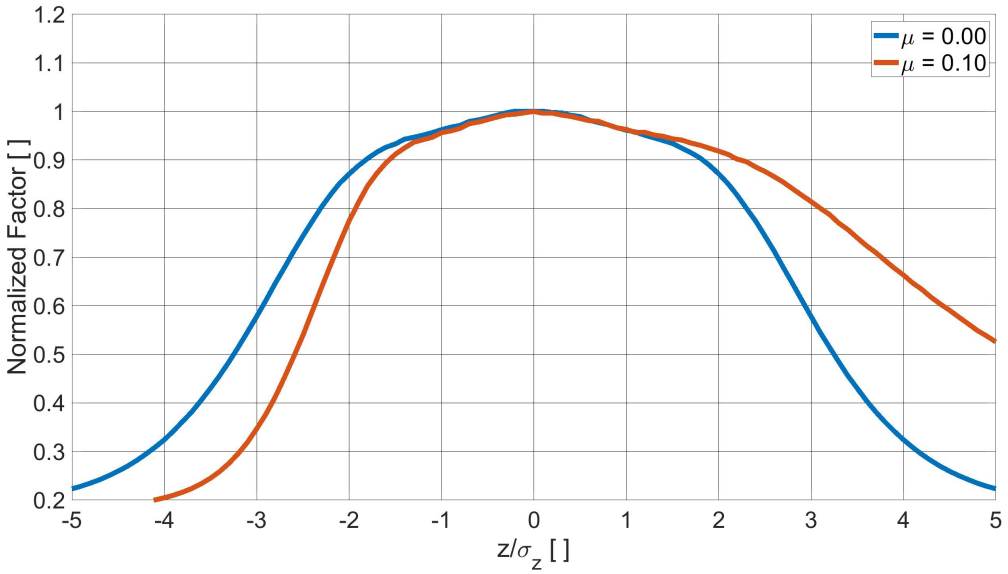

Figure 2.12: Product of E[|X|] and E[1/|X|] for different normalized elevations generated by Monte-Carlo simulations. The blue curve gives the case with $\mu = 0.0$ and the red curve shows the case for a value of $\mu = 0.1$.

The final missing formula that might have an elevation dependency is the joint probability density function of the first-order spatial derivatives. This formula is derived via the definition of a characteristic function, which is shown for the partial derivative in up-wind direction.

$$\begin{aligned}\varphi_{\eta_x|\eta}(v|z) &= \lim_{x\to 0}\int_{\mathbb{R}} \exp\left\{\frac{z_p + \frac{\mu}{2}z_p^2 - z - \frac{\mu}{2}z^2}{x}v\right\} p_{\eta_p|\eta}(z_p|z)dz_p \\ &\times \lim_{x\to 0}\int_{\mathbb{R}} \exp\left\{-\frac{i\mu}{2}\frac{z_p^2 - z^2}{x}v\right\} p_{\eta_p|\eta}(z_p|z)dz_p \\ &= \exp\left\{-\frac{1}{2}v^2\sigma_x^2(1 + 2\mu z + 2\mu^2 z^2)\right\} \end{aligned} \tag{2.84}$$

with η_p being a random variable describing the elevation at a surface location close to η and z_p is a realization of η_p.

From Eq. 2.84 it can be stated that $\eta_x|\eta$ follows a normal distribution with zero mean and a variance of $\sigma_x^2(1 + 2\mu z + 2\mu^2 z^2)$. Applying this to the cross-wind direction gives the joint PDF of the first-order spatial derivatives as:

$$p_{\eta_x,\eta_y|\eta}(z_x, z_y|z) = \frac{1}{2\pi\sigma_x^2(1 + 2\mu z + 2\mu^2 z^2)} \exp\left\{-\frac{z_x^2 + z_y^2}{2\sigma_x^2(1 + 2\mu z + 2\mu^2 z^2)}\right\} \tag{2.85}$$

In Eq. 2.85, an isotropic wind field was assumed as both η_x and η_y have the same variance here.

As it will be shown in chapter 5 $E[X]E\left[\frac{1}{X}\right]$ and $p_{\eta_x,\eta_y|\eta}$ will be multiplied with the PDF of the sea level elevation and vertical motion. The normalized result of the multiplications is shown in Figure 2.13, whereat I refers to $E[X]E\left[\frac{1}{X}\right]$ and $V = 1 + 2\mu z + 2\mu^2 z^2$ being the elevation part of the variance of the first-order spatial derivatives.

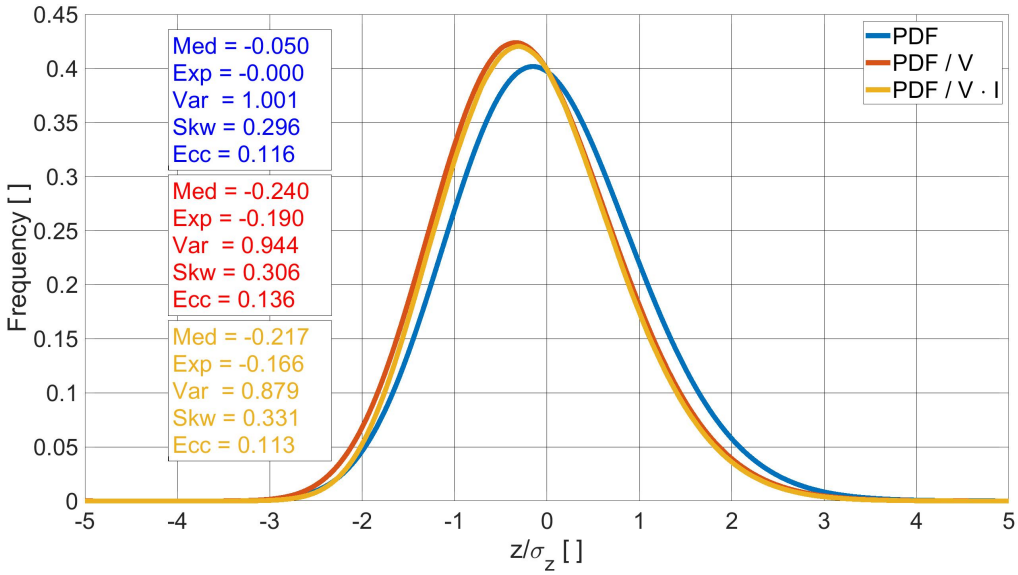

Figure 2.13: PDFs of the normalized surface elevations and their statistical parameters for $\mu = 0.1$. With Med being the median, Exp the expected value, Var the variance, Skw the skewness and Ecc the excess kurtosis. The blue curve gives the PDF of the elevation whereat the red one describes the PDF divided by the variance of first order spatial derivatives and the orange curve additionally includes the power factor I.

The blue curve in Figure 2.13 shows the PDF of the normalized sea surface elevation for a wave steepness of 0.1, where the text box with the blue text gives its stochastic parameters which are taken from table 2.3. The median is an important parameter as according to Chelton et al. [2001] this value corresponds to the sea level that the altimeter tracks. A value of -0.05 means that the altimeter would underestimate the sea level by 5% σ_z or 1.25% H_s if no wave steepness is considered in the retracker. The expected value is shown for the sake of completeness.

In the red curve of Figure 2.13 the variance of $p_{\eta_x,\eta_y|\eta}$ is also included, leading to a median value of -0.24, which corresponds to a sea level error of 6% H_s. Additionally the variance decreases from one to 0.944, which implies that the SWH will be estimated as about 3% too small. The skewness and excess remain approximately unaltered.

By additionally including the elevation-dependent backscattered power I, it can be seen on the orange curve of Figure 2.13 that this term has only a minor effect on the PDF. The sea level error reduces slightly from 6% to 5.5% H_s and the skewness increases by about ten percent. The main difference appears in the variance, which decreases from 0.944 to 0.876, meaning that the SWH will be estimated as about 6% too small.

This section can be concluded by introducing an additional term I and an elevation dependency in the joint PDF of surface slopes to the function of the radar cross section by setting

$$\sigma^0(\theta_i, z, z_{tt}) = \sigma_0 \sec(\theta_i)^4 p_{\eta_x,\eta_y|\eta}(\tan\theta_i|z) I(z) \tag{2.86}$$

with σ_0 the nominal radar cross section. In Eq. 2.86, an isotropic wind field is already considered by inserting the incidence angle in p_{η_x,η_y}. The new term $I(z) = E[X]E[1/X]$ is a function defining how the reflected intensity changes depending on the elevation. For $I(z) = 1$ and $\mu = 0$ Eq. 2.86 becomes the same as in Barrick [1968].

3 A Mode Consistent Retracker with Local Torus Sea Surface Representation and Vertical Wave Motion

In the past, several waveform models were introduced to the scientific community to retrieve geophysical parameters out of radar altimetry signals. For LRM, the current state of the art is the Brown-Hayne model (see Hayne [1980]), which assumes a circular antenna pattern and approximates the Point Target Response (PTR) as a Gaussian to find a fully-analytical solution of the integral equations, whereas for SAR waveforms the SAR Altimetry Mode Studies and Applications over Ocean, Coastal Zones and Inland Water (SAMOSA) model introduced by Ray et al. [2015] is mainly used. As in the Brown-Hayne model, a Gaussian PTR approximation is undertaken to derive an analytical solution, although it allows for an elliptical antenna pattern. Both of these state-of-the-art models are defined for their specific processing mode and cannot applied to another one.

The waveform model derived in this chapter is an extension of the Signal Model involving fast Numerical Convolutions (SINC) developed in Buchhaupt et al. [2018], which will allow a more realistic local sea surface representation by including a torus coordinate system. Additionally, it introduces vertical wave particle motion and it is mode consistent, which means it is usable for both LRM and SAR signals. The whole model will be defined in the frequency/slow-time domain, which means that the transform back into the time delay/Doppler frequency domain needs to be applied numerically. For this reason, the approach shown here is called semi-analytical.

This chapter is divided in three sections, whereas the first shows the waveform processing of LRMC the second gives the solution of the integral equations by using Fourier transforms. Finally, in the third section the computation of a SAR stack using the derived model is discussed, which includes the vertical wave motion.

3.1 LRMC Waveform Processing

Before starting with the waveform processing, it is necessary to find an analytical representation of the range and the relative velocity between the altimeter and a wave particle.

In torus coordinates, the squared range between two points is given as

$$\begin{aligned} r^2 &= (r_t + h_1)^2 + (r_t + h_2)^2 + 2R_t^2 + 2R_t(r_t + h_2)\cos p_2 \\ &- 2(r_t + h_1)(r_t + h_2)\sin p_2 \sin p_1 + 2R_t(r_t + h_1)\cos p_1 \\ &- 2(r_t + h_1)(R_t + (r_t + h_2)\cos p_2)\cos p_1 \cos(q_2 - q_1) \\ &- 2R_t(R_t + (r_t + h_2)\cos p_2)\cos(q_2 - q_1) \end{aligned} \tag{3.1}$$

where parameters with index 1 belong to the surface and with 2 to the satellite.

The cosine and sine terms in Eq. 3.1 can be simplified by using a Taylor series up to order two. This approximation is valid as the angles are small.

$$\cos p_1 \approx 1 - \frac{p_1^2}{2} \tag{3.2}$$

$$\sin p_1 \approx p_1 \tag{3.3}$$

$$\cos p_1 \cos(q_2 - q_1) \approx (1 - \frac{q_1^2}{2} - \frac{p_1^2}{2})\cos q_2 + q_1 \sin q_2 \tag{3.4}$$

Inserting the approximated trigonometric terms in Eq. 3.1 yields

$$r^2 \approx r_0^2 + \frac{p_1^2}{\kappa_1^2}\alpha_p + \frac{q_1^2}{\kappa_2^2}\alpha_q - 2\frac{p_1 \sin p_2}{\kappa_1^2}\beta_p - 2\frac{q_1 \sin q_2}{\kappa_2^2}\beta_q \tag{3.5}$$

with $\kappa_1 = \frac{1}{r_t}$ and $\kappa_2 = \frac{1}{R_t + r_t}$ being the principal curvatures of the reference torus, which defines the coordinate system. The other terms are defined as:

$$\begin{aligned}
r_0^2 &= h_2^2 + h_1^2 - 2h_1h_2 \cos p_2 \cos q_2 \\
&\quad +2r_t^2(1 - \cos p_2 \cos q_2)(1 + \kappa_1 h_1 + \kappa_1 h_2) \\
&\quad +2\tfrac{R_t}{\kappa_2}(1 - \cos q_2)(1 + \kappa_2(h_1 + (r_t + h_2)\cos p_2)) && (3.6)\\
\beta_p &= (1 + \kappa_1 h_1)(1 + \kappa_1 h_2) && (3.7)\\
\beta_q &= \kappa_2(R_t + (r_t + h_2)\cos p_2)(1 + \kappa_2 h_1) && (3.8)\\
\alpha_p &= \beta_p \cos p_2 \cos q_2 + \left(1 - \tfrac{\kappa_1}{\kappa_2}\right)(1 - \cos q_2)(1 + \kappa_1 h_1) && (3.9)\\
\alpha_q &= \beta_q \cos q_2 && (3.10)
\end{aligned}$$

The squared range can be further simplified by assuming that the angles p_2 and q_2 are small too. Additionally removing small terms with exponent higher than two yields

$$r^2 \approx h_2^2 - 2h_1h_2 + \alpha_p \left(\frac{p_1 - p_2}{\kappa_1}\right)^2 + \alpha_q \left(\frac{q_1 - q_2}{\kappa_2}\right)^2 \tag{3.11}$$

with $\alpha_p \approx 1 + h_2\kappa_1$ and $\alpha_q \approx 1 + h_2\kappa_2$ being the curvature factor in torus coordinates.

Introducing the platform and surface motion setting $h_2 = h_s + v_h t_s$, $p_2 = p_s + v_p t_s$, $q_2 = q_s + v_q t_s$ and $h_1 = z + z_t t_s + \frac{z_{tt}}{2} t_s^2$, $p_1 = p_i$, $q_1 = q_i$ and calculating the square root leads to

$$r(t_s) \approx h_s - z + \frac{\alpha_p}{2h_s}\left(\frac{p_i - p_s}{\kappa_1}\right)^2 + \frac{\alpha_q}{2h_s}\left(\frac{q_i - q_s}{\kappa_2}\right)^2 + v_h t_s - z_t t_s - \frac{z_{tt}}{2}t_s^2 - \frac{\alpha_p}{h_s}\left(\frac{p_i - p_s}{\kappa_1^2}\right)v_p t_s - \frac{\alpha_q}{h_s}\left(\frac{q_i - q_s}{\kappa_2^2}\right)v_q t_s \tag{3.12}$$

with v_h the vertical satellite velocity in torus coordinates,z the elevation, z_t the vertical wave particle velocity and z_{tt} the vertical wave particle acceleration. Horizontal wave motion is not considered as radar altimeters are nadir looking and the impact on the relative velocity would be insignificant as the satellite moves more than one thousand times faster compared with wave particles.

The relative velocity is now calculable by differentiation of Eq. 3.12 after the slow time:

$$v_r(t_s) \approx v_h - z_t - z_{tt}t_s - \frac{\alpha_p}{h_s}\left(\frac{p_i - p_s}{\kappa_1^2}\right)v_p - \frac{\alpha_q}{h_s}\left(\frac{q_i - q_s}{\kappa_2^2}\right)v_q \tag{3.13}$$

Inserting Eq. 3.12 and Eq. 3.13 into Eq. 2.6 yields

$$\Phi_S(t_f, t_s) \approx 2\pi i \left[\frac{2r(0) - 2r_{trk}}{c} s t_f - \frac{2v_r(0)}{\lambda_c}\left(t_s + t_f - \frac{s}{f_c} t_f t_s\right) + \frac{z_{tt}}{\lambda_c} {t_s}^2\right] \tag{3.14}$$

where Φ_S is the phase term of $S(t_f, t_s)$, which is defined in Eq. 2.6.

For the sake of readability, it is assumed that $r_{trk} \approx h$ and ignoring constant phase offset terms

$$\begin{aligned}\Phi_S(t_f,t_s) &\approx 2\pi i\left[\frac{\alpha_p}{ch_s}\left(\frac{p_i-p_s}{\kappa_1}\right)^2+\frac{\alpha_q}{ch_s}\left(\frac{q_i-q_s}{\kappa_2}\right)^2-\frac{2z}{c}\right]st_f+2\pi i\frac{z_{tt}}{\lambda_c}{t_s}^2\\ &- 2\pi i\left[\frac{2v_h}{c}-\frac{2z_t}{c}-\frac{2\alpha_p v_p}{ch_s}\left(\frac{p_i-p_s}{\kappa_1^2}\right)-\frac{2\alpha_q v_q}{ch_s}\left(\frac{q_i-q_s}{\kappa_2^2}\right)\right]\left[f_c\left(t_s+t_f\right)-st_ft_s\right]\end{aligned} \tag{3.15}$$

Accordingly, it is possible to derive the L1B processing of LRMC data. It is further assumed that the bursts are calibrated and aligned for different tracker ranges or AGC values.

Vertical Alignment

This step - which is performed directly after the calibration - corrects for vertical movement of the satellite within one burst. This is achieved by multiplying the burst with the complex conjugate of the satellite motion term leading to

$$D(t_f,t_s)=S(t_f,t_s)\cdot\exp\left\{2i\pi\frac{2}{\lambda_c}v_h\left(t_s-\frac{s}{f_c}t_ft_s\right)\right\} \tag{3.16}$$

In the L1B processing using real data in this step, range shifts are additionally applied to the bursts to align them for different tracker ranges. This is not shown here.

Along Track Fourier Transform

Whereas in L1B processing the along-track Fourier transform is applied via a matrix multiplication, in the model case a continuous Fourier transform is used. This transforms the burst from the fast time/slow time to the fast time/Doppler frequency (presented asf_D) domain.

$$\hat{D}(t_f,f_D)=\int_{-\infty}^{\infty}D(t_f,t_s)e^{-2i\pi f_D t_s}dt_s \tag{3.17}$$

For the sake of readability, the following function is defined describing a chirp signal

$$S_c(t_s)=\exp\left\{2\pi i\Delta f t_s+2\pi i\frac{z_{tt}}{\lambda_c}{t_s}^2\right\}\sqcap\left(\frac{t_s}{\tau_B}\right) \tag{3.18}$$

with $\Delta f=\frac{2}{\lambda_c}\left(z_t+\frac{\alpha_p(p_i-p_s)v_p}{h_s\kappa_1^2}+\frac{\alpha_q(q_i-q_s)v_q}{h_s\kappa_2^2}\right)$.

The result of this integral is not solvable with elemental functions as the vertical particle accelerations introduce an additional chirp signal. However, it is sufficient to keep the integral representation.

$$\begin{aligned}\hat{D}(t_f,f_D) &= \frac{\lambda_c G(\theta,\omega)\sqrt{\sigma^0(\theta,\omega)}}{\sqrt{(4\pi)^3}r^2}\exp\left\{2\pi i\left[\frac{\alpha_p}{ch_s}\left(\frac{p_i-p_s}{\kappa_1}\right)^2+\frac{\alpha_q}{ch_s}\left(\frac{q_i-q_s}{\kappa_2}\right)^2-\frac{2z}{c}\right]st_f\right\}\cdot\sqcap\left(\frac{t_f}{\tau_u}\right)\\ &\times \exp\left\{-2\pi i\left[\frac{2v_h}{c}-\frac{2z_t}{c}-\frac{2\alpha_p v_p}{ch_s}\left(\frac{p_i-p_s}{\kappa_1^2}\right)-\frac{2\alpha_q v_q}{ch_s}\left(\frac{q_i-q_s}{\kappa_2^2}\right)\right]f_ct_f\right\}\hat{S}_c(f_D)\end{aligned} \tag{3.19}$$

with $\hat{S}_c(f_D)$ being the Fourier transform of $S_c(t_s)$.

Range Compression

In L1B processing, the next step would be the range cell migration correction, which is not necessary here as it is applied later. Accordingly, the range compression is next, which is a Fourier transform in fast time domain

$$\hat{\hat{D}}(f_r, f_D) = \int_{-\infty}^{\infty} \hat{D}(t_f, f_D) e^{-2i\pi f_r t_f} dt_f \tag{3.20}$$

with f_r the frequency of the beat signal, which is related to the time-delay τ by $f_r = s\tau_r$ (see Egido and Smith [2016]). Inserting this into Eq. 3.20 and solving the integral yields

$$\hat{\hat{D}}(\tau_r, f_D) \approx \frac{\lambda_c G(\theta,\omega)\sqrt{\sigma^0(\theta,\omega)}}{\sqrt{(4\pi)^3 r^2}} \tau_u sinc\left\{s\tau_u\left[\tau_r - \Delta\tau + \Delta\tau_{D,0} - \Delta\tau_{D,i}\right]\right\} \hat{S}_c(f_D) \tag{3.21}$$

with
$\Delta\tau = \frac{\alpha_p}{ch_s}\left(\frac{p_i - p_s}{\kappa_1}\right)^2 + \frac{\alpha_q}{ch_s}\left(\frac{q_i - q_s}{\kappa_2}\right)^2 - \frac{2z}{c}$,
$\Delta\tau_{D,0} = \frac{2}{c}\frac{f_c}{s} v_h$ the time delay due to the Doppler effect independent on scatter coordinates and
$\Delta\tau_{D,i} = \frac{2}{c}\frac{f_c}{s}\left[\frac{\alpha_p(p_i - p_s)v_p}{h_s\kappa_1^2} + \frac{\alpha_q(q_i - q_s)v_q}{h_s\kappa_2^2}\right]$ the delay caused by the Doppler-effect with the elemental scatterers.
$\Delta\tau_{D,0}$ can be ignored in the further calculation as it causes a constant range offset of $\Delta r_{D,0} = \frac{c}{2}\Delta\tau_{D,0}$ which is applied after retracking as a Doppler correction.

$$\hat{\hat{D}}(\tau_r, f_D) \approx \frac{\lambda_c G(\theta,\omega)\sqrt{\sigma^0(\theta,\omega)}}{\sqrt{(4\pi)^3 r^2}} \tau_u sinc\left\{B\left[\tau_r - \Delta\tau - \Delta\tau_{D,i}\right]\right\} \hat{S}_c(f_D) \tag{3.22}$$

with B the bandwidth of the compressed pulse.

In the next step the power of the beams is retrieved by calculating the absolute square of the whole burst. As the analysis only includes one scattering area element located on a torus an integration over the whole torus surface, **S** is performed to include all other scatterers.

$$P(\tau_r, f_D) = \iiint_{\mathbb{R}^3} p_{\eta,\eta_t,\eta_{tt}}(z, z_t, z_{tt}) \iint_{\mathbf{S}} \|\hat{\hat{D}}(\tau_r, f_D)\|_2^2 d\mathbf{A} dz dz_t dz_{tt} \tag{3.23}$$

The second integral gives the variables z, z_t and z_{tt} the distribution as discussed in section 2.3.2 by multiplying the function $\hat{\hat{D}}$ with the joint PDF $p_{\eta,\eta_t,\eta_{tt}}(z, z_t, z_{tt})$ and integrating over the whole definition area of the distribution.

Accordingly, the stack is processed but without considering the the range cell migration correction. Due to the continuous analysis, a discussion about zero-padding was not necessary as only for the discrete case aliasing occurs. However, this issue will be discussed in chapter 6. A close form representation for the RMC is given in section 3.3.

The following section gives a closed form solution of Eq. 3.23 by transforming it from the time delay/Doppler frequency to the frequency/slow time domain using Fourier transforms.

As $\hat{S}_c(f_D)$ in Eq. 3.23 is not representable with elementary functions, a forward Fourier transform in the time delay and a backward Fourier transform in the Doppler frequency domain are applied before calculating the result.

Thereby, it is possible to solve the remaining integral in $\hat{\hat{D}}$ by using $\|\hat{\hat{D}}(\tau_r, f_D)\|_2^2 = \hat{\hat{D}}\hat{\hat{D}}^*$ with $\hat{\hat{D}}^*$ the complex conjugate of $\hat{\hat{D}}$ together with the convolution theorem, leading to

$$\int_{-\infty}^{\infty} S_c(t_s-\tau_s)S_c^*(-\tau_s)d\tau_s \quad = \quad \exp\left\{2\pi i\Delta f t_s\right\} sinc\left(\frac{4}{\lambda_c}z_{tt}t_s\left[t_s-\tau_B\right]\right)\tau_B \bigwedge\left(\frac{t_s}{\tau_B}\right) \tag{3.24}$$

with $\bigwedge$ denoting a triangular impulse function.

Inserting Eq 3.24 and the resulting formula of σ^0 derived in Eq. 2.86 in the forward Fourier transform in the time-delay and backward Fourier transform in the Doppler frequency of Eq 3.23 yields

$$\begin{aligned}\hat{\hat{P}}(f,t_s) \quad &= \quad \iiint\limits_{\mathbb{R}^3} p_{\eta,\eta_t,\eta_{tt}}(z,z_t,z_{tt})I(z)\, sinc\left(\frac{4}{\lambda_c}z_{tt}t_s\left[t_s-\tau_B\right]\right)e^{-2\pi i\frac{2f}{c}z+2i\pi\frac{2t_s}{\lambda_c}z_t}dzdz_tdz_{tt} \\ &\times \quad P\hat{\hat{T}}R(f,t_s)\iint\limits_{\mathbf{S}}\frac{{\lambda_c}^2G^2(x,y)\sigma_0\sec^4(\theta_i)p_{\eta_x,\eta_y}(\tan\theta_i)}{(4\pi)^3L_pr^4}e^{-2\pi i(\Delta\bar{\tau}+\Delta\tau_{D,i})f+2\pi i\Delta\bar{f}t_s}d\mathbf{A}\end{aligned} \tag{3.25}$$

with $\Delta\bar{\tau} = \frac{\alpha_p}{ch_s}\left(\frac{p_i-p_s}{\kappa_1}\right)^2+\frac{\alpha_q}{ch_s}\left(\frac{q_i-q_s}{\kappa_2}\right)^2$, $\Delta\bar{f} = \frac{2}{\lambda_c}\left(\frac{\alpha_p(p_i-p_s)v_p}{h_s\kappa_1^2}+\frac{\alpha_q(q_i-q_s)v_q}{h_s\kappa_2^2}\right)$ and $P\hat{\hat{T}}R(f,t_s)$ the two dimensional Fourier transform of the PTR.

Inserting $\sec^4(\theta_i) = \frac{r^4}{{h_s}^4}$, $\tan^2(\theta_i) = \frac{x^2+y^2}{{h_s}^2}$ and assuming the wave steepness μ to be negligible small in p_{η_x,η_y} yields

$$\begin{aligned}\hat{\hat{P}}(f,t_s) \quad &= \quad \iiint\limits_{\mathbb{R}^3} p_{\eta,\eta_t,\eta_{tt}}(z,z_t,z_{tt})I(z)\, sinc\left(\frac{4}{\lambda_c}z_{tt}t_s\left[t_s-\tau_B\right]\right)e^{-2\pi i\frac{2f}{c}z+2i\pi\frac{2t_s}{\lambda_c}z_t}dzdz_tdz_{tt} \\ &\times \quad P\hat{\hat{T}}R(f,t_s)\iint\limits_{\mathbf{S}}\frac{{\lambda_c}^2G^2(x,y)\sigma_0\exp\left\{-\frac{x^2+y^2}{2{h_s}^2{s_0}^2}\right\}}{(4\pi)^3L_p{h_s}^4}e^{-2\pi i(\Delta\bar{\tau}+\Delta\tau_{D,i})f+2\pi i\Delta\bar{f}t_s}d\mathbf{A}\end{aligned} \tag{3.26}$$

The two-dimensional Fourier transform of the point target response is given by using Bateman [1954, Eq. 1.6.8]:

$$P\hat{\hat{T}}R(f,t_s) = \frac{\tau_u^2}{B}\bigwedge\left(\frac{f}{B}\right)\tau_B\bigwedge\left(\frac{t_s}{\tau_B}\right) \tag{3.27}$$

The three-dimensional integral with respect to sea state parameters can be solved directly by using the definition of characteristic functions being the backward Fourier transform of the joint PDF by

$$\begin{aligned}P\hat{\hat{D}}F(f,t_s) \quad &= \quad \iiint\limits_{\mathbb{R}^3} p_{\eta,\eta_t,\eta_{tt}}(z,z_t,z_{tt})I(z)\,\mathrm{sinc}\left(\frac{2}{\lambda_c}z_{tt}t_s\left[t_s-\tau_B\right]\right)e^{-2\pi i\frac{2f}{c}z+2i\pi\frac{2t_s}{\lambda_c}z_t}dzdz_tdz_{tt} \\ &= \quad \int\limits_{-\infty}^{\infty}\varphi_{\eta,\eta_t,\eta_{tt}}\left(-2\pi\frac{2f}{c},2\pi\frac{2t_s}{\lambda_c},-w\right)\frac{\sqcap\left(\frac{w}{2\pi\frac{2}{\lambda_c}t_s[t_s-\tau_B]}\right)}{\sqrt{2\pi}\frac{2}{\lambda_c}t_s\left[t_s-\tau_B\right]}dw * \hat{I}\left(-2\pi\frac{2f}{c}\right)\end{aligned} \tag{3.28}$$

with $\hat{I}$ the Fourier transform if I and $*$ denoting a convolution.

For a wave field with very small wave steepness and under neglecting of the I term, Eq. 3.28 can be written as

$$P\hat{\hat{D}}F(f,t_s) = \exp\left\{-2\pi^2\sigma_s^2 f^2 - 2\pi^2\sigma_t^2 t_s^2\right\} \begin{cases} \sqrt{\pi}\exp\left\{\zeta_f^2\right\}\frac{\mathrm{erf}\left(\zeta_f+\zeta_t\right)-\mathrm{erf}\left(\zeta_f-\zeta_t\right)}{4\zeta_t} & \zeta_t \neq 0 \\ 1 & \zeta_t = 0 \end{cases} \tag{3.29}$$

with ζ_f and ζ_t being auxiliary variables defined as

$$\zeta_f = 2\sqrt{2}\pi\frac{\sigma_t^2}{\sigma_{tt}}\frac{f}{f_c} \tag{3.30}$$

$$\zeta_t = \frac{\pi}{\sqrt{2}}\sigma_{tt}t_s\left[\tau_B - t_s\right] \tag{3.31}$$

where $\sigma_s = \frac{2\sigma_z}{c}$, $\sigma_t = \frac{2\sigma_v}{\lambda_c}$, $\sigma_{tt} = \frac{2\sigma_a}{\lambda_c}$ and erf describing the error function.

This is interesting as the impact of wave particle motion depends on the central wavelength of an emitted radar signal. The shorter the carrier wave length the greater the impact on the received stack. This means that the observable effect of these is about three times higher in the Ka-band ($\lambda_c \approx 8$ mm) compared with the Ku-band ($\lambda_c \approx 22$ mm).

In Eq. 3.29 the acceleration part of the function is a slowly decaying compared with the expontential parts if the burst duration is small. Therefore, it is negligible in the unfocused SAR case as t_s varies typically between ± 3.5 ms. In the fully-focused SAR case, this does not apply, possibly leading to the necessity to include accelerations.

To summarize Eq. 3.25 can be rewritten as

$$\hat{\hat{P}}(f,t_s) = P\hat{\hat{D}}F(f,t_s)\cdot P\hat{\hat{T}}R(f,t_s)\cdot F\hat{\hat{S}}SR(f,t_s) \tag{3.32}$$

$$F\hat{\hat{S}}SR(f,t_s) = \frac{{\lambda_c}^2\sigma_0}{(4\pi)^3 L_p {h_s}^4}\iint_{\mathbf{S}} G^2(x,y)\exp\left\{-2\pi i([\Delta\bar{\tau}+\Delta\tau_{D,i}]f - \Delta\bar{f}t_s) - \alpha_0\frac{x^2+y^2}{{h_s}^2}\right\}dA \tag{3.33}$$

with $F\hat{\hat{S}}SR(f,t_s)$ the Flat Sea Surface Response (FSSR) in the frequency/slow time domain and $\alpha_0 = \frac{1}{2s_o^2}$.

Eq. 3.33 is a solvable integral equation after transforming p_2, q_2, v_p and v_q to the same Cartesian coordinate system as the antenna gain function by setting

$$x_i' = \frac{p_i}{\kappa_1},\ x_s' = \frac{p_s}{\kappa_1},\ v_x' = \frac{v_p}{\kappa_1}$$
$$y_i' = \frac{q_i}{\kappa_2},\ y_s' = \frac{q_s}{\kappa_2},\ v_y' = \frac{v_q}{\kappa_2}$$

which yields

$$\Delta\bar{\tau} = \frac{\alpha_p}{ch_s}\left(x_i'-x_s'\right)^2 + \frac{\alpha_q}{ch_s}\left(y_i'-y_s'\right)^2 \tag{3.34}$$

$$\Delta\tau_{D,i} = \frac{2}{ch_s}\frac{f_c}{s}\left[\alpha_p(x_i'-x_s')v_x' + \alpha_q(y_i'-y_s')v_y'\right] \tag{3.35}$$

$$\Delta\bar{f} = \frac{2}{\lambda_c h_s}\left(\alpha_p v_x'(x_i'-x_s') + \alpha_q v_y'(y_i'-y_s')\right) \tag{3.36}$$

Transforming (x', y') to the coordinate system of the platform (x, y) by setting $x' = x\cos\Omega - y\sin\Omega$ and $y' = x\sin\Omega + y\cos\Omega$ leads to a zero velocity in y direction as the platform moves only in x in its own coordinate system, whereas Ω is the course angle. This leads to

$$\Delta\bar{\tau} \approx \frac{\alpha_x(x-x_s)^2}{ch_s} - 2\frac{\alpha_{xy}(x-x_s)(y-y_s)}{ch_s} + \frac{\alpha_y(y-y_s)^2}{ch_s} \tag{3.37}$$

$$\Delta\tau_{D,i} \approx \frac{2\alpha_x f_c v_x}{ch_s}\left[x - x_s - \frac{\alpha_{xy}}{\alpha_x}(y-y_s)\right]\frac{1}{s} \tag{3.38}$$

$$\Delta\bar{f} \approx \frac{2\alpha_x f_c v_x}{ch_s}\left[x - x_s - \frac{\alpha_{xy}}{\alpha_x}(y-y_s)\right] \tag{3.39}$$

with x_s, y_s denoting horizontal coordinate shifts of the platform due to surface slopes and the alpha variables being the curvature coefficients, defined as:

$$\alpha_x = 1 + h_s\left[\cos^2(\Omega)\kappa_1 + \sin^2(\Omega)\kappa_2\right] \tag{3.40}$$

$$\alpha_y = 1 + h_s\left[\sin^2(\Omega)\kappa_1 + \cos^2(\Omega)\kappa_2\right] \tag{3.41}$$

$$\alpha_{xy} = h_s\sin(\Omega)\cos(\Omega)\left(\kappa_1 - \kappa_2\right) \tag{3.42}$$

$$\Omega = \arctan 2(v_y', v_x') \tag{3.43}$$

For $\kappa_1 = \kappa_2$ this converges to the spherical state-of-the-art approach introduced in Chelton et al. [1989, Appendix A].

The FSSR function in the time delay/Doppler frequency domain can be determined by performing a two-dimensional inverse Fourier transform and using the approach in Buchhaupt et al. [2018, Eq. 11]

$$FSSR(\tau_r, x_D) = \frac{{\lambda_c}^2\sigma_0}{(4\pi)^3 L_p {h_s}^4}\frac{c^2{h_s}^2}{4(\alpha_x\alpha_y - \alpha_{xy}^2)f_c v_x}\sum_{i=1}^{2} G(x_i + x_s, y_i + y_s)\frac{\exp\left\{-\alpha_0\frac{(x_i+x_s)^2+(y_i+y_s)^2}{{h_s}^2}\right\}}{y_0}U(y_0^2) \tag{3.44}$$

with U the Heaviside step function and x_1, x_2, y_1, y_2 are functions depending on the along-track coordinate of the scattering area x_D and the time delay τ_r given by

$$x_i = x_D + \frac{\alpha_{xy}}{\alpha_x}y_i \tag{3.45}$$

$$y_i = \sqrt{\frac{\alpha_x\alpha_y}{\alpha_x\alpha_y - \alpha_{xy}^2}}\left[(-1)^i y_0 - \frac{\alpha_{xy}f_c v_x}{\alpha_y s}\right] \tag{3.46}$$

$$y_0 = \sqrt{\frac{ch_s}{\alpha_y}}\sqrt{\tau_r - \frac{f_D}{s} - \frac{\alpha_x}{ch_s}x_D^2 + \frac{\alpha_y}{ch_s}\left(\frac{\alpha_{xy}f_c v_x}{\alpha_y s}\right)^2} \tag{3.47}$$

where $x_D = \frac{ch_s}{2\alpha_x f_c v_x}f_D$. It is important to note that Eq. 3.44 becomes infinite for $y_0 \to 0$, which makes it impossible to start in this domain directly.

To compute Eq. 3.44 a representation for the antenna gain function needs to be found first. Following Brown [1975, Appendix B] the antenna pattern of a radar altimeter can be expressed as the product of two squared cardi-

nal sine functions, which can be approximated with a good accuracy by a Gaussian antenna characteristic (see Brown [1975, Appendix B])

$$\begin{aligned} G(\theta,\omega) &= G_0 \frac{\sin^2(a\sin\theta\cos\omega)}{(a\sin\theta\cos\omega)^2}\frac{\sin^2(b\sin\theta\sin\omega)}{(b\sin\theta\sin\omega)^2} \\ &\approx G_0 \exp\left\{-a^2\sin^2\theta\cos^2\omega\right\}\exp\left\{-b^2\sin^2\theta\sin^2\omega\right\} \end{aligned} \tag{3.48}$$

with G_0 the nominal antenna gain, a parameter related with the along-track half power beam width Θ_{3dBx} and b a parameter related with the across track half power beam width Θ_{3dBy} given by

$$a = \frac{\sqrt{\ln(2)}}{\sin(\Theta_{3dBx}/2)} = \sqrt{\frac{2}{\gamma_x}} \tag{3.49}$$

$$b = \frac{\sqrt{\ln(2)}}{\sin(\Theta_{3dBy}/2)} = \sqrt{\frac{2}{\gamma_y}} \tag{3.50}$$

To use the antenna gain function, it is necessary to transform it from a polar coordinate system to a Cartesian one by using the geometry of θ and ω, shown in Fig. 3.1.

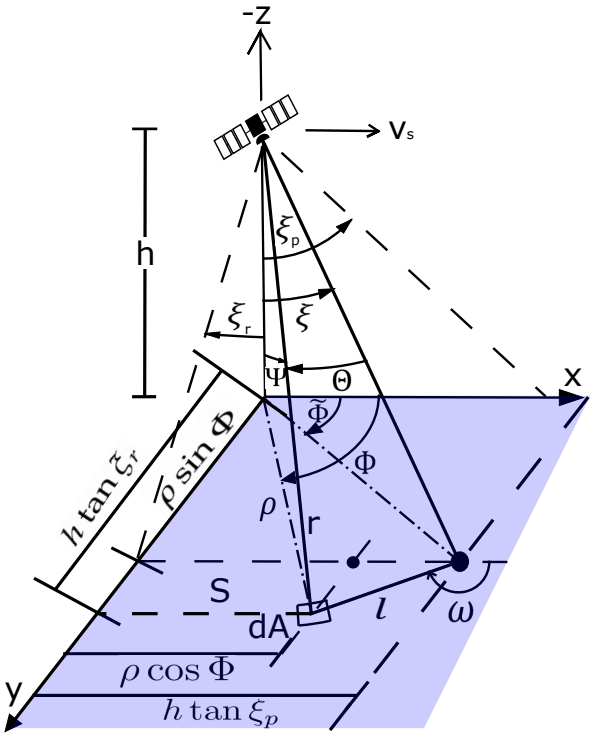

Figure 3.1: Geometry for calculating the antenna characteristic function G in Cartesian coordinates. l is an auxiliary variable to determine the angles θ and ω of the area element dA as a function of x and y coordinates

Using the same geometric approaches as described in Brown [1975, Appendix A] and Buchhaupt et al. [2018] and applying a counter clockwise rotation around the z-axis to include the yaw mispointing yields

$$a\sin\theta\cos\omega = a\cos\xi_y\frac{x - y\tan\xi_y - x_p\sec\xi_y - y_s\tan\xi_y + x_s}{h_s} = a\cos\xi_y\frac{x - y\tan\xi_y + \Delta x}{h_s} \tag{3.51}$$

$$b\sin\theta\sin\omega = b\cos\xi_y\frac{y + x\tan\xi_y - y_p\sec\xi_y + x_s\tan\xi_y + y_s}{h_s} = b\cos\xi_y\frac{y + x\tan\xi_y + \Delta y}{h_s} \tag{3.52}$$

with ξ_p the pitch angle, ξ_r the roll angle, ξ_y the yaw angle, $x_p = h_s \tan \xi_p$ and $y_p = h_s \tan \xi_r$. In the equations above the surface slope is already applied. Inserting these in Eq. 3.33 and solving the integrals using Gradshteyn and Ryzhik [2007, Eq. 3.323 2.10] yields

$$\hat{FSSR}_D(f, t_s) = \frac{A}{\sqrt{s_x s_y - s_{xy}^2}} \exp\left\{ \frac{s_y \zeta_x^2 + s_x \zeta_y^2 + 2\zeta_x \zeta_y s_{xy}}{s_x s_y - s_{xy}^2} \right\} \tag{3.53}$$

with $A = \frac{G_0^2 \sigma_0 {\lambda_c}^2 c}{4(4\pi)^2 \sqrt{\alpha_x \alpha_y} L_p {h_s}^3} \exp\left\{ -\alpha_0 \frac{x_s^2 + y_s^2}{{h_s}^2} - \Delta\sigma_{0,\xi} \right\}$.

A solution for CA waveforms can be found by $\hat{FFSR}_C(f) = \hat{FSSR}_D(f, 0)$ (see Buchhaupt et al. [2018]). As for SAR altimetry, it is often convenient to start in the f/f_D domain, whereby this formula is given here as

$$\hat{FSSR}(f, f_D) = \frac{K \exp\left\{ -2\pi i \frac{f}{s} f_D - \frac{\alpha_x}{ch_s} s_x x_D^2 + 2\sqrt{\frac{\alpha_x}{ch_s}} x_D \right\}}{\sqrt{s_y + \frac{\alpha_{xy}^2}{\alpha_x \alpha_y} s_x + 2\frac{\alpha_{xy}}{\sqrt{\alpha_x \alpha_x}} s_{xy}}} \exp\left\{ \frac{\left[\beta_y - \frac{\alpha_{xy}}{\sqrt{\alpha_x \alpha_y}} \beta_x + \sqrt{\frac{\alpha_x}{ch_s}} \left(\delta_{xy} + \frac{\alpha_{xy}}{\sqrt{\alpha_x \alpha_y}} \delta_x \right) x_D \right]^2}{s_y + \frac{\alpha_{xy}^2}{\alpha_x \alpha_y} s_x + 2\frac{\alpha_{xy}}{\sqrt{\alpha_x \alpha_x}} s_{xy}} \right\} \tag{3.54}$$

with $K = \sqrt{\frac{\alpha_x}{ch_s}} \frac{ch_s}{2\alpha_x f_c \nu_x} A$.

The parameters in Eq. 3.53 and 3.54 are defined by

$$\zeta_x = \beta_x + 2\pi i \sqrt{\frac{\alpha_x}{ch_s}} f_c \nu_x \left[\frac{f}{s} + t_s \right] \tag{3.55}$$

$$\zeta_y = \beta_y - 2\pi i \sqrt{\frac{\alpha_y}{ch_s}} \frac{\alpha_{xy}}{\alpha_y} f_c \nu_x \left[\frac{f}{s} + t_s \right] \tag{3.56}$$

$$\beta_x = 2a^2 \sqrt{\frac{c}{\alpha_x h_s}} \cos^2 \xi_y \frac{\Delta x + \frac{b^2}{a^2} \tan \xi_y \Delta y}{h_s} + \sqrt{\frac{c}{\alpha_x h_s}} \alpha_0 \tag{3.57}$$

$$\beta_y = 2b^2 \sqrt{\frac{c}{\alpha_y h_s}} \cos^2 \xi_y \frac{\Delta y - \frac{a^2}{b^2} \tan \xi_y \Delta x}{h_s} + \sqrt{\frac{c}{\alpha_y h_s}} \alpha_0 \tag{3.58}$$

$$s_x = \delta_x + 2\pi i f = 2a^2 \frac{c}{\alpha_x h_s} \cos^2 \xi_y \left[1 + \frac{b^2}{a^2} \tan^2 \xi_y \right] + \frac{c}{\alpha_x h_s} \alpha_0 + 2\pi i f \tag{3.59}$$

$$s_y = \delta_y + 2\pi i f = 2b^2 \frac{c}{\alpha_y h_s} \cos^2 \xi_y \left[1 - \frac{a^2}{b^2} \tan^2 \xi_y \right] + \frac{c}{\alpha_y h_s} \alpha_0 + 2\pi i f \tag{3.60}$$

$$s_{xy} = \delta_{xy} + 2\pi i \frac{\alpha_{xy}}{\sqrt{\alpha_x \alpha_y}} f = 2[a^2 - b^2] \frac{c}{\sqrt{\alpha_x \alpha_y} h_s} \sin(2\xi_y) + 2\pi i \frac{\alpha_{xy}}{\sqrt{\alpha_x \alpha_y}} f \tag{3.61}$$

$$\Delta\sigma_{0,\xi} = 2a^2 \frac{\Delta x^2}{{h_s}^2} \cos^2 \xi_y \left[1 + \frac{b^2}{a^2} \tan^2 \xi_y \right] + 2b^2 \frac{\Delta y^2}{{h_s}^2} \cos^2 \xi_y \left[1 - \frac{a^2}{b^2} \tan^2 \xi_y \right] \tag{3.62}$$

With Eq. 3.53 and Eq. 3.54, a fully-analytical stack or waveform model is defined but the measured stack or waveform is given in the time delay/Doppler frequency domain. This means numerical Fourier transforms needs to be applied during the retracking to achieve modelled signals in the correct domain. This will be discussed in the following section.

This section provides a step-by-step instruction how to calculate a stack and its partial derivatives if vertical wave particle motion is included in the SAR and LRMC case. A detailed discussion for CA and for SAR with a frozen sea is given in Buchhaupt et al. [2018]. The motivation of this is to include the model in a retracking procedure that shall estimate geophysical parameters.

The noise of a radar altimetry stack follows an exponential distribution with good approximation, although the least squares approach usually used in retracking assumes a normal distribution of the signal. The minimization problem involves finding the minimum of the negative log-likelihood function for a multivariate normal distribution [Bjerhammar, 1973, Section 2.19]

$$\mathbf{P}_X \rightarrow \min_{\mathbf{P}_X} \sum_{k=1}^{\bar{N}} \sum_{\bar{l}=1}^{\bar{L}} (y_{k,\bar{l}} - s_{k,\bar{l}})^2 \tag{3.63}$$

with n the number of free parameters to be estimated, $\bar{N}$ the number of considered time delay samples, $\bar{L}$ the number of considered Doppler beams, $y_{k,\bar{l}}$ the measured stack with indexes k, l and $s_{k,\bar{l}}$ the modelled stack as a function of parameter vector $\mathbf{P}_X$.

To solve Eq. (3.63) efficiently, many solvers need the design matrix $J_{k,i}$ of the objective function which is defined as followings:

$$J_{k,\bar{l},i} = \frac{\partial (y_{k,\bar{l}} - s_{k,\bar{l}})}{\partial \mathbf{P}_{Xi}} = -\frac{\partial s_{k,\bar{l}}}{\partial \mathbf{P}_{Xi}} \tag{3.64}$$

The parameters actually estimated in this study are the epoch with respect to the tracking reference point, significant wave height, the standard deviation of the vertical wave particle velocity and amplitude. However, the SINC can also be used in retrackers estimating other parameters, like antenna orientation, root mean square of surface slope or wave steepness.

The two parameters epoch t_0 and amplitude A are directly included in the expression of the retracker using SINC. For the parameters SWH and σ_v three approaches exist.

1. Set $\sigma_s^2 = \left(\frac{H_s}{2c}\right)^2$ which is used in most retrackers
2. Estimate σ_s^2 as a free parameter and set $H_s = \Re(\sigma_s) - \Im(\sigma_s)$ after the optimization
3. Set $\sigma_s^2 = sgn(\sigma_s) \cdot \sigma_s^2$, estimate σ_s as a free parameter and calculate $H_s = 2c\sigma_s$ afterwards

where sgn denotes the sign function [Papoulis, 1977, Section 1-2], $\Re(z)$ the real part and $\Im(z)$ the imaginary part of a complex number z.

One drawback of the first approach is that with the PDF being an even function with respect to SWH, the retracker cannot distinguish between positive and negative SWH values. The SWH is biased for small SWH values, as negative SWH are not allowed but could occur in reality due to noise in the retrieved signal. The second and third approaches allow negative SWH values instead. The third is preferable as the optimization algorithm required in the estimation converges with fewer iteration without loss of accuracy and precision. For σ_t, a similar procedure is chosen by setting $\sigma_t^2 = sgn(\sigma_t) \cdot \sigma_t^2$ and calculating $\sigma_v = \frac{\lambda_c}{2}\sigma_t$ after the retracking of the stack.

With the set of parameters to be estimated defined above, the next two subsections describe an efficient way to compute the modelled stack $(s_{k,\bar{l}})$ and its partial derivatives.

First, it needs to be considered in which domain the computation shall start and how the azimuthal PTR will be considered. Analytical expressions exist for this case, although the evaluation of the special functions involved is slower than a numerical way via Fourier transforms together with the RMC and Fourier transform matrix. These are described below.

For the sake of efficient and correct implementation, the calculation will start in the frequency/Doppler frequency domain with Eq. (3.54), which is going to be evaluated at discrete samples as follows

$$\hat{p}_{n,l} = F\hat{S}\hat{S}R_D\left(f_n, f_{D_l}\right) \tag{3.65}$$

with

$$f_n = \frac{O_t B}{N} n \tag{3.66}$$

where O_t is the oversampling factor in time delay samples, B the bandwidth and $N = N_s O_t N_t$ the total number of calculated samples with N_s the number of samples in the L1A product and N_t the receiving window widening factor to avoid aliasing (see Buchhaupt et al. [2018]) and

$$f_{D_l} = \begin{cases} \frac{f_p}{L} l & , \text{for } l \leq \frac{L}{2} \\ \frac{f_p}{L}\left(l - \frac{L}{2}\right) & , \text{for } l > \frac{L}{2} \end{cases} \tag{3.67}$$

where $L = N_p O_x$, $\{l \in \mathbb{N} | l \leq L\}$ is the total number of calculated beams, f_p the pulse repetition frequency, N_p the number of pulses per burst and O_x the oversampling factor in azimuth direction.

As the PTR functions should to be applied in the frequency/slow time domain, an inverse complex to complex Fourier transform of $\hat{p}_{n,l}$ needs to be performed with input $\hat{p}_{n,l} \cdot e^{-i\pi \frac{(L-1)}{L}(l-\frac{L}{2})}$ and output $\hat{\hat{p}}_{n,m}$. The phase shift of $\hat{p}_{n,l}$ is necessary to shift the origin $t_s = 0$ to the centre of $\hat{\hat{p}}_{n,m}$.

The azimuthal and time delay PTR can then be applied with element-wise multiplications

$$\hat{\hat{q}}_{n,m} = \hat{\hat{p}}_{n,m} \cdot P\hat{T}R_x\left(t_{s_m}\right) \cdot P\hat{T}R_\tau(f_n) \tag{3.68}$$

with $t_{s_m} = \left(m - \frac{M-1}{2}\right) \frac{1}{N_x f_p}$, $M = L$, m having the same definition area as l and N_x the azimuth widening factor.

The result of Eq. 3.68 is stored in the Random-Access Memory (RAM) of the computing system as a constant input. Additionally, the Fourier transform matrix and the RMC matrix can also be computed outside of the iterations as they do not change within the retracking of one stack or waveform.

The Fourier transformation matrix is defined by

$$(w_{m,\bar{l}}) = \exp\left\{-2\pi i \boldsymbol{t_s} \otimes \boldsymbol{f_D}\right\} \tag{3.69}$$

where the exponential function is applied element-wise to the matrix argument. $\boldsymbol{t_s} \in \mathbb{R}^L$ describes a vector containing the t_{s_m} values, $\otimes$ describing a dyadic product and $\boldsymbol{f_D} \in \mathbb{R}^{\bar{L}}$ another vector containing the Doppler frequencies of the beams extracted from the DDA L1B dataset.

The RMC matrix is defined as

$$(r_{n,\bar{l}}) = \exp\left\{2\pi i \boldsymbol{f} \otimes \left[\left(\frac{c h_s \boldsymbol{f_D}}{2 f_c \alpha_x v_x}\right)^{\textcircled{2}} + \frac{\boldsymbol{f_D}}{s}\right]\right\} \tag{3.70}$$

where the circles around the exponents denote that they are applied on each element of the vectors/matrices separately. This notation is similar to the Hadamard product, which shows a circled multiplication symbol.

Computations Within the Iterations

The calculation within the iterations is divided into several steps.

1. Calculate $\hat{\hat{s}}_{n,m} = \hat{\hat{q}}_{n,m} \cdot P\hat{\hat{D}}F(f_n, t_{s_m}) \cdot e^{-2i\pi t_0 f_n}$
   where the exponential term shifts the whole stack in time delay direction by t_0 which is the estimated epoch.
2. Perform a discrete Fourier in the azimuth direction with a matrix multiplication $(\hat{s}_{n,\bar{l}}) = (\hat{\hat{s}}_{n,m}) \cdot (w_{m,\bar{l}})$.
3. Apply the RMC by $(\hat{\hat{s}}_{n,\bar{l}}) = (\hat{s}_{n,\bar{l}}) \odot (r_{n,\bar{l}})$, with $\odot$ being the Hadamard product.
4. Perform a complex to real FFT in frequency direction with input $(\hat{\hat{s}}_{n,\bar{l}})$ and output $(s_{k,\bar{l}})$.
5. Only keep the first $\bar{N}$ necessary samples for each beam $\bar{l}$ and apply the stack mask $M_{k,\bar{l}}$ with a Hadamard product,

where the stack mask is calculated with two auxiliary variables δr_k^+ and δr_k^- by

$$M_{k,\bar{l}} = [\delta r_k^+ > \delta R_{\bar{l}}] \cdot [\delta r_k^- > -\delta R_{\bar{l}}] \tag{3.71}$$

where the rectangular brackets return one if their argument is true and zero otherwise. The objective of this mask is to eliminate the power "outside" the receiving window in the stack processing and is used during retracking.

They auxiliary variables are defined as:

$$\delta r_k^+ = \frac{c}{2} \cdot \frac{O_t}{B} \cdot (O_t N_s - k) \tag{3.72}$$

$$\delta r_k^- = \frac{c}{2} \cdot \frac{O_t}{B} \cdot (k - 1) \tag{3.73}$$

These steps can be adopted for the partial derivatives of $s_{k,\bar{l}}$ after the estimated parameters too by inserting the derivative instead. These are given for the discrete case by the following equations:

$$\frac{\partial(\hat{\hat{s}}_{n,m})}{\partial K} = \frac{(\hat{\hat{s}}_{n,m})}{K} \tag{3.74}$$

$$\frac{\partial(\hat{\hat{s}}_{n,m})}{\partial t_0} = -2\pi i \boldsymbol{f} \odot (\hat{\hat{s}}_{n,m}) \tag{3.75}$$

$$\frac{\partial(\hat{\hat{s}}_{n,m})}{\partial \sigma_s} = -4|\sigma_s|\pi^2 \boldsymbol{f}^{\textcircled{2}} \odot (\hat{\hat{s}}_{n,m}) \tag{3.76}$$

$$\frac{\partial(\hat{\hat{s}}_{n,m})}{\partial \sigma_t} = -4|\sigma_t|\pi^2 \boldsymbol{t_s}^{\textcircled{2}} \otimes \left[1 + \frac{f}{f_c}\right] \odot (\hat{\hat{s}}_{n,m}) \tag{3.77}$$

If thermal noise was removed from the measured stack, then this also needs to be applied to all of the equations to preserve consistency.

4.1 Mission and L1B Processing Parameters

As this study uses CryoSat-2 SAR mode L1A data, Table 4.1 shows the parameter of this mission. They are chosen to be consistent with the SARvatore processor prototype available at the G-POD service from the European Space Research Institute (ESRIN).

Symbol	Description	Value
G_0	Nominal antenna gain	42.6 dB
s	Negative chirp slope	7.1438 $MHz/\mu s$
f_c	Central frequency	13.575 GHz
f_p	Pulse repetition frequency	18.181 kHz
f_B	Burst repetition frequency	80 Hz
Θ_{3dBx}	Half power beam width along-track	1.10°
Θ_{3dBy}	Half power beam width across-track	1.22°
B	Bandwidth	320 MHz
τ_p	Pulse width	49.0 μs
τ_u	Usable pulse width	44.8 μs
τ_b	Burst duration	3.5 ms
N_s	Number of samples per echo	128
N_p	Number of pulses per burst	64
g_0	Tracker reference gate (oversampled waveform)	68
N_t	Time delay window widening factor	6
N_x	Azimuth window widening factor	2
h_N	Nominal altitude above reference ellipsoid	735 km
v_N	Nominal magnitude of the satellite velocity	7498 m/s
R_c	Nominal local earth curvature radius	6371 km

Table 4.1: Summary of CryoSat-2 mission parameters used.

Table 4.1 is divided in three parts, the first of which provides parameters according to the antenna characteristics, the emitted pulse and the number of samples built for each dimension. The tracker reference gate g_0 can be chosen arbitrarily, although in this study it is consistent with the value of the Radar Altimeter Data System (RADS) RDSAR processor prototype. The second part gives the widening factors used in the L2 processing to avoid aliasing effects of the PDF, which were chosen according to Buchhaupt et al. [2018]. Finally, the third part shows nominal orbit parameters, which are not used during the L1B or L2 processing as they can be extracted from the L1A data for each burst location. However, they will be used to appraise some measures such as the azimuthal PTR width in chapter 5.

In the L1B processing of SAR mode data, several options exist to calculate stacks or waveforms. The following enumeration shows the processing options considered in this study. Of course, more exist - e.g. applying a window function before each FFT - although in the open ocean the ones given here have the most significant impact on the geophysical parameters retrieved.

1. Processing modes
   a) RDSAR as a proxy for LRM.
   b) LRMC, which is SAR processing but without performing a beam steering to dedicated surface locations. This leads to a precision of SAR mode but a RDSAR footprint.
   c) SAR which presents unfocused SAR processing in this study.

   All three processing modes are used in this study.

2. Sea surface sampling rate
   Describes the time interval between each consecutive surface location, whereby 20, 40 and 80 Hz are supported. Of course, in SAR processing this measure can be chosen arbitrarily, although then the consistency between the two other modes vanishes as these only support the three options mentioned here. By default, 20 Hz is chosen unless stated otherwise. Chapter 5 discusses different surface sampling rates and how these affect the geophysical parameters retrieved.

3. Oversampling the bursts before the FFTs by a factor two to avoid aliasing caused by the PTR. This parameter is always true, which means that zero-padding is applied leading to $O_t = 2$ and $O_x = 2$.

4. Local sea surface representation
   a) Sphere, which is the current state of the art. No slopes and curvature effects are considered.
   b) Slopes, which calculates x_s and y_s by using spherical harmonics. Curvatures are not considered, which means $\alpha_x = \alpha_y = 1 + \frac{h_s}{R_c}$ and $\alpha_{xy} = 0$.
   c) Geoid, which considers both slopes and curvatures retrieved from spherical harmonics.

   Unless stated otherwise, Geoid is the default option.

5. Skewness of pulse or stack samples. This parameter decides whether a variable transform is applied for each sample to change its distribution from exponential to symmetric Weibull. This will be discussed in chapter 7. By default, this value is set to false, which means that no variable transform is performed.

These are processing options for open ocean processing. Another consideration for open ocean processing would be the implementation of amplitude and dilation compensation, which assimilates the outer beams to a similar shape as the central beam to achieve a higher signal-to-noise-ratio of the multi-looked waveform, (see Ray et al. [2015]). For coastal areas, other additional processing steps are applicable such as multiplying a Hamming window before each FFT to reduce the power of the PTR side-lobes or increasing the time delay window length to avoid loss of information due to the RMC (see Dinardo et al. [2018]). However, these will not be considered in this study.

First, the parameters used in the further chapters are introduced, namely sea level anomaly, sea surface height, significant wave height, standard deviation of vertical wave particle velocity and backscatter coefficient. Although for ocean studies wind speed is ultimately more interesting than the radar cross section, the comparison of σ_0 allows a direct validation of the retracker output and therefore is preferable. The variable α_0 related to the mean square slope is set to zero. However, in the following it is still included for the sake of completeness.

The sea level anomaly h_{SLA} is calculated as

$$h_{SLA} = h_s - (R - \Delta R) - \Delta h_{corr} - h_{mss} = h_{SSH} - h_{mss} \tag{4.1}$$

with

- R the one-way range from the satellite centre of mass to the closest scatterer on the surface calculated with

$$R = r_{trk} + \left(t_0 - \frac{g_0}{O_t B}\right)\frac{c}{2} \tag{4.2}$$

  where $g_0 = 68$ for oversampled and $g_0 = 34$ for non oversampled waveforms.

- ΔR the instrumental range bias which is set to 0.698 m for CryoSat-2 [Fenoglio-Marc et al., 2015, Eq. 3].

- Δh_{corr} the range offset caused by atmospheric and geophysical effects.

- h_{mss} the height of the mean sea surface.

- h_{SSH} the sea surface height above the reference ellipsoid.

As the validation metric uses the standard deviation of the difference between SLA products, the height offsets Δh_{corr} and h_{mss} are not relevant as long they are the same for all products. The mean sea level is applied to estimate more realistic standard deviations of the sea surface height, which do not include sea level changes due to the geoid and currents. In this study, the DTU15 mean surface is used (see Andersen et al. [2016]). The atmospheric and geophysical corrections are extracted from the L1A data.

The SWH is calculated by multiplying the estimated value of σ_s with two times the speed of light and $\sigma_v = \frac{\lambda_c}{2}\sigma_t$.

The computation of the backscatter coefficient depends on the L1B processor and how the model is integrated into a retracker. Therefore, the following description is specific for the retrackers mentioned in this study. The backscatter coefficient computation can be described by

$$\sigma_{0,dB} = G_{amp} + G + \Delta\sigma_{0,dB} \tag{4.3}$$

where G_{amp} is the amplitude estimated by the retracker solved for σ_0 in dB, G is the waveform scale factor computed and stored in the L1B product when constructing the waveforms and $\Delta\sigma_{0,dB}$ set to 3.04dB is a commonly-used constant to align CryoSat-2 to Envisat results. This is necessary to retrieve a wind speed estimation from σ_0 [Abdalla, 2012].

As different factors are estimated for RDSAR and SAR/LRMC (A for RDSAR and K for SAR/LRMC), we discriminate between the DDA and the CA implementation of SINC (see the notation below).

In the RDSAR model the amplitude A is defined as:

$$A = \frac{G_0^2 \sigma_0 {\lambda_c}^2 c}{4(4\pi)^2 \sqrt{\alpha_x \alpha_y} L_p {h_s}^3} \exp\left\{-\alpha_0 \frac{x_s^2 + y_s^2}{{h_s}^2} - \Delta\sigma_{0,\xi}\right\} \tag{4.4}$$

which can be solved for σ_0 and converted to dB. For the sake of readability, an auxiliary variable G_ξ is defined, which holds the attenuation caused by the mispointing and the mean square surface slope:

$$G_\xi = \frac{10}{\ln(10)} \left[\alpha_0 \frac{x_s^2 + y_s^2}{{h_s}^2} + \Delta\sigma_{0,\xi}\right] \tag{4.5}$$

G_{Amp}^{CA} can then be written as

$$G_{Amp}^{CA} = 10\log_{10}(A) + 10\log_{10}\left(\frac{4(4\pi)^2 \sqrt{\alpha_x \alpha_y} L_p {h_s}^3}{G_0^2 {\lambda_c}^2 c}\right) + G_\xi \tag{4.6}$$

whereby the two way propagation loss due to atmospheric effects L_p is computed using weather data from the global forecast system.

For the SAR/LRMC model, the calculation of G_{Amp}^{DDA} involving the estimated parameter K is defined as:

$$K = \sqrt{\frac{\alpha_x}{c h_s}} \frac{c h_s}{2\alpha_x f_c v_x} A \tag{4.7}$$

leading to

$$G_{Amp}^{DDA} = 10\log_{10}(K) + 10\log_{10}\left(\frac{(4\pi)^3 L_p {h_s}^4}{G_0^2 {\lambda_c}^2}\right) - 5\log_{10}\left(\frac{c h_s}{\alpha}\right) + G_\xi \tag{4.8}$$

Outlier detection is necessary to account for corrupted signals or for errors in the retracking procedure to receive a reliable estimation of the trueness, accuracy and precision. This study follows the definitions of the ISO 5725 series of standards, where trueness is defined as the mean difference of a data population with respect to an accepted reference, precision the closeness of a measured value with respect to the mean of the given data population and accuracy describes the closeness of a measured value to the true value (see ISO 5725-1 [1994]). To be consistent with the G-POD SARvatore product, the same criteria to the select the 20 Hz data and build the 1 Hz data from the 20 Hz data in the L2 processor are used. For 40 or 80 Hz, the procedure is the same. First, the selection of 20 Hz data and the building of the 1 Hz data as made in the L2 processor is described. For stack retracking, the same procedure applies. As this study focuses on the open ocean, only data points with a distance to coast longer than ten kilometres are considered. The distance to coast is calculated by linear interpolation of the 1x1 arc-minute closest distance to coast grid derived by the Global Self-consistent, Hierarchical, High-resolution Geography Database (GSHHG) (see Wessel and Smith [1996] for further information). The version of the grid used is v2.3.4.

1. Gather 20 consecutive 20 Hz values. Gaps have been filled with Not a Number (NaN).
2. Replace 20 Hz values with not a number (NaN) if their corresponding misfit r_i value is bigger than $1.8\tilde{r}$ with
   - $r_i = 100\sqrt{\frac{1}{208}\sum_{k=25}^{232}(\bar{y}_k - \bar{s}_k)^2}$ the misfit of the signal with index i within one file calculated from the residuals obtained in the estimation.
   - $\tilde{r}$ the median of all misfit values within one file excluding NaN values.
3. Calculate and store 1 Hz value by averaging all not NaN values of the set of 20 consecutive 20 Hz values.
4. Detrend the set of gathered 20 Hz values and calculate and store the standard deviation of the averaged 1 Hz value.

Second, the selection criteria of the above-computed 1 Hz data for cross validation with another product are described. These criteria are applied outside the L2 processor before the cross comparison and are parameter-dependent. They involve both the 1 Hz values and their standard deviation, whereby those not fulfilling the criteria below are excluded from further analysis:

- SLA:
  - $r_i < 10$ for RDSAR
  - $|SLA_{unc}| = |h_s - (R - \Delta R) - h_{mss}| < 15$ metre
  - $|SLA - \tilde{SLA}| < 3\sigma_{SLA}$ with median $\tilde{SLA}$ and standard deviation σ_{SLA} computed for the complete regional dataset
- SWH:
  - $r_i < 10$ for RDSAR
  - -1.5 m < H_s < 15 m
- σ_0:
  - $r_i < 10$ for RDSAR
  - $|\sigma_0 - \tilde{\sigma_0}| < 3\sigma_{\sigma_0}$ with median and standard deviation computed for the complete regional dataset

This chapter briefly discusses how sea surface sampling can affect the quality of retrieved geophysical parameters. First, in Figure 5.1 it is shown how surface sampling is performed within one tracking cycle. Of course, in SAR processing the location of the sea surface samples is arbitrary as all beams are steered automatically to any surface location in reach by the L1B SAR algorithm. However, this is not possible for RDSAR and LRMC, which are tied to the burst locations within a tracking cycle.

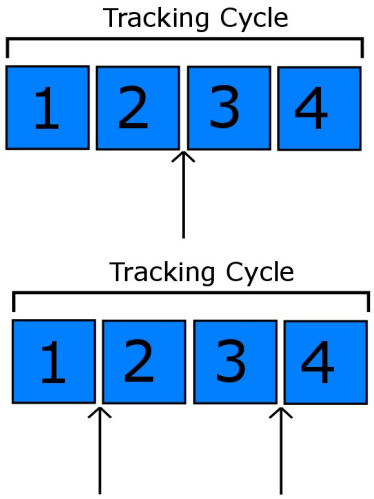

Figure 5.1: Sampling within a tracking cycle of CryoSat-2. The numbers in the squares give the index of the bursts where the arrows shows the position at which a surface sample is set. The upper half shows the 20 Hz case and the lower part the 40 Hz case.

The location of the sea surface sample depends on how many bursts are considered to retrieve a RDSAR waveform or a LRMC stack. The upper part of Figure 5.1 shows the 20 Hz case where all of the pulses or stacks of all four bursts in the current tracking cycle are averaged, leading the surface sample to be in the middle (see the black arrow). Otherwise, in the 40 Hz case (lower part of Figure 5.1) the pulses or stacks from burst number one and two are averaged given a surface sample between these two and additionally numbers three and four are averaged giving another surface location in between.

As the centres of each burst are geolocated, the 20 or 40 Hz surface locations can be calculated by a linear interpolation and a projection on a reference surface (in this study a torus). The epoch for each location is also calculated with a linear interpolation.

Of course, the choice of the sea surface sampling rate affects the Signal-to-Noise-Ratio (SNR) for RDSAR and LRMC L1B data as in the 40 Hz case fewer observations are used in the averaging. However, in SAR processing this does not apply as the number of beams in each surface location does not change, although it is possible that due to correlations the overall quality of the retrieved data does not change.

The theoretical background for optimal sampling is the Nyquist-Shannon sampling theorem [Papoulis, 1977, Section 5-1], stating that a band-limited signal with maximal frequency f_{max} needs to be sampled with a rate $\geq 2f_{max}$ to avoid aliasing. During the L1B processing this automatically applies due to the zero-padding before each FFT, although for the sea surface locations this is not necessarily the case due to different illumination patterns for each processing mode. Where RDSAR is pulse-limited, leading to an illuminated area defined by the antenna characteristic for LRMC and SAR, which are beam-limited, the footprint differs. Of course as no beam steering is performed in LRMC processing,

it is assumed that this mode behaves similar like RDSAR. However, in SAR processing the illuminated area is given by the along-track PTR of each beam coming from different burst locations, which gives a much smaller footprint compared with the other modes. For the CryoSat-2 beams, the maximal frequency of the along track PTR is given by

$$f_{max} = \frac{2\alpha_x f_c v_x}{ch_s} \frac{N_p}{PRF} \approx 0.0034 \frac{1}{m} \tag{5.1}$$

This means that the distance between each surface sample to avoid aliasing should be

$$\Delta x_{Nyquist} \leq \frac{1}{2f_{max}} \approx 146 \text{ m} \tag{5.2}$$

where the distance between two 20 Hz samples is

$$\Delta x_{20Hz} = \frac{v_x}{20Hz} \approx 336 \text{ m} \tag{5.3}$$

which means that the sea surface is under-sampled by approximately a factor of two for 20 Hz SAR waveforms or stacks. According to the results of Eq. 5.2 and Eq. 5.3 an optimal surface sampling rate would be 40 Hz to avoid aliasing. This will be investigated in the following real data experiment. 80 Hz surface sampling is not considered as frequencies greater than $2f_{max}$ do not introduce more information than $2f_{max}$ and therefore do not affect the SNR.

Figure 5.2 shows the region of interest for this study, namely the Pacific SAR mode box for CryoSat-2. The L1A data processed in this part include the whole year 2013 of this box.

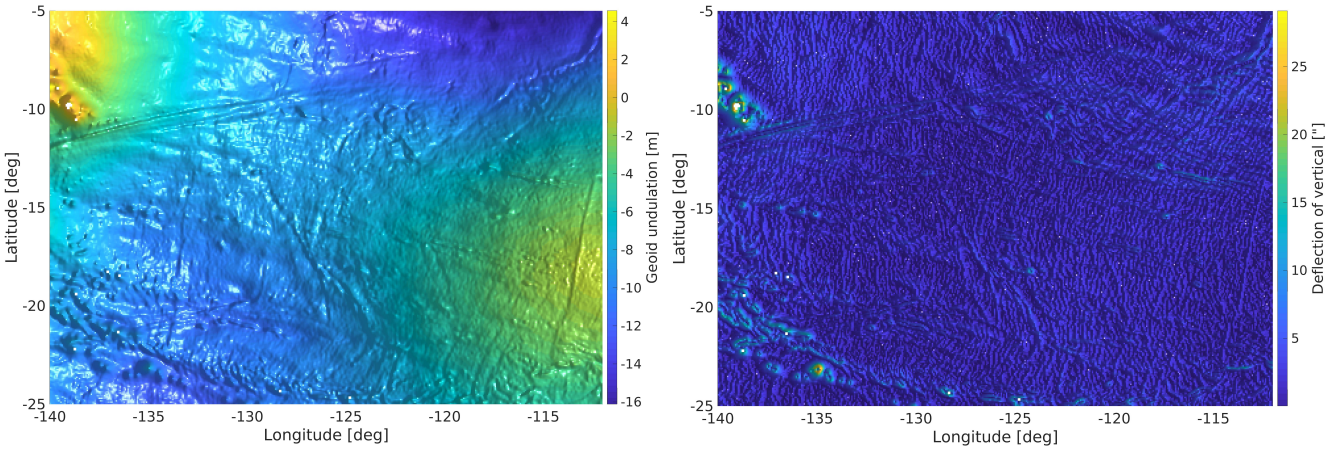

Figure 5.2: Geoid undulation (left side) and absolute deflection from vertical (right side) in the pacific box.

The Pacific box is appropriate for this part of the study as it allows calculating Power-Spectral-Density (PSD) diagrams with long tracks of 6800 20 Hz and 13600 40 Hz surface samples, as with the exception of a few islands in the west of this box (see white gaps in Figure 5.2) no land contamination is expected. Additionally, the geoid is flat (see Figure 5.2 left side) and the absolute deflections of vertical are small (see Figure 5.2 right side).

The considered retracker in this chapter are SINC2 for RDSAR and SINCS for SAR and LRMC. Both retrackers are described in Buchhaupt et al. [2018], although in this study the SINC derived in chapter 3 extended for geoid slopes and curvatures is used. The estimated parameter are therefore A, t_0 and σ_s.

First, the trueness between 1 Hz geophysical parameter from SAR 20 Hz and the other processing modes with different surface sampling rates are investigated to ascertain whether there are biases between them. This is achieved by calculating the differences of 1 Hz data depending on the SWH value retrieved from SAR 20 Hz shown in Figure 5.3. As in the Pacific box in the year 2013 SWH values mainly vary between one and five metres only, this interval is considered. In Figure 5.3, the 1 Hz SWH values from SAR 20 Hz are divided in classes from one to five metres with a step size of one decimetre. Within each class, all differences between the reference product and the others are gathered separately and the mean value is calculated. The mean differences for σ_0 are shown for the sake of completeness as the differences are insignificantly small.

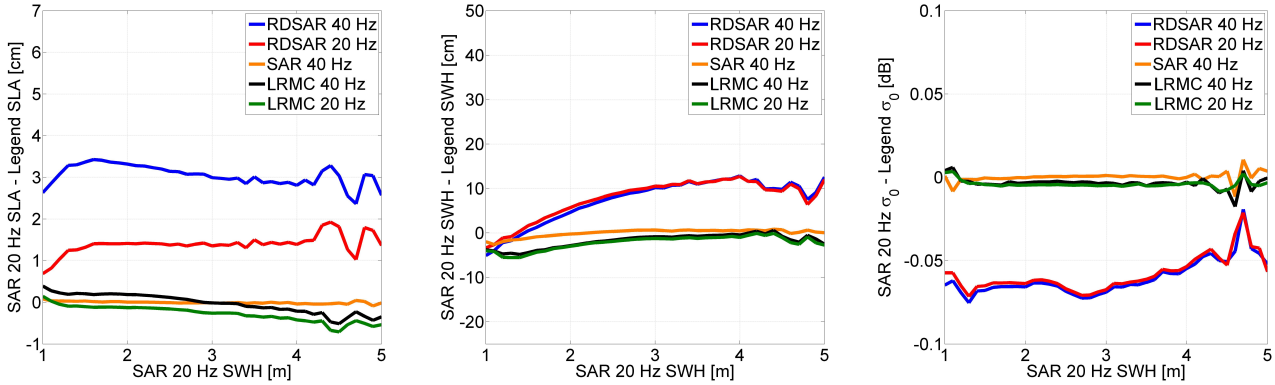

Figure 5.3: Relative trueness between different processing modes with different sea surface sampling rates. In all three figures, the reference is 1 Hz data, derived by 20 Hz SAR processing. The figures shows the relative accuracy for SLA, SWH and σ_0 (from left to right).

It is observable in Figure 5.3 left that RDSAR 20 (blue curve) and 40 Hz (red curve) have a bias with respect to SAR 20 Hz where the mean differences are higher in RDSAR 40 Hz. This can be explained by the retracker bias, which occurs as the RDSAR waveform samples ar not sufficiently close to a normal distribution to retrieve bias-free parameters. This effect is increased in RDSAR 40 Hz as only pulses calculated from two bursts are averaged instead of four in RDSAR 20 Hz. However, this effect is only observable for Sea Level Anomaly (SLA). The SWH (Figure 5.3 middle) and σ_0 (Figure 5.3 right) values show no significant differences between RDSAR 20 and 40 Hz. However, in Figure 5.3 middle a clear sea state dependency between the SWH differences varying from -5 to 12 cm is observable between SAR 20 Hz and RDSAR. This will be discussed in chapter 7.

For LRMC (black and dark green curves), the mean differences with SAR 20 Hz are below one centimetre for SLA and below 5 cm for SWH. However, for both parameters a slight sea state dependency for both SLA and SWH is observable, which needs to be investigated as these cannot be explained. It is observable that LRMC 40 Hz has a slightly different bias than LRMC 20 Hz, which can be explained in the same way as for RDSAR by the retracker bias.

With the orange curve in Figure 5.3, it can be shown that SAR 20 and 40 Hz are approximately identical in terms of mean differences. Only for SWH smaller than two metres is a SWH difference less than two centimetres observable.

In order to investigate the impact of sea surface sampling on the precision of the geophysical parameter retrieved, it is not sufficient to compare empiric standard deviations of 1 Hz data as this does not consider correlations between the 20 or 40 Hz values. To overcome this issue, the absolute difference of consecutive 1 Hz data samples are calculated and compared for each processing mode and sampling rate. The benefit of this approach is that the absolute difference of two consecutive values is proportional to the real 1 Hz standard deviation considering implicitly correlations. This means that the higher the standard deviation, the greater the absolute difference and vice versa. Of course, slopes that occur also affect these measures, although if the difference between two data products is calculated the slopes vanish as they are the same for all considered datasets.

Figure 5.4 shows the difference of absolute along-track differences for several products where the reference is always SAR 20 Hz as this sampling rate is assumed to be under-sampling the sea surface in SAR mode. The statistical parameter considered in Figure 5.2 are the mean and the skewness. A positive mean value means that the absolute differences are on average lower than for the reference dataset, which means that these product is more precise. If the skewness is greater than zero, more data is positive, given that absolute differences are more often lower than the reference. The results for σ_0 are shown for the sake of completeness as the differences are sufficiently small to neglect.

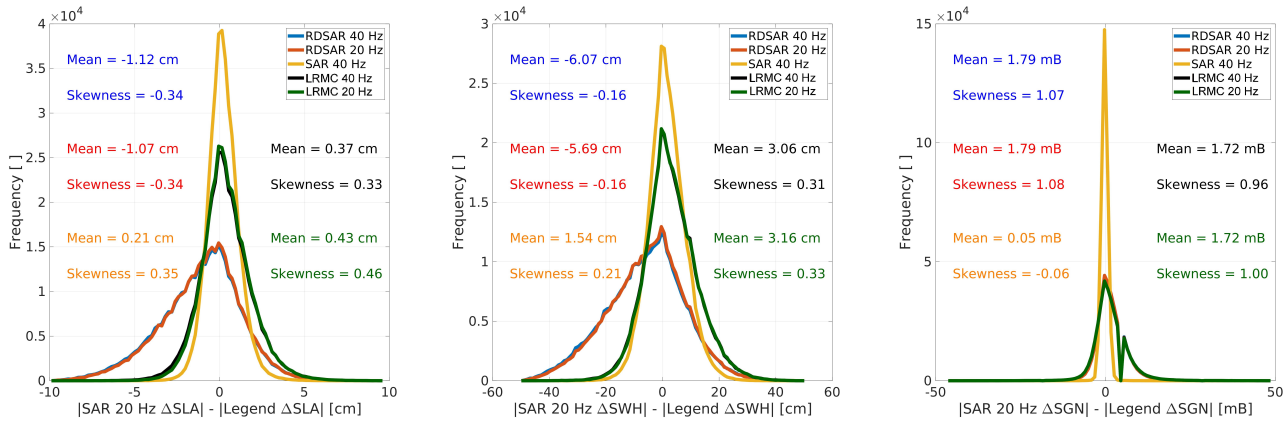

Figure 5.4: Difference between 1 Hz absolute along-track differences for different processing modes with different surface sampling rates. In all three figures, the reference is the absolute along-track differences of 1 Hz data derived by 20 Hz SAR processing. The figures shows the relative differences for SLA, SWH and σ_0 (from left to right).

Figure 5.4 shows that RDSAR has a lower precision than SAR 20 Hz, as the mean values and the skewness are negative. It is observable that RDSAR 40 Hz (blue curve) is slightly less precise than RDSAR 20 Hz (red curve) for SLA and SWH. The opposite applies for LRMC that have positive mean and skewness values, which means that they are more precise or that signals with high frequencies are filtered out due to the larger footprint leading to a lower standard deviation. As for RDSAR, the 40 Hz LRMC values (black curve) are slightly less precise than the 20 Hz product (dark green curve) for both parameter which can be explained by the lower SNR of the processed waveforms as two stacks are averaged in the 40 Hz case compared with four in 20 Hz. The most interesting result is shown by the orange curve in Figure 5.4 showing the differences between SAR 20 and 40 Hz. It is observable due to the positive mean and skewness values that for both SLA and SWH the 40 Hz product is superior in precision compared with the 20 Hz data.

Next, the PSD is investigated to evaluate the capability of each processing mode to detect signals with high frequencies. This is achieved by performing following two steps:

1. Calculate for each track and parameter (SLA, SWH and σ^0) separately a PSD if the track fulfils following conditions:
   - No gaps and outliers are present.
   - The track has at least 6800 20 Hz or 13600 40 Hz consecutive samples.

   The PSD is calculated with FFTs of lengths 6800 in the 20 Hz case and 13600 in the 40 Hz case by

$$PSD = \frac{\Delta_t v_x}{N_{FFT}} |FFT(\mathbf{x})|^{②} \tag{5.4}$$

   where Δt is the average time interval between two consecutive sea surface samples, N_{FFT} the length of the FFT's and $\mathbf{x}$ a vector containing the estimated values for one variable and track. The prefactor serves as a normalization to retrieve cycles per kilometre (cpkm) as a unit.

2. Average for each parameter separately all PSDs to increase the SNR. The spectra are shown in Figure 5.5.

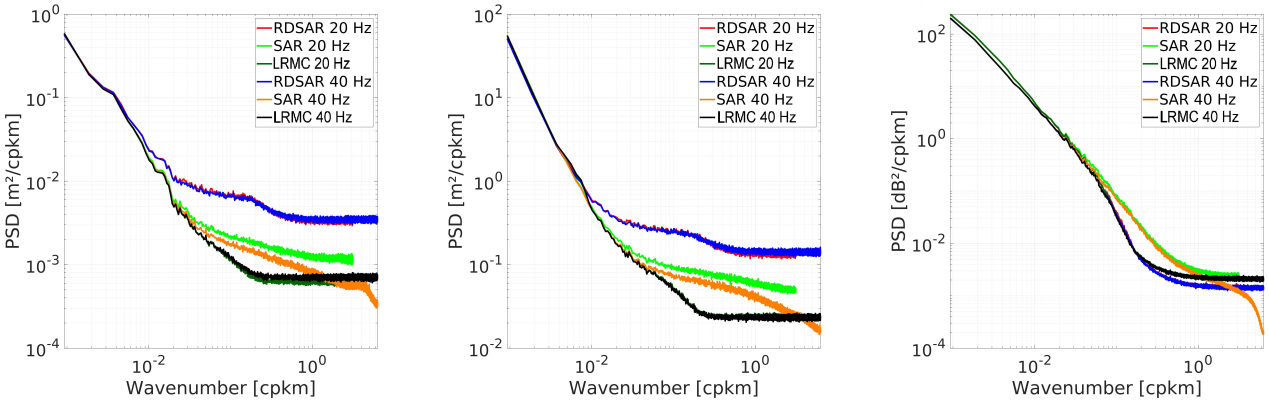

Figure 5.5: Averaged PSDs for different processing and sampling rates for SLA, SWH and σ_0 (from left to right).

The left plot in Figure 5.5 shows the averaged PSDs of retrieved SLA values. For RDSAR, both the 20 (red curve) and 40 Hz (blue curve) spectras overlap, whereby the 40 Hz version has a slightly higher noise floor of about 5 cm. In both cases, a bump is observable at 0.2 cpkm, which can be related to the footprint with circa five kilometre radius. In the RDSAR 40 Hz spectra, no additional information in the higher frequencies is observable. For LRMC (black and dark green curves), no spectral bump is present and the noise floor is circa 2.6 cm high, whereas in the 40 Hz case the noise is slightly larger and no additional information is achievable in high frequencies. For SAR mode data (light green and orange curves), pink noise - which is characterized by a linear frequency-dependent power decrease - is observable in medium to high frequencies. A possible explanation for this phenomena is the correlation between the surface locations as they contain beams coming from an equal subset of bursts. However, it is observable that 40 Hz SAR data introduces more information in high frequencies, which is observable due to smaller powers in these bands, although the overall precision of LRMC is superior.

In the middle plot of Figure 5.5, the SWH spectra show exactly the same behaviour, albeit with different quantities. The noise floor of LRMC is about 16 cm, whereas for RDSAR it is circa 38 cm. Due to pink noise, an estimation of the precision cannot be generated from Figure 5.5.

For σ_0 (right plot in Figure 5.5), the main difference is that the noise floor of RDSAR (0.04 dB) is lower than for LRMC (0.05 dB). Moreover, for this parameter SAR 40 Hz is capable of observing signals at higher frequencies.

6.1 Region of Interest and Overview

The scope of this chapter is to investigate the impact of sea surface curvatures and slopes on RDSAR, LRMC and SAR processing from L1A to L2. This is performed by using CryoSat-2 SAR mode data in the area of the Marianna trench shown in Figure 6.1. In this study, data in the year 2016 is considered.

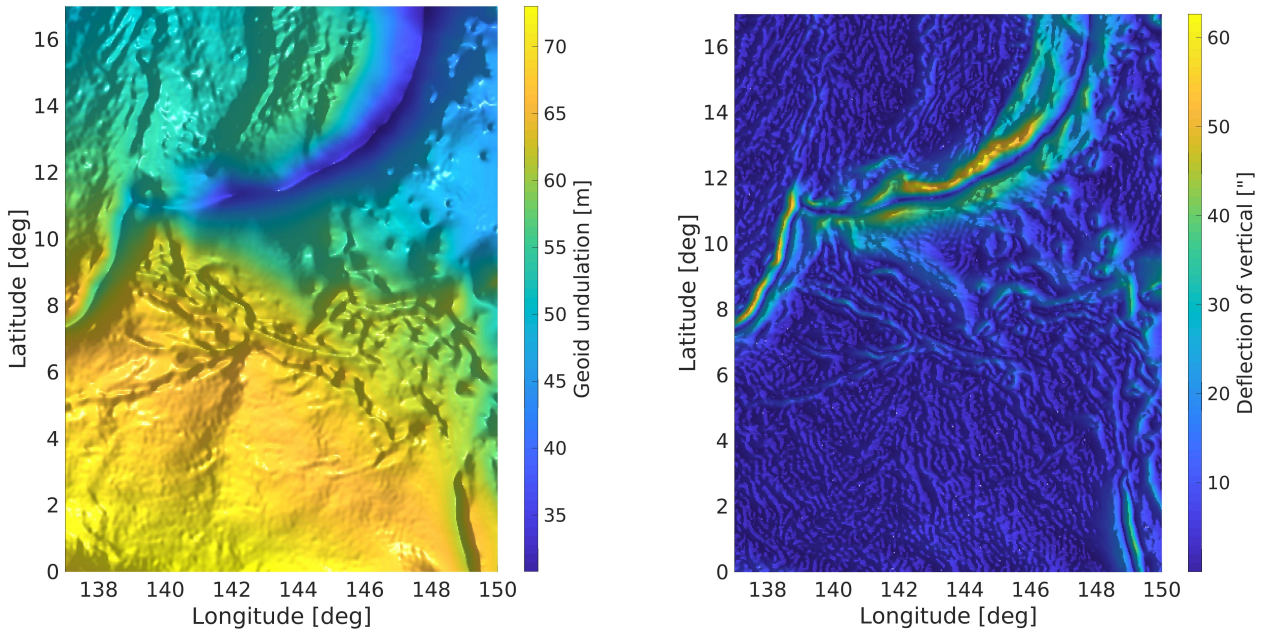

Figure 6.1: Geoid undulation (left) and absolute deflection from vertical (right) in the SAR box Marianna trench.

As shown in Figure 6.1, the chosen SAR mode box offers a high variety of absolute vertical deflections from zero to sixty arc seconds. It is beneficial that areas exist with high deflections being the Marianna trench and low ones. This is discussed in section 6.4. The impact of surface slopes and curvatures can be divided into three partitions:

1. Impact on the L1B processing: This only affects LRMC and SAR processing as in these modes geometrical corrections are performed depending on the location of the beams on the sea surface such as the RMC.

2. Impact on the model used in L2 processing: As shown in Eq. 3.51 and 3.52 the surface slopes cause a roll and pitch bias, whereas the curvatures introduce different sea surface curvature coefficients.

3. An error introduced in Sandwell and Smith [2014] - caused by the retrieved range from retracking L1B data - corresponds to the closest sea surface location, which differs from the closest point between the platform and the reference ellipsoid if slopes and curvatures are present. This effect is not considered here, although given that SAR is not affected by along-track slopes due to the steering to dedicated surface locations a range shift of $\frac{\alpha_x x_s^2}{2h_s}$ is applied to keep this mode consistent with the other two.

To separate impact factor one and two the comparison is divided into two sections. In the first section 6.2, all LRMC and SAR mode data with different surface representations are compared against the corresponding RDSAR product. This shall isolate the impact on L1B processing as it can be assumed that the effect on the retracking is similar for all three modes. Given that only the along-track slope and curvature coefficients can affect the L1B processing, only x_s and α_x are considered in this chapter.

In section 6.3, results with different surface representations but same processing modes are compared. Accordingly, it is possible to investigate the impact on the L2 processing for the curvature and slopes separately.

Section 6.4 briefly discusses how the investigation results can be used in MSS or geoid determination.

6.2 Cross Comparison of the Different Processing Modes with Different Sea Surface Representations

Before the results are discussed, first it is described how the following figures are calculated. All figures show two-dimensional normalized histograms where the x-axis is divided in 50 and the y-axis in 64 classes. The range of the classes can be directly read off the axis limits. Within each class, the number of occurring members is counted and stored in the corresponding sample. For the sake of clarity, the counts of the y-axis are normalized, whereby that for each x-axis class the maxima is one.

For a better evaluation, a best-fitting polynomial is calculated and plotted for each histogram (see thick blue curves), whereby the coefficients a_i are shown in each plot. The polynomials $y(x)$ are then defined by

$$y(x) = \sum_{i=0}^{i_m} a_i x^i \tag{6.1}$$

with i_m the maximal index shown in each plot. x corresponds to the quantity described by the x-axis. The polynomials are estimated by using a Levenberg-Marquardt least squares optimizer.

This section is subdivided into the comparison between RDSAR and LRMC and between RDSAR and SAR, each of which have three subsections for each surface representation (sphere, slopes and geoid). The parameters of interest are Sea Surface Height (SSH) and SWH. For SSH, a polynomial of order three is used and a second order polynomial is fitted to the SWH. σ_0 will not be discussed as the mean differences are below 0.2 dB and therefore very small. However, for the sake of completeness they are shown.

6.2.1 Comparison of RDSAR and LRMC

Sphere

Figure 6.2 shows a high dependency on the SSH differences (left) varying from -20 to +20 cm, where the best-fitting polynomial is cubic. For SWH (middle), a quadratic dependency is observable, meaning that the sign of x_s does not affect the differences which vary from 7 to 200 cm. Overall, LRMC L1B processing is affected by slopes due to the blind range cell migration corrected, which is not performed in RDSAR processing.

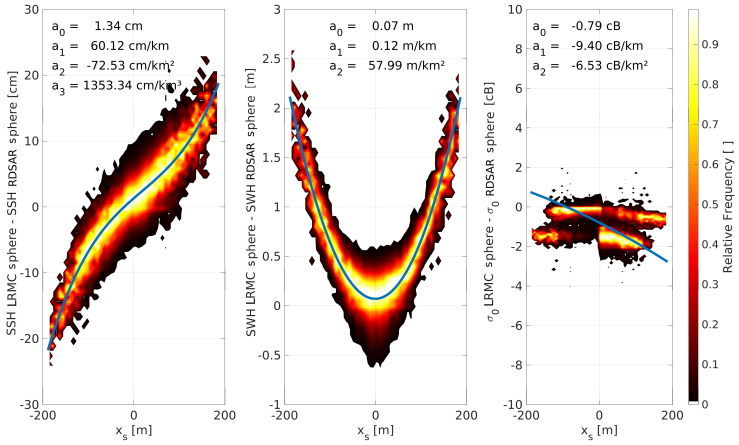

Figure 6.2: Two-dimensional normalized histograms of the differences between LRMC sphere and RDSAR sphere products with respect to the along-track coordinate x_s of the platform on a torus best fitting the geoid. The figures show the differences for SSH, SWH and σ_0 (from left to right).

For the curvatures this does not apply given that - as shown in Figure 6.3 only the SSH (left) - shows a significant dependency on this measure where the best-fitting polynomial has an order of one with slope of -5.5 cm and offset of 1.7 cm. The higher order coefficients are small. For SWH (middle) no significant dependency is observable, whereby only a bias of 10 cm is present.

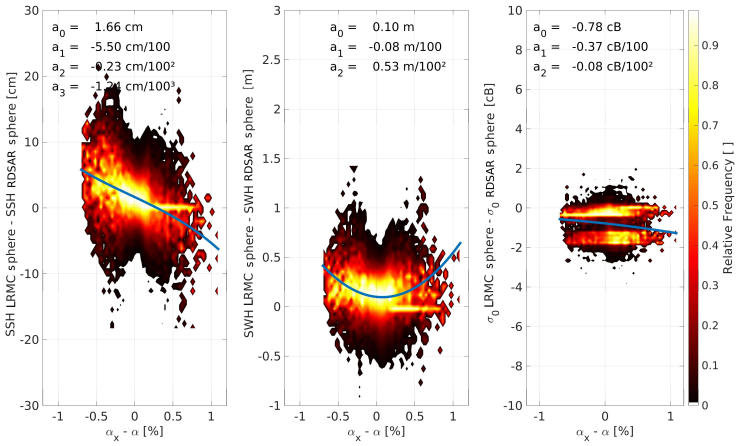

Figure 6.3: Two-dimensional normalized histograms of the differences between LRMC sphere and RDSAR sphere products with respect to the relative difference between the along-track curvature coefficient α_x of a torus best fitting the geoid and the spherical curvature coefficient α. The figures show the differences for SSH, SWH and σ_0 (from left to right).

Figure 6.4 shows that if geoid slopes are applied in the L1B and L2 processing, no significant dependencies of the differences between RDSAR and LRMC are observable. The magnitude of the polynomial coefficients can be explained by over-fitting. However, a SSH bias of 1.3 cm and a SWH bias of 7 cm remains.

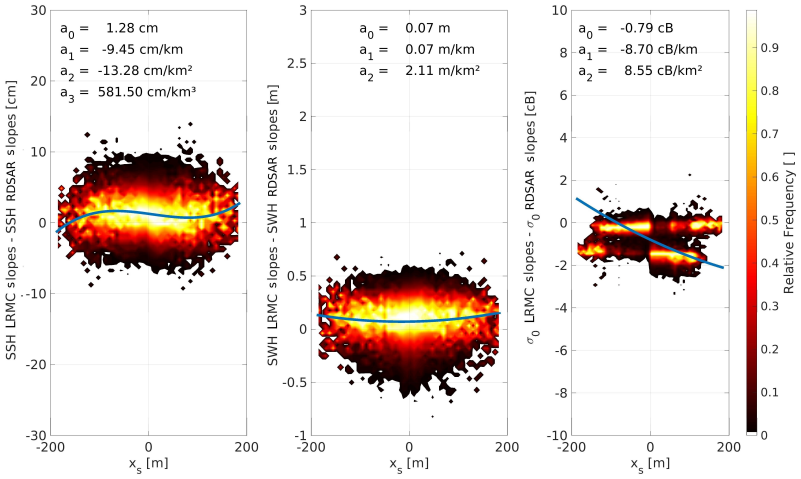

Figure 6.4: Two-dimensional normalized histograms of the differences between LRMC slopes and RDSAR slopes products with respect to the along-track coordinate x_s of the platform on a torus best fitting the geoid. The figures show the differences for SSH, SWH and σ_0 (from left to right).

However, it can be observed that a curvature dependency on the SSH differences remains present in Figure 6.5, with a slope of minus six centimetre per percent. This leads to the conclusion that LRMC SSH estimations are effected by geoid curvatures and slopes where the SWH only shows a slope dependency.

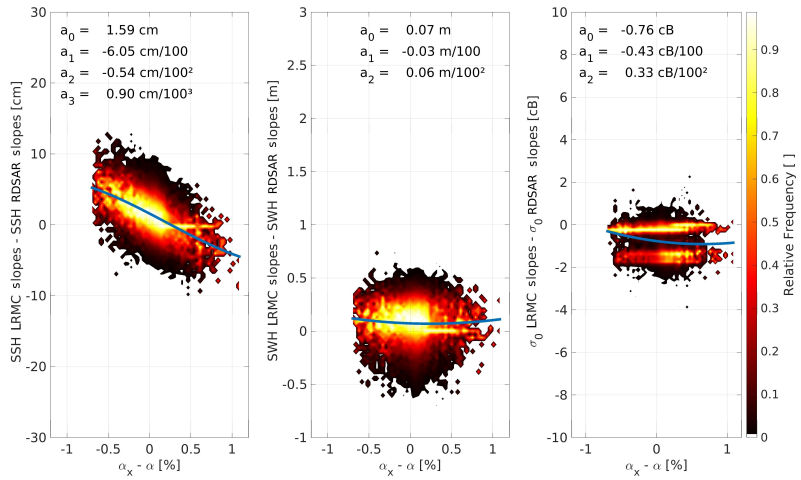

Figure 6.5: Two-dimensional normalized histograms of the differences between LRMC slopes and RDSAR slopes products with respect to the relative difference between the along-track curvature coefficient α_x of a torus best fitting the geoid and the spherical curvature coefficient α. The figures show the differences for SSH, SWH and σ_0 (from left to right).

In order to ensure that the processing including the geoid was performed correctly, the differences of the retrieved parameters from products including the geoid are compared. Figures 6.6 and 6.7 show that no significant differences remain, which means that LRMC processing leads to consistent results with RDSAR. However, a SSH bias of 1.5 cm and a SWH bias of 7 cm remain.

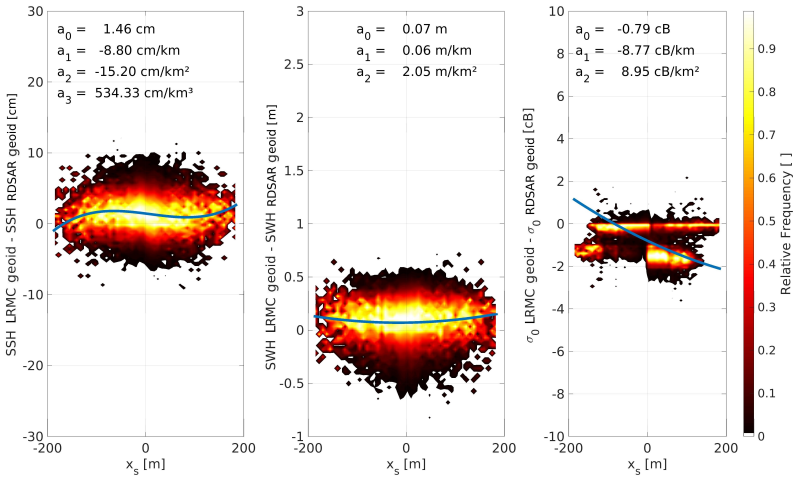

Figure 6.6: Two-dimensional normalized histograms of the differences between LRMC geoid and RDSAR geoid products with respect to the along-track coordinate x_s of the platform on a torus best fitting the geoid. The figures show the differences for SSH, SWH and σ_0 (from left to right).

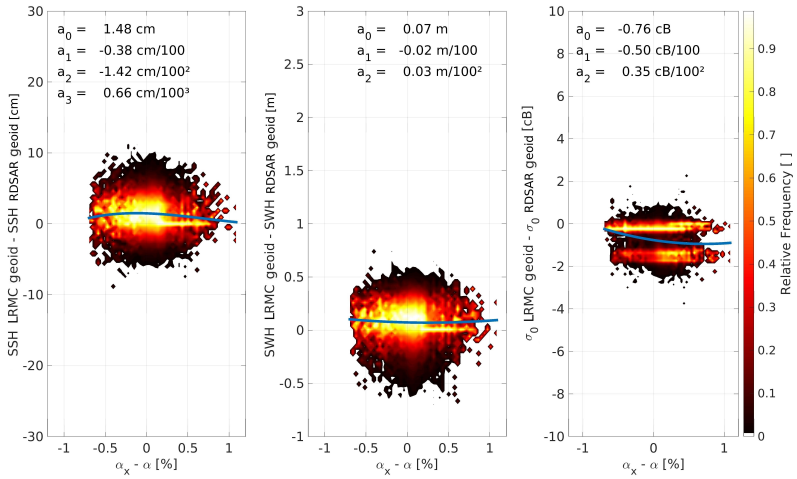

Figure 6.7: Two-dimensional normalized histograms of the differences between LRMC geoid and RDSAR geoid products with respect to the relative difference between the along-track curvature coefficient α_x of a torus best fitting the geoid and the spherical curvature coefficient α. The figures show the differences for SSH, SWH and σ_0 (from left to right).

6.2.2 Comparison of RDSAR and SAR

Sphere

Figure 6.8 shows a slight dependency on the SSH differences (left) where the best-fitting polynomial is quadratic. For SWH (middle), no dependency is observable. Overall, SAR L1B processing is not affected by slopes as the quadratic polynomial is caused by an error in RDSAR, which does not account for the fact that the closest point is not located at the reference coordinated on the ellipsoid.

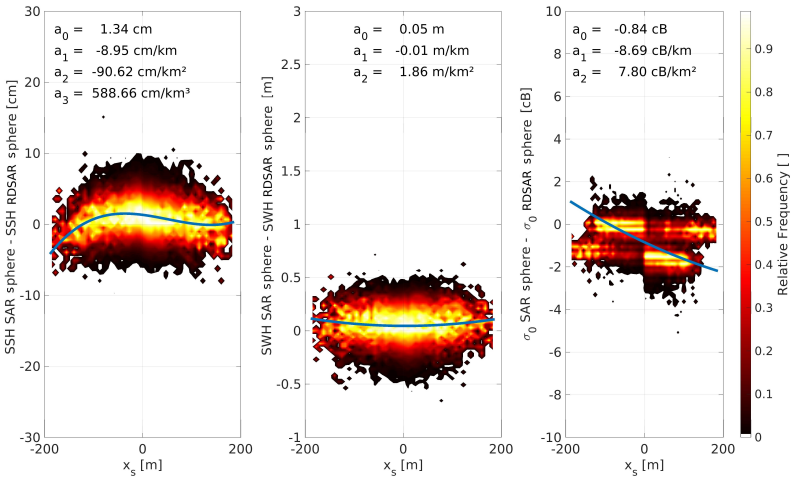

Figure 6.8: Two-dimensional normalized histograms of the differences between SAR sphere and RDSAR sphere products with respect to the along-track coordinate x_s of the platform on a torus best fitting the geoid. The figures show the differences for SSH, SWH and σ_0 (from left to right).

For the curvatures this does not apply given that - as shown in Figure 6.9 - no significant dependency exists, whereby only a SWH bias of five centimetre and a SSH of 1.3 cm are present.

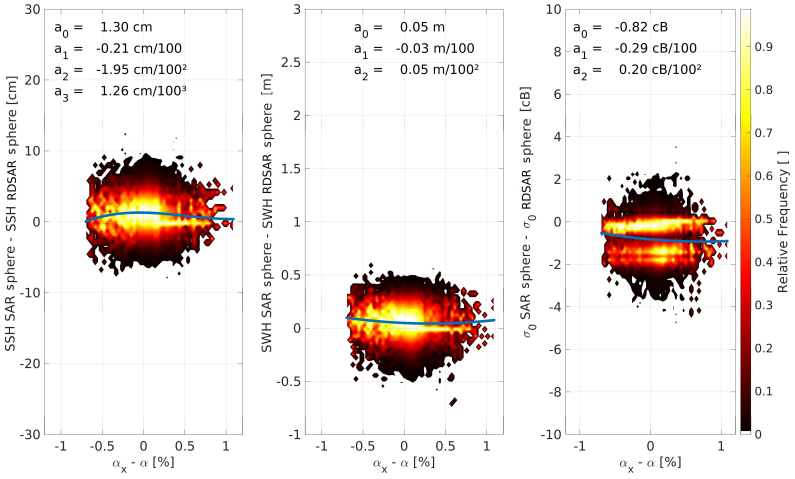

Figure 6.9: Two-dimensional normalized histograms of the differences between SAR sphere and RDSAR sphere products with respect to the relative difference between the along-track curvature coefficient α_x of a torus best fitting the geoid and the spherical curvature coefficient α. The figures show the differences for SSH, SWH and σ_0 (from left to right).

Figure 6.10 shows that if geoid slopes are applied in the L1B and L2 processing, no significant dependencies of the differences between RDSAR and SAR are observable. The magnitude of the polynomial coefficients can be explained by over-fitting. However, a SSH bias of 1.3 cm and a SWH bias of 5 cm remains.

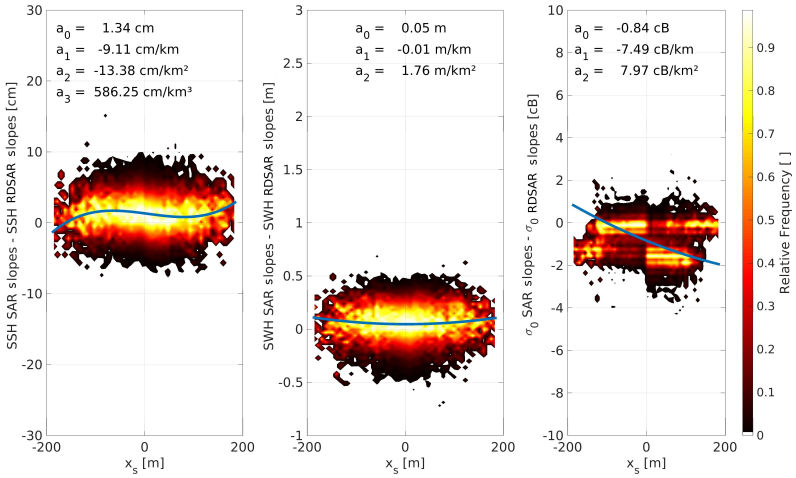

Figure 6.10: Two-dimensional normalized histograms of the differences between SAR slopes and RDSAR slopes products with respect to the along-track coordinate x_s of the platform on a torus best fitting the geoid. The figures show the differences for SSH, SWH and σ_0 (from left to right).

Even for curvatures no related differences exist in Figure 6.11. This leads to the conclusion that SAR SSH and SWH estimations are not significantly affected by along-track curvatures.

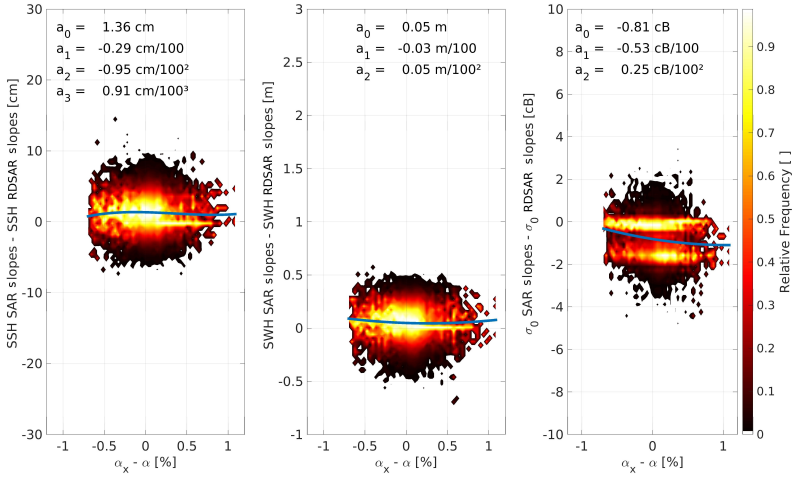

Figure 6.11: Two-dimensional normalized histograms of the differences between SAR slopes and RDSAR slopes products with respect to the relative difference between the along-track curvature coefficient α_x of a torus best fitting the geoid and the spherical curvature coefficient α. The figures show the differences for SSH, SWH and σ_0 (from left to right).

For the sake of completeness, Figure 6.12 and 6.13 show that no significant differences remain, which means that SAR processing leads to consistent results with RDSAR. However, a SSH bias of 1.3 cm and a SWH bias of 5 cm remain.

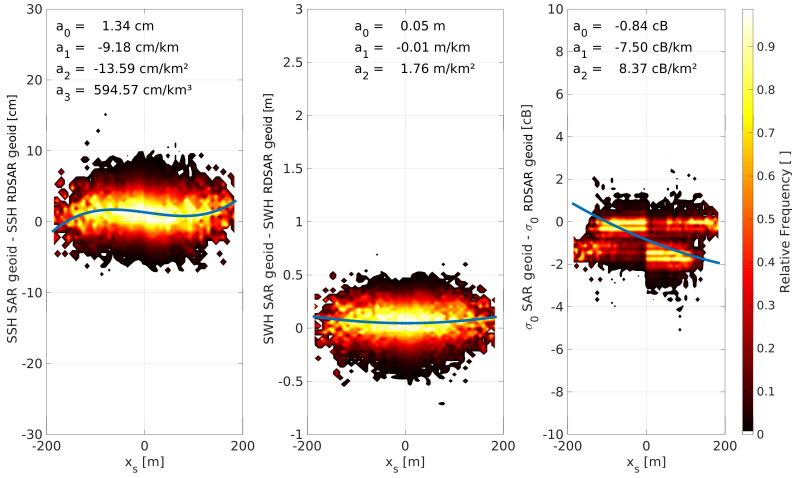

Figure 6.12: Two-dimensional normalized histograms of the differences between SAR geoid and RDSAR geoid products with respect to the along-track coordinate x_s of the platform on a torus best fitting the geoid. The figures show the differences for SSH, SWH and σ_0 (from left to right).

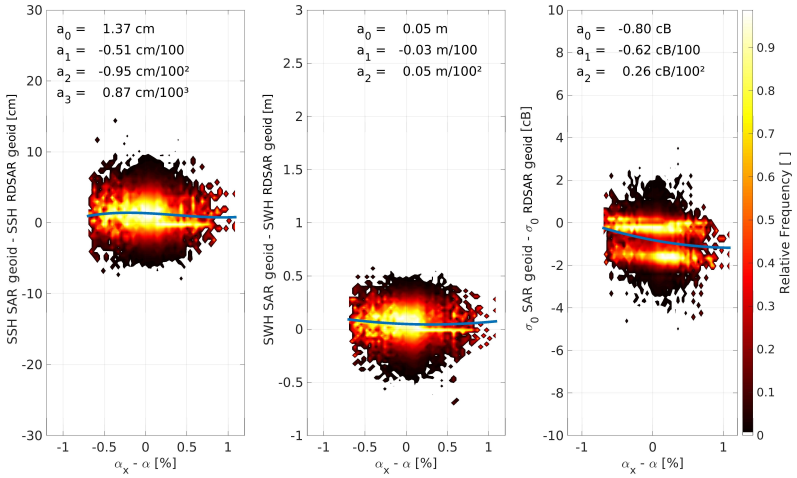

Figure 6.13: Two-dimensional normalized histograms of the differences between SAR geoid and RDSAR geoid products with respect to the relative difference between the along-track curvature coefficient α_x of a torus best fitting the geoid and the spherical curvature coefficient α. The figures show the differences for SSH, SWH and σ_0 (from left to right).

6.3 Cross Comparison with Different Surface Representations and Same Processing Mode

In the previous section LRMC and SAR products with different surface representations were compared against RDSAR, which made it possible to find impacts on the L1B processing. However, due to the low SNR of RDSAR only signals with a high amplitude were detectable. Therefore, small effects such as the introduced roll and pitch biases caused by slopes were blurred by noise. In order to detect these, a comparison with same processing modes but different surface representation is performed for RDSAR and SAR. Due to the smaller scales of these, the y-axis limits were reduced to observe these effects. LRMC is not considered as these effects on the L2 processing are small compared with the L1B impacts and therefore would not be observable.

6.3.1 Comparison for RDSAR

Figure 6.14 shows the differences between the RDSAR products with a spherical surface representation and a version including surface slopes. The SNR is much lower than in the previous section, given that both RDSAR products have highly correlated noise as they observe the same surface locations. This makes it possible to observe small slope dependencies that were masked out by noise in the previous section.

For SSH, a linear trend is observable with a slope of 1.85 cm per km, resulting in differences varying from -4 to +4 mm. In the case of SWH differences, a linear trend can also be observed, with a slope of 9 cm per km leading to mean differences from -2 to 2 cm in the area of the Marianna trench. Overall, it can be concluded that for high sea surface slopes the resulting roll and pitch biases can have a significant impact on estimated SSH and SWH values.

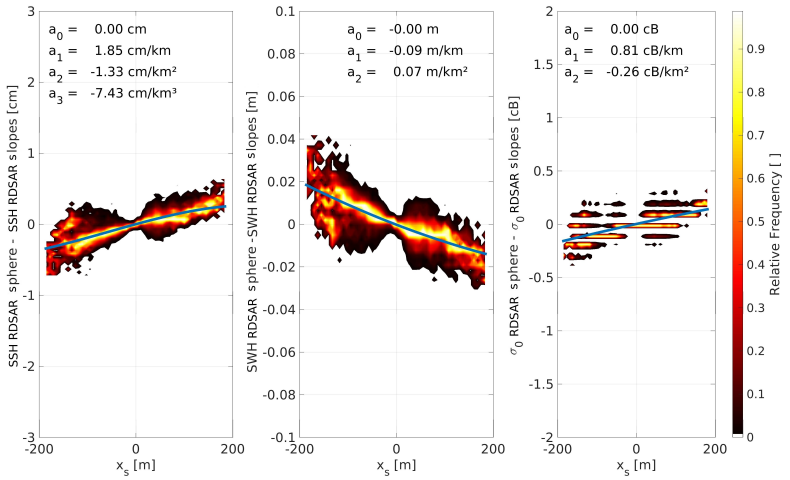

Figure 6.14: Two-dimensional normalized histograms of the differences between RDSAR sphere and RDSAR slopes products with respect to the along-track coordinate x_s of the platform on a torus best fitting the geoid. The figures show the differences for SSH, SWH and σ_0 (from left to right).

Figure 6.15 shows the differences between the RDSAR products with a version including surface slopes and a product including both curvature and slopes of the geoid. Compared with the differences shown in Figure 6.14, the trends are small leading to differences varying from -2 to 2 mm for SSH and -1 to 1 cm for SWH. Therefore, even for high curvatures the differences are negligible.

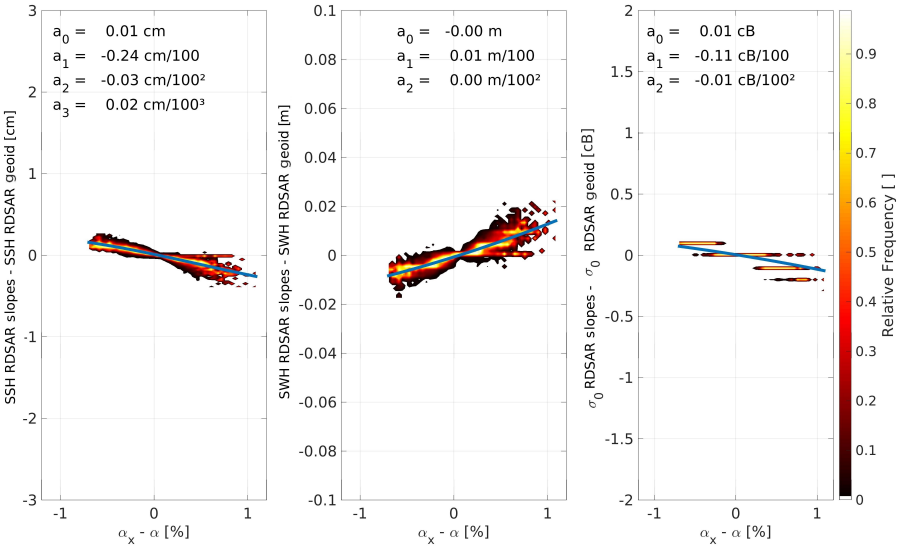

Figure 6.15: Two-dimensional normalized histograms of the differences between RDSAR geoid and RDSAR slopes products with respect to the relative difference between the along-track curvature coefficient α_x of a torus best fitting the geoid and the spherical curvature coefficient α. The figures show the differences for SSH, SWH and σ_0 (from left to right).

6.3.2 Comparison for SAR

Figure 6.16 shows the differences between the SAR products with a spherical surface representation and a version including surface slopes. With the exception of the quadratic x_s dependency of SSH - which has already been explained in section 6.1 - the results are similar to Figure 6.14, with equal linear trends. Therefore, it can be stated that the L2 processing of RDSAR and SAR are affected similarly by surface slopes.

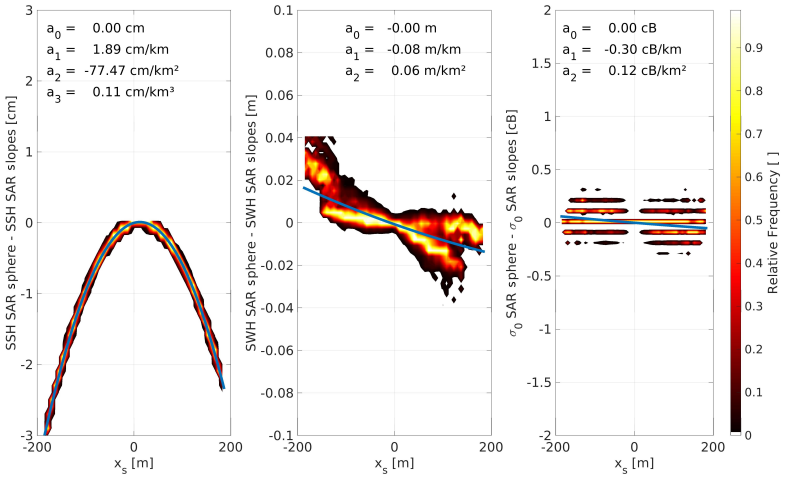

Figure 6.16: Two-dimensional normalized histograms of the differences between SAR sphere and SAR slopes products with respect to the along,track coordinate x_s of the platform on a torus best fitting the geoid. The figures show the differences for SSH, SWH and σ_0 (from left to right).

Figure 6.17 shows the differences between the SAR products with a version including surface slopes and a product including both curvature and slopes of the geoid. Compared with the differences shown in Figure 6.16, the trends are small leading to no differences for SSH and -2 to 2 cm for SWH. This means that only SWH is affected by sea surface curvatures. The slope of 2 cm per percentage is twice as high as for RDSAR, as shown in Figure 6.15.

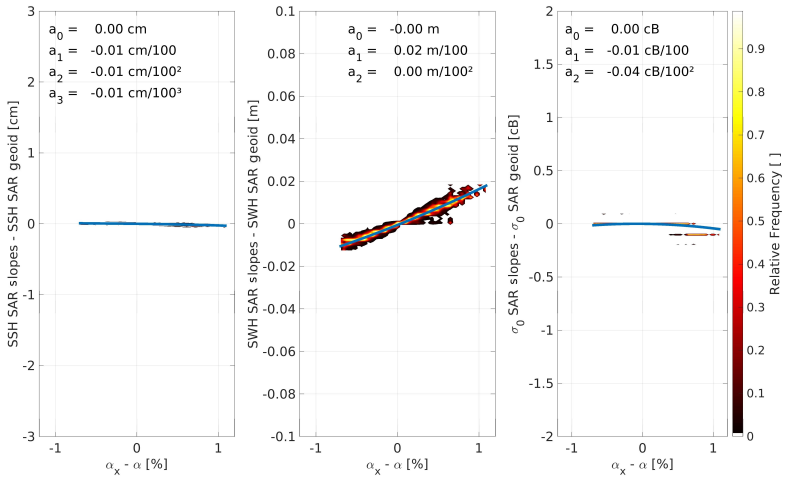

Figure 6.17: Two-dimensional normalized histograms of the differences between SAR geoid and SAR slopes products with respect to the relative difference between the along-track curvature coefficient α_x of a torus best fitting the geoid and the spherical curvature coefficient α. The figures show the differences for SSH, SWH and σ_0 (from left to right).

6.4 Possible Application

In the previous two sections, it was shown that along-track geoid curvatures and slopes significantly affects LRMC L1B processing, which is due to the blind RMC very sensitive to these quantities. On the other hand, RDSAR and SAR are robust against these influences as only the L2 processing results show significant differences at high slopes and curvatures. However, if the sea surface is correctly introduced in the L1B and L2 processing, the results of all three considered modes are consistent with each other, which is beneficial as LRMC will be the standard processing mode for Jason-CS (also called Sentinel-6) at the open ocean. Of course, the aim of using a processing mode is to retrieve correct geophysical parameters, although there are applications that might benefit from errors in LRMC caused by the sea surface, which will be briefly discussed in this section.

The idea is to use differences between LRMC and SAR SSH and SWH data to determine surface slopes and curvatures, which can be used to improve the MSS or the geoid. The benefit of this method is that the SSH differences would not be affected by atmosphere and sea state bias, as it is safe to assume that these quantities have the same impact on both modes. The same applies for SWH estimates, as these are probably also affected by wave steepness due to the intensity factor $I(z)$ and the variance of $p_{\eta_x,\eta_y|\eta}$ introduced in section 2.3.3. This leads to the assumption that the only remaining impact that differs between the two modes is the condition of the sea surface. As a result, it can be stated that the SSH differences between LRMC and SAR are a more robust measure compared with using the SSH for each mode separately. The SWH is used to distinguish between slopes and curvatures as SSH is affected by both.

The following Figures 6.18 to 6.20 shows how clearly the impact of the slopes and curvatures can be observed. For the sake of clarity, the tracks were gridded by a Delaunay triangulation performed with Matlab's *delaunay* function (see Su and Drysdale [1997] for further information about the algorithm). Figure 6.18 serves as a reference to see connections between the differences and occurring slopes and curvatures. As the sign of x_s depends on whether the platform is in ascending or descending mode, the absolute value is plotted here.

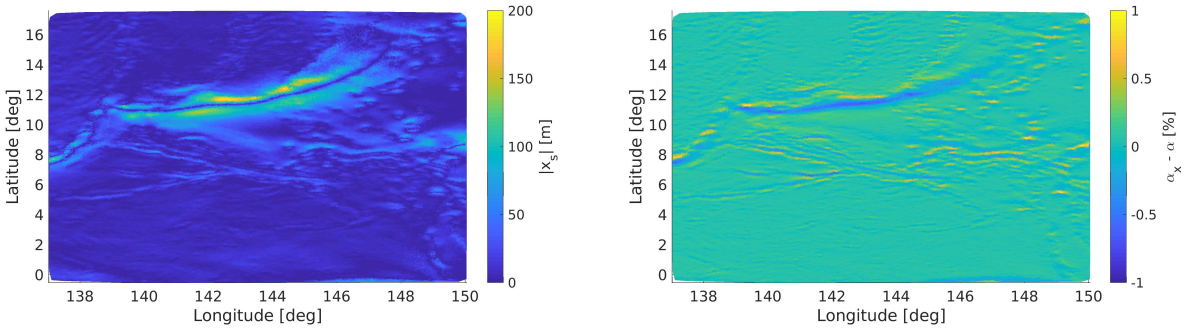

Figure 6.18: Slopes and curvatures in the area of the Marianna tench. The left plot shows the absolute along-track position of the platform in torus coordinates best fitting the geoid. On the right side, the relative difference between the spherical curvature coefficient α and the along-track coefficient α_x belonging to the geoid.

Figure 6.19 show the absolute differences for SWH (left plot) and SSH (right plot). It can be observed that the SWH differences clearly show the high surface slopes where the small ones are not that visible. This can be explained by the quadratic dependency, which reduces the impact for small slopes and increases it for high ones. In the case of SSH absolute differences even the smaller slopes are clearly observable due to the mainly linear dependency. Curvature dependencies are not clearly observable as these are smaller.

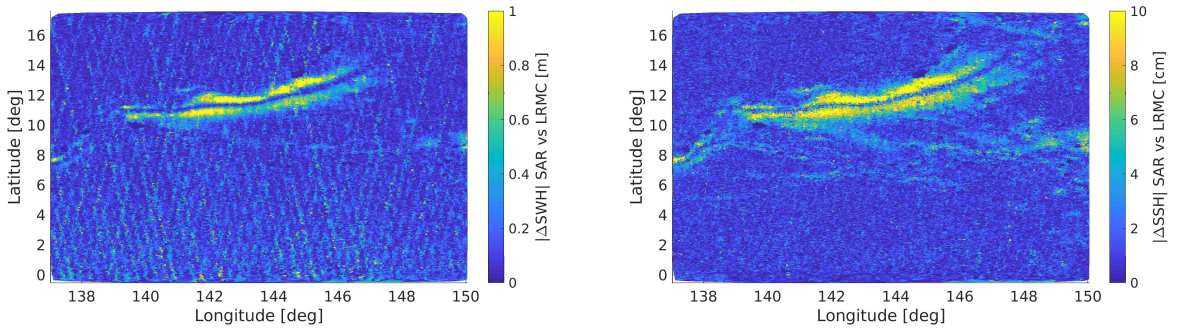

Figure 6.19: Absolute relative differences between SAR and LRMC Sphere products for SWH (left) and SSH (right)

To show that even curvature dependencies are observable, Figure 6.20 shows the differences of slope products. On the left side, no significant SWH differences are observable, which is consistent with the results shown in the previous two sections. However, it can be seen that SSH differences follow well the sea surface curvature and even small relative curvature differences are observable.

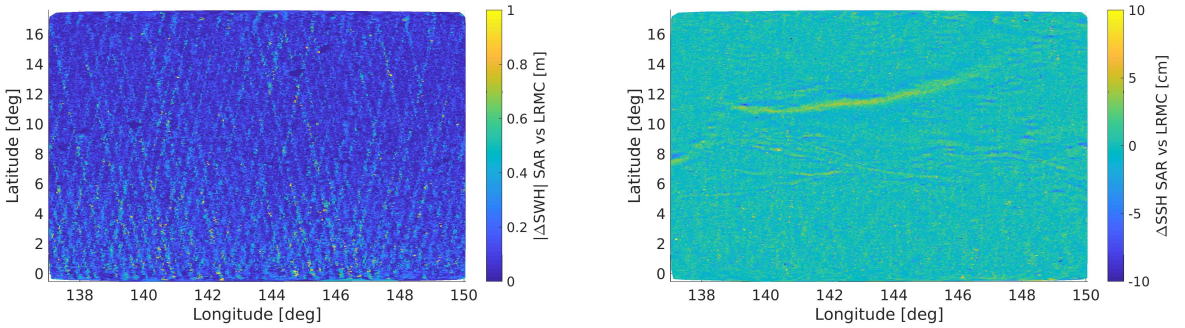

Figure 6.20: Relative differences between SAR and LRMC Slopes products for SWH (left) and SSH (right)

Of course, if a MSS study considering more than one year of data is investigated, a better SNR is to be expected. It might also be possible to detect time-varying quantities such as tides. However, this shall be investigated in an extending study.

In Figure 5.3, it was shown that an inconsistency of retrieved SWH values of RDSAR and LRMC/SAR exists depending on the sea state. As a three parameter retracker SINCS was used in that chapter that does not include the impact of vertical wave particle velocities, it is assumed that this causes the SWH differences. In this chapter, this new parameter σ_v is included in a new retracking scheme to investigate whether this is capable of reducing or even eliminating this effect. However, this means that a new retracking strategy needs to be developed to retrieve reasonable geophysical parameters.

This chapter is divided into four sections, the first of which introduces the region of interest being the North East Atlantic (NEA) and how the standard deviation of the vertical wave particle velocities σ_v will be estimated properly . This will be achieved by presenting and discussing several possible approaches from retracking the waveform, including the Range Integrated Power (RIP), considering the whole stack and applying a variable transform to increase the SNR.

The second section shows the cross comparison of all retracking results from LRMC and SAR with respect to the corresponding RDSAR values. RDSAR serves as a reference, as it was shown in chapter 3 that this processing mode is not affected by vertical motions of scattering surface elements. The cross comparison addresses the accuracy and precision of SLA, SWH and σ_0 retracking results.

As σ_v cannot be estimated in RDSAR, the ECMWF wave model [Janssen, 2002] is used as a reference for this parameter. The results of the cross comparison with ECMWF are shown and discussed in section 7.3. Additionally, the SWH of all retrackers and processing modes is compared with respect to this model to assure that both sea state parameters H_s and σ_v are consistent with each other.

In the final section, an in-situ validation is performed to verify the trueness and precision of the estimated geophysical parameters. This will be undertaken in the German bight with sea state data from the scientific platform FINO1 [Fischer et al., 2010] and sea levels from the tide gauge located at Helgoland-Binnenhafen (HELG). Table 7.1 provides an overview of the location of the in-situ stations used and the time span of the data available for this study.

Station	Longitude	Latitude	Available time span
HELG	7.9030° E	54.175° N	January 2010 to August 2018
FINO1	6.5878° E	54.0148° N	January 2010 to December 2015

Table 7.1: Overview of used in-situ stations

The location of both in-situ stations within the German bight is visualized in section 7.4, Figure 7.33.

The region of interest for this chapter is the NEA, shown in Figure 7.1, whereby the Mediterranean sea - which is also shown - is not considered. The benefit if this region is that it contains a high variety of SWH values up to ten metres. Additionally, it contains the German bight with a high density of buoys and tide gauges whose sea state and sea level observations can be used as ground truth. The geoid undulations and absolute deflections from vertical are shown for the sake of consistency with the two previous chapters.

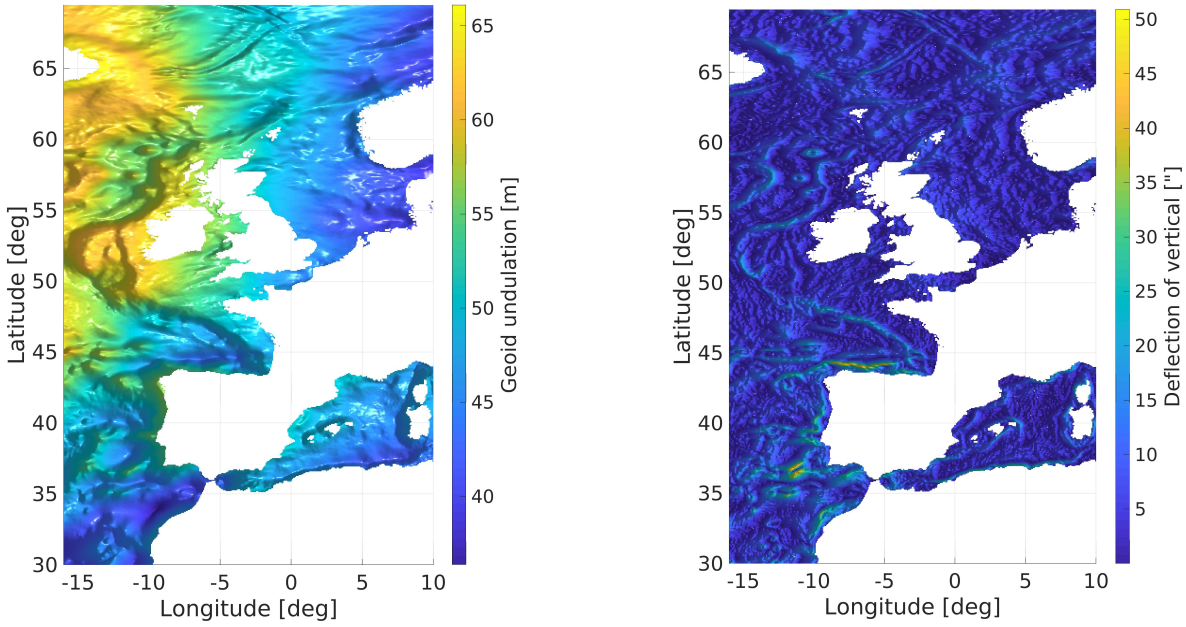

Figure 7.1: Geoid undulation (left side) and absolute deflection from vertical (right side) in the North East Atlantic.

To estimate σ_ν in a correct manner, it is necessary to take a look at the partial derivatives of the waveform model with respect to the estimated parameters as these provide an overview of how the retracker can distinguish them. If the partial derivatives with respect to different parameters are similar, the retracker is unable to estimate these parameters correctly due to high correlations. Figure 7.2 shows the partial derivatives of the waveform.

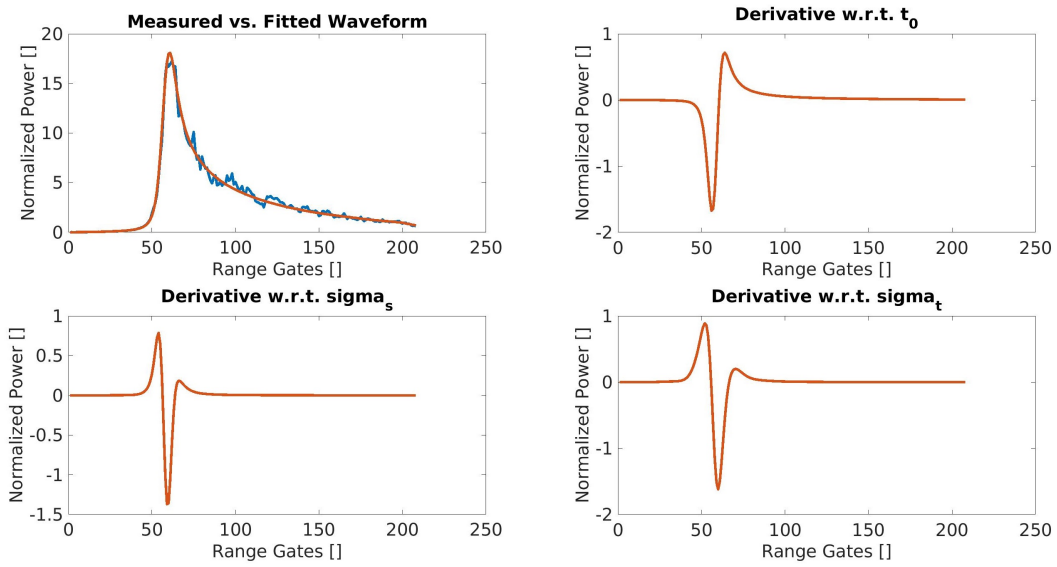

Figure 7.2: Waveform model and its partial derivatives w.r.t. estimated parameters.

In the top left of Figure 7.2 a measured SAR waveform (blue curve) is shown and its best-fitting modelled version (red curve). It is observable that the partial derivatives with respect to t_0 and σ_s - which is related to the SWH - show a different shape, which means that they are sufficiently different to allow the retracker to distinguish them. However, this is not the case for σ_t, which is related to σ_v, as its shape is very similar to the derivative with respect to σ_s. This leads to high correlations in the retracking process of circa -0.9 (derived by retracking a track in the German bight). Overall, it is not sufficient to retrack a SAR of LRMC waveform to retrieve SWH and σ_v correctly.

Another idea would be to include the RIP in the retracking to allow the retracker to differ between σ_s and σ_t. The partial derivatives of the RIP are shown in Figure 7.3, where in the top left a measured RIP and its best-fitting modelled version is shown.

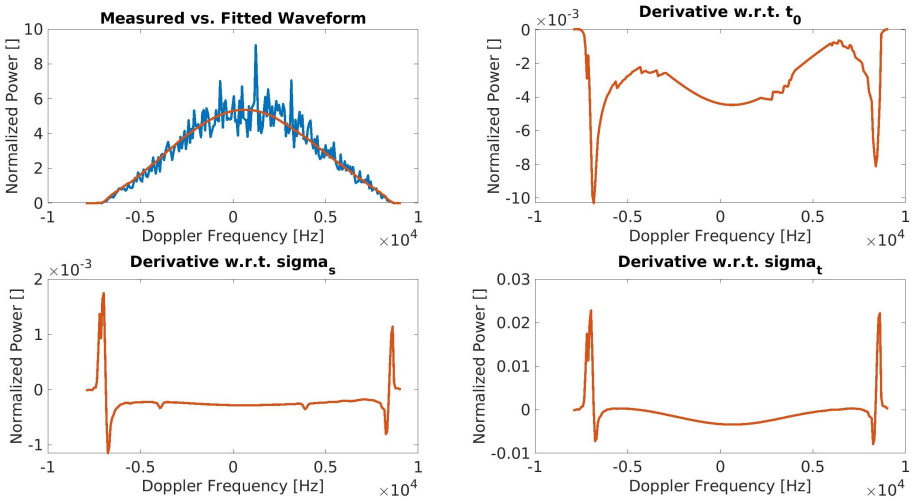

Figure 7.3: RIP and its partial derivatives w.r.t. estimated parameters.

It can be observed form Figure 7.3 that the RIP is very robust to changes of the estimated parameters as the magnitudes of the partial derivatives are small. However, even in this case the shape of the partial derivatives of σ_s and σ_t are similar. Nonetheless, the correlation coefficient of these reduces to -0.8 (computed with the same test track) which is still too high.

The next lower processing level of L1B would be the stack, which is shown in Figure 7.4 with its partial derivatives.

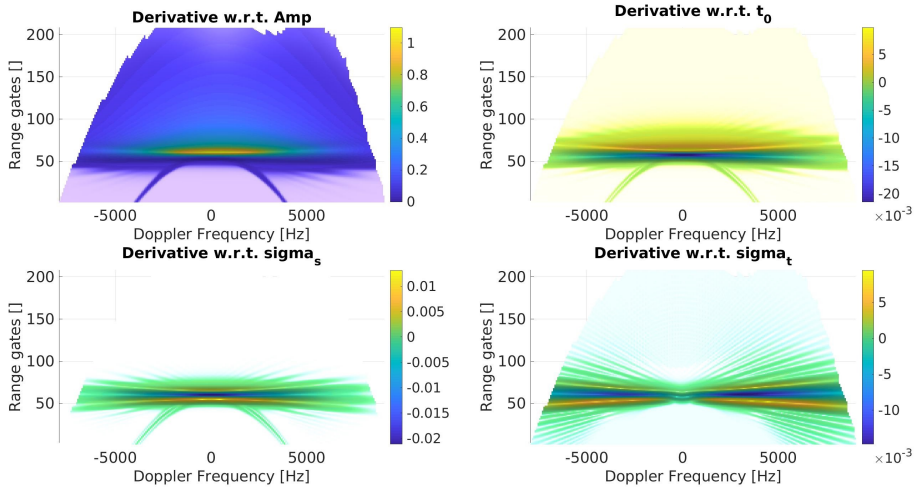

Figure 7.4: Stack and its partial derivatives w.r.t. estimated parameters for exponentially-distributed samples.

The partial derivatives with respect to σ_s and σ_t in Figure 7.4 show significant differences that are eliminated by calculating the waveform and RIP due to summations. It can be observed that at high Doppler frequencies the magnitude of the derivative with respect to σ_t is maximal, whereas for σ_s it is minimal. The opposite applies with low Doppler frequencies. Even the empirical correlation coefficient between these parameter reduces to -0.6, which is high but acceptable. This leads to the conclusion that the whole stack needs to be retracked to retrieve proper SWH and σ_v values.

As the samples within a stack follow an exponential distribution with a skewness of two [Weisstein, 2019], it can be assumed that retracking with a least squares based optimizer might result in biased retrieved geophysical parameters. This effect can be reduced by performing a variable transform on each sample $S_{k,l} \sim Exp\left(\frac{1}{s_{k,l}}\right)$ with $E[S_{k,l}] = s_{k,l}$ and $Var[S_{k,l}] = s_{k,l}^2$ given by

$$S_{k,l} \mapsto \frac{\sqrt[3.602]{S_{k,l}}}{\Gamma\left(1 + \frac{1}{3.602}\right)} \tag{7.1}$$

After the transformation, the distribution changes from exponential to Weibull (see Devore [2011, Section 4.5]) with a skewness of zero, a expected value of $E[S_{k,l}] = \sqrt[3.602]{s_{k,l}}$ and variance $Var[S_{k,l}] = 0.095\sqrt[3.602]{s_{k,l}^2}$. This means that the transform introduced in Eq. 7.1 creates a random variable close to a normal distribution, which is beneficial for the least squares optimizer assuming normal distributed samples. Another property of the transformed samples is that their SNR given as $SNR = \frac{E[S_{k,l}]}{\sqrt{Var[S_{k,l}]}}$ increases by 3.24 compared with the samples before the transform. Of course, this also applies for RDSAR waveforms if the pulses are transformed according to Eq. 7.1 before the summation. After the summation, this transform no longer works as it needs exponentially-distributed random variables as input. Obviously, this transform also needs to be applied to each sample of the modelled waveform or stack $s_{k,l}$ to keep it consistent with the expected value of the transformed samples.

$$s_{k,l} \mapsto \sqrt[3.602]{s_{k,l}} \tag{7.2}$$

Figure 7.5 shows the differences between SAR waveforms and RIPs before (upper part) and after the variable transform (lower part). The blue curves show the measured waveform or RIPs retrieved from the L1B product and the red curves the best-fitting modelled versions. It can be observed that the variable transform increases the weight of waveform bins with lower power compared with bins with higher power. The same applies for the RIP where higher Doppler frequencies contain more power after the transform. Overall, the SNR improved (see blue curves).

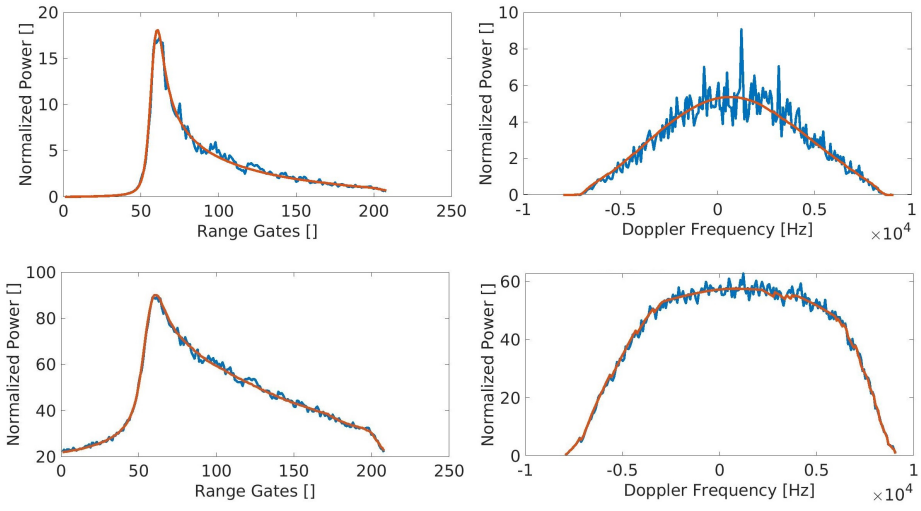

Figure 7.5: Comparison of the waveforms (left side) and the RIP (right side) for exponentially-distributed samples (upper half) and symmetric Weibull distributed samples (lower half).

Similar effects can be observed on the stack and its partial derivatives with respect to estimated parameter shown in Figure 7.6. The empirical correlation coefficient between σ_s and σ_t reduces to -0.3, which is half the value for the retracker without the variable transform.

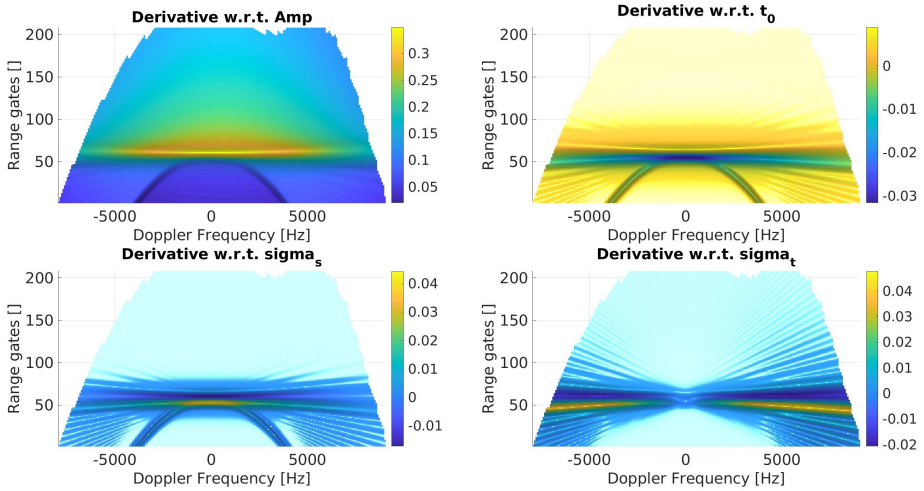

Figure 7.6: Stack and its partial derivatives regarding estimated parameters for symmetric Weibull distributed samples.

Although, the variable transform in Eq. 7.1 shows promising properties, it is necessary to validate retrieved geophysical parameters of all retrackers as otherwise it cannot be concluded that one algorithm is superior. The following listing details all retrackers considered in this chapter for each processing mode, whereas the retrackers with extension ZSK (zero skewness) consider the variable transformation according to Eq. 7.1.

- RDSAR
    1. SINC2: Three-parameter waveform retracker estimating A, t_0 and σ_s. No variable transform is applied.
    2. SINC2 ZSK: Similar to SINC2 but the pulses are transformed according to Eq. 7.1 before the summation.
- LRMC and SAR
    1. SINCS: Three-parameter waveform retracker estimating A, t_0 and σ_s. No variable transform is applied.
    2. SINCS ZSK: Similar to SINCS but the beams are transformed according to Eq. 7.1 before the multi-looking.
    3. SINCS-OV: Four parameter stack retracker estimating A, t_0, σ_s and σ_t. No variable transform is applied.
    4. SINCS-OV ZSK: Similar to SINCS-OV but the stack samples are transformed according to Eq. 7.1.

As previously mentioned, due to the variable transformation samples with small power gain a higher weighting, which affects the thermal noise estimation as small outliers in the thermal noise area of the stack or waveform lead to high errors in the estimation of this parameter. To overcome this issue, the thermal noise is introduced as a free parameter in SINC2 ZSK, SINC ZSK and SINCS-OV ZSK.

7.2 Cross Comparison

This section shows the cross comparison results of the three parameters estimable in the RDSAR processing mode, namely SLA (section 7.2.1), SWH (section 7.2.2) and σ_0 (section 7.2.3). All figures in this chapter follow the same structure. The upper part shows results from the retracker that does not include vertical wave particle velocities of scattering elements, unlike the lower part. On the left side of each figure, retrackers with standard exponentially-distributed samples are shown and on the right side results that include the variable transform of Eq. 7.1 are considered. In this and the next section, CryoSat-2 data located in the NEA and within the year 2013 are considered.

7.2.1 Cross Comparison of Altimetry-Retrieved SLA

The first geophysical parameter considered in the cross comparison between RDSAR and the other processing modes is the SLA calculated by Eq. 4.1.

Histogram of SLA values

Figure 7.7 shows the histogram of occurring SLA values and shall provide a first impression about the quality of the retrieved values of each processing mode. With exception of Figure 7.7 d), all histograms shows a good consistency with each other. The curves of LRMC and SAR overlap. It is worth mentioning that Figure 7.7 b) showing retracker results with transformed samples have the best consistency as in the other plots biases of circa 1 cm between RDSAR and SAR/LRMC exist.

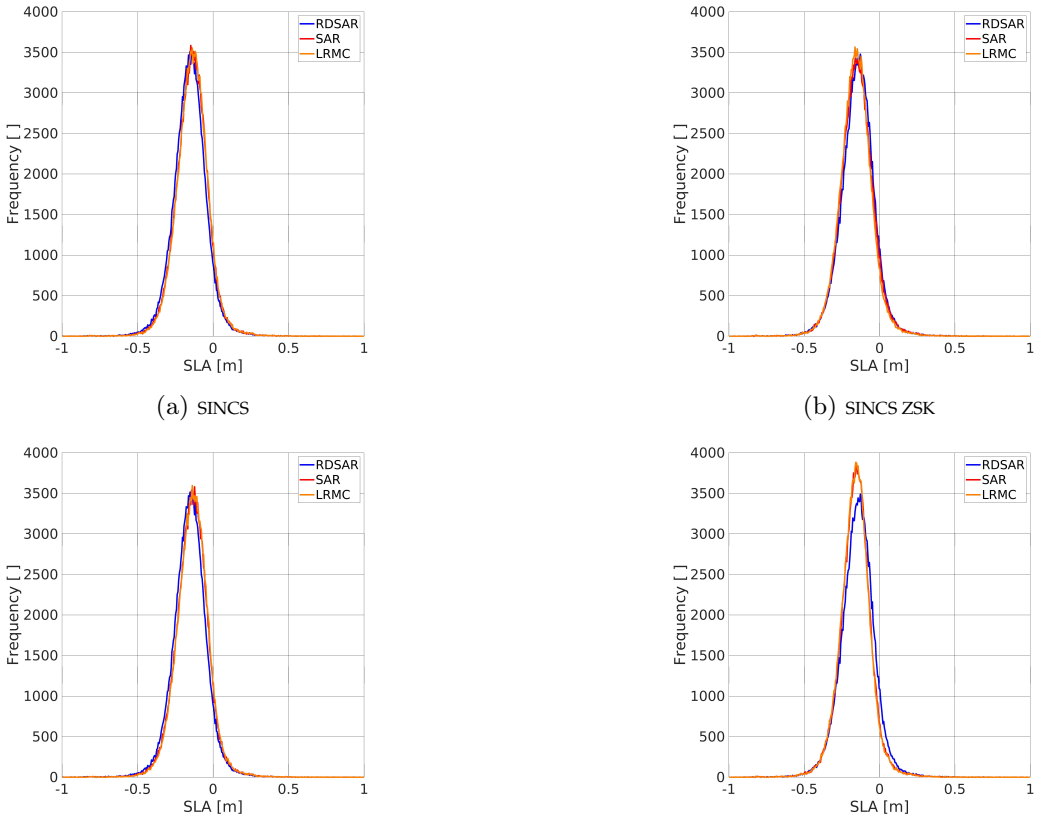

(a) SINCS (b) SINCS ZSK

(c) SINCS-OV (d) SINCS-OV ZSK

Figure 7.7: Histogram of occurring SLA values in the NEA for all considered retracker and processing modes.

Accuracy of SLA with Respect to RDSAR

Figure 7.8 shows the accuracy of retrieved SAR SLA values with respect to the RDSAR results. The left plots of Figure 7.8 are consistent, showing no significant differences which leads to the assumption that SINCS-OV behaves well for SLA.

However, a sea state dependency of the results from both retrackers is observable, varying from -1 to 2 cm for the mean differences (blue curves).

For SINCS ZSK shown in Figure 7.8 b), this sea state dependency of the mean differences (blue curve) becomes smaller for wave heights greater than two metres, varying from -1 to 0 cm, although for a smaller sea state it slightly increases up to 2 cm.

Observing Figure 7.8 d) showing the differences between SINC2 ZSK and SINCS-OV ZSK gives large mean differences of up to -6 cm for SWH smaller than two metre, whereas for higher sea state the mean differences rapidly converge towards zero. This leads to the assumption that SINCS-OV ZSK have problems in retrieving consistent SLA estimations at small sea states, whereas for SWH values greater than two metre it gives the best results compared with the other retrackers.

Making a statement with respect to precision is not possible from Figure 7.8 as the overall noise is similar in all four plots. Possible differences are blurred out due to the noise coming from RDSAR, which is expected to have larger standard deviations than the LRMC and SAR SLA values.

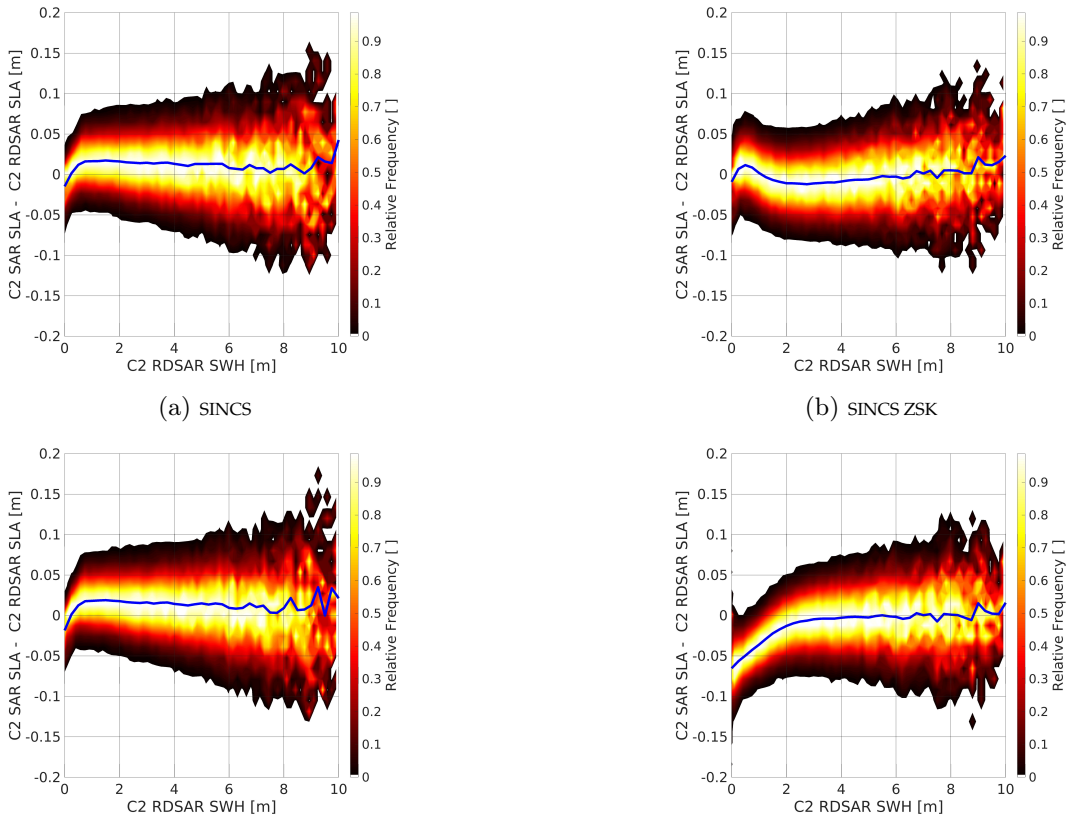

(a) SINCS (b) SINCS ZSK

(c) SINCS-OV (d) SINCS-OV ZSK

Figure 7.8: Two-dimensional histogram of differences between SAR and RDSAR SLA with respect to RDSAR SWH.

For LRMC the plots shown in Figure 7.9 are very similar to Figure 7.8, which is a good result as it means that the LRMC processing leads to consistent SLA results with respect to SAR processing.

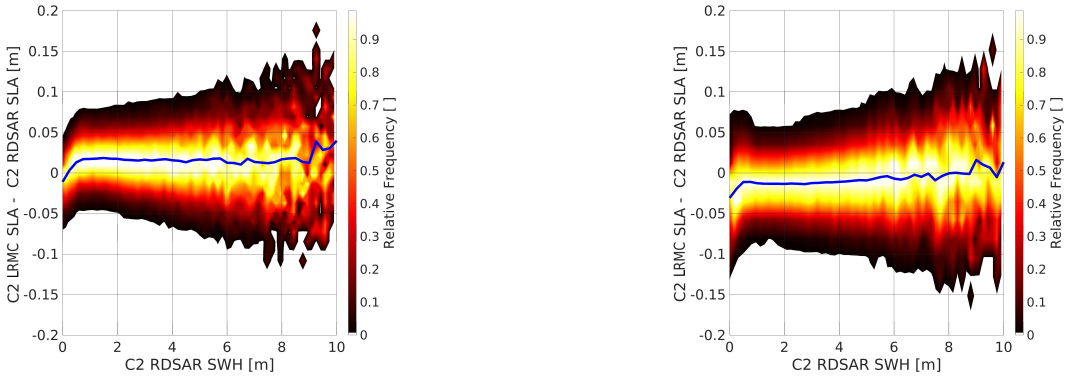

(a) SINCS (b) SINCS ZSK

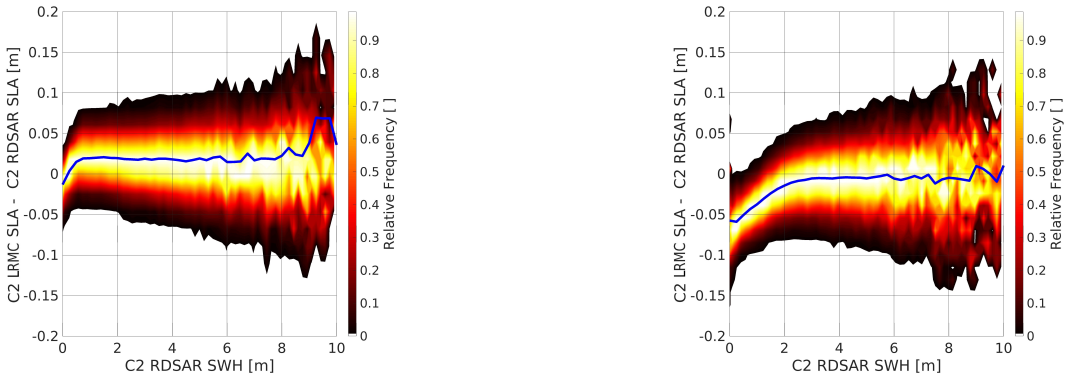

(c) SINCS-OV (d) SINCS-OV ZSK

Figure 7.9: Two-dimensional histogram of differences between LRMC and RDSAR SLA with respect to RDSAR SWH.

Precision of SLA

Figure 7.10 shows the empirical standard deviations of th 1 Hz SLA RDSAR valuese retrieved. It can be observed that both SINC2 (left plot) and SINC2-ZSK (right plot) produce similar SLA standard deviation varying from 1 to 3.5 cm, whereas the values for SINC2 ZSK are around two millimetre smaller and therefore slightly more precise.

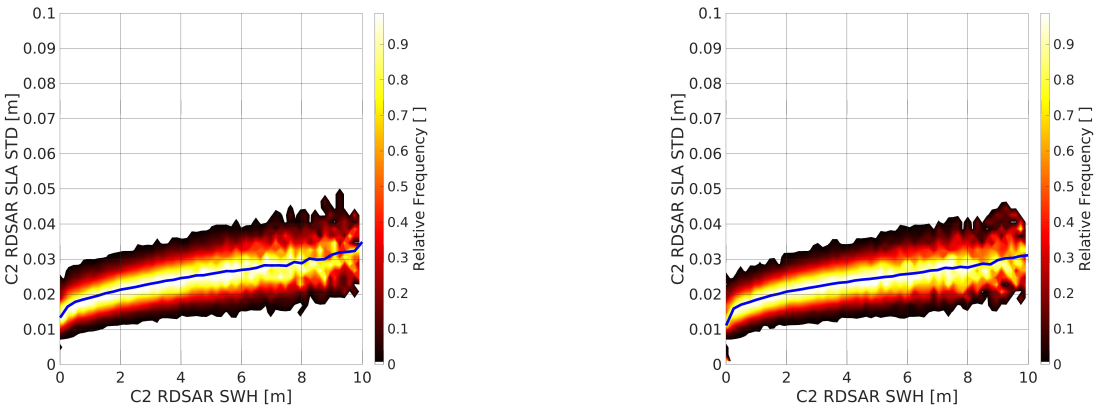

(a) SINC2 (b) SINCS2 ZSK

Figure 7.10: Two-dimensional histogram of RDSAR SLA standard deviations with respect to RDSAR SWH.

Figure 7.11 shows the precision of SAR SLA values retrieved with respect to RDSAR SWH results. The left plots of Figure 7.11 are consistent showing no significant differences, which means that SINCS-OV gives SLA values with the same precision as SINCS. However, a sea state dependency of the standard deviations from both retrackers is observable, varying from 0.8 to 4 cm for the mean standard deviations (blue curves). Overall, for SWH values less than seven metres the SAR results are more precise than corresponding RDSAR results, whereas for higher sea state RDSAR is more precise.

For SINCS ZSK shown in Figure 7.11 c) the mean standard deviations (blue curve) is smaller than those from SINCS or SINCS-OV, varying from 0.8 to 3 cm. This means that the variable transform leads to more precise SLA results.

Figure 7.11 d), showing the standard deviations of SINCS-OV ZSK gives similar results than SINCS ZSK, giving values varying from 0.8 to 3 cm. This means that SINCS ZSK and SINCS-OV ZSK are consistent with respect to SLA standard deviations.

The effect that RDSAR standard deviations increase slower than in the SAR processing is explainable by the Walsh limit, which states that the effective number of looks for RDSAR is proportional to the SWH (see Smith [2011]). Accordingly, the SNR increases at a higher sea state leading to more precise results. Of course, this also applies for SAR, although the maximal effective number of looks is greater than the number of averaged beams for SWH of more than two metres. This means that the positive effect of higher possible SNR is eliminated by the number of available beams.

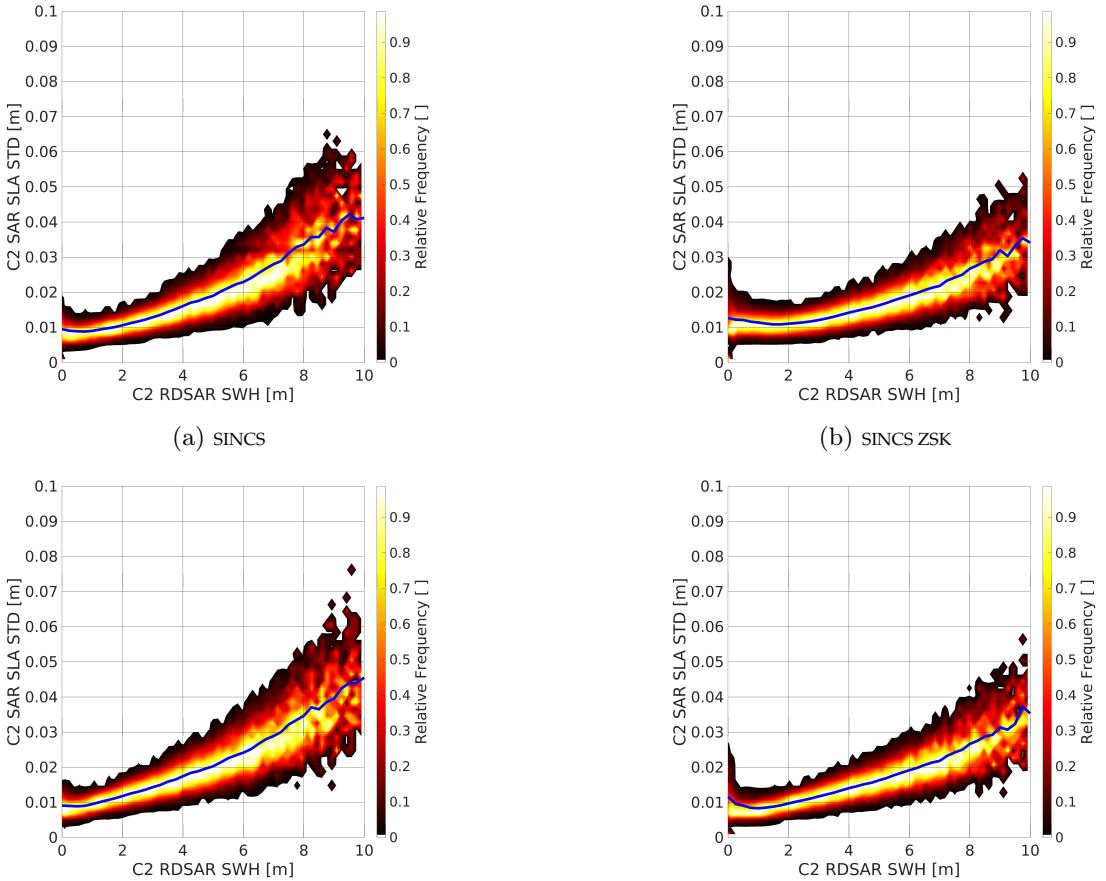

(a) SINCS (b) SINCS ZSK

(c) SINCS-OV (d) SINCS-OV ZSK

Figure 7.11: Two-dimensional histogram of SAR SLA standard deviations with respect to RDSAR SWH.

Compared with the standard deviation retrieved in SAR processing mode, LRMC shows a different behaviour. Figure 7.12 shows the precision of retrieved SLA values with respect to RDSAR SWH results. It is observable that the SLA precisions of all LRMC retracker increases more smoothly than in SAR, which is an interesting result as this means that LRMC benefits from higher possible SNR according to the Walsh limit. For SINCS, the standard deviation varies from 0.6 to 1.6 cm, whereas for SINCS-OV it varies from 0.6 to 2.0 cm.

For SINCS ZSK shown in Figure 7.12 c) the mean standard deviations (blue curve) is slightly smaller than those from SINCS or SINCS-OV, varying from 0.6 to 1.5 cm. This means that the variable transform leads to approximately equally precise SLA results.

Observing Figure 7.12 d) showing the standard deviations of SINCS-OV ZSK gives similar results than SINCS ZSK, giving values varying from 0.6 to 1.5 cm. This means that SINCS ZSK and SINCS-OV ZSK are consistent with respect to SLA standard deviations.

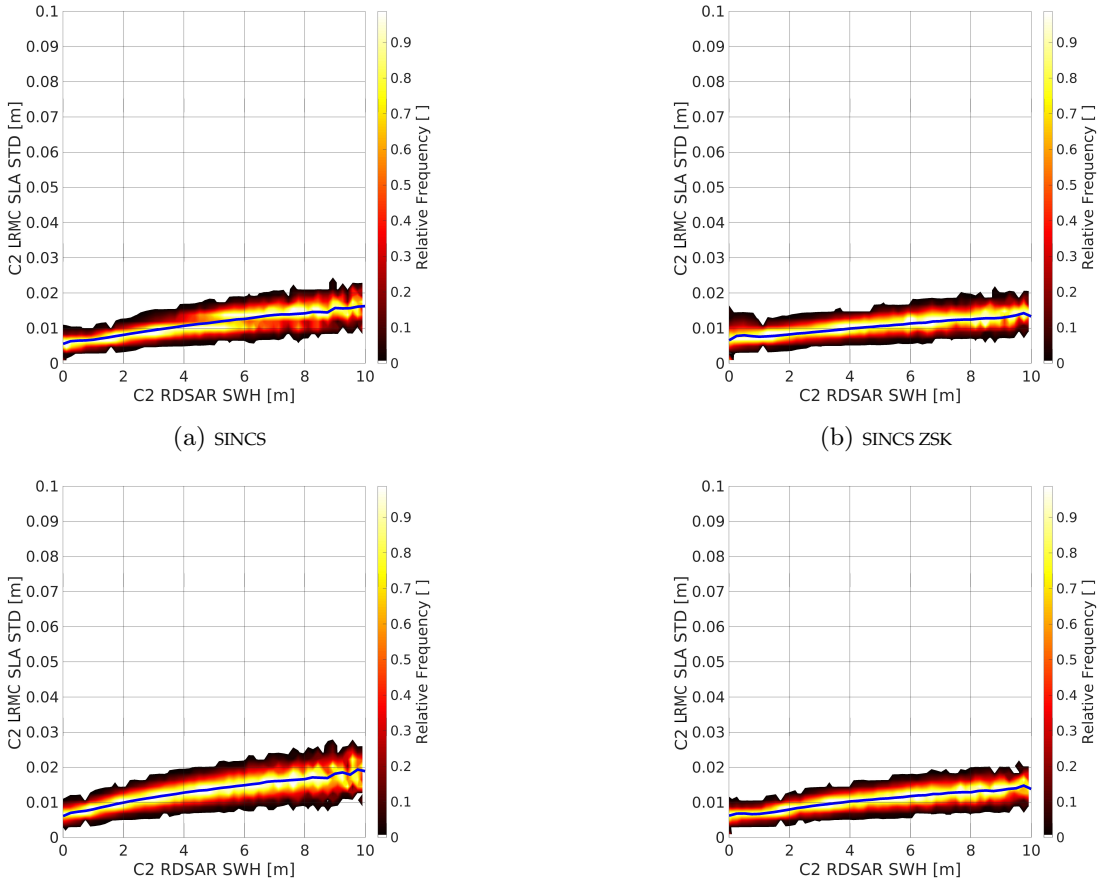

(a) SINCS (b) SINCS ZSK

(c) SINCS-OV (d) SINCS-OV ZSK

Figure 7.12: Two-dimensional histogram of LRMC SLA standard deviations with respect to RDSAR SWH.

Scatterplots of retrieved SLA values with respect to RDSAR

Figure 7.13 shows the scatterplot of retrieved SAR SLA values with respect to RDSAR SLA. The colour in each figure corresponds to the overall frequency of the values. In Figure 7.13 a), the scatterplot between SINCS and SINC2 SLA values is shown. It can be observed that the consistency between the two datasets is high due to a regression slope of 0.963 and a empirical correlation coefficient of 0.956. The standard deviation of the differences is 3.3 cm with a bias of 1.4 cm, which is a good result as it shows that the two datasets provide similar results with a good quality.

If a variable transform is performed in the L1B processing according to Eq. 7.1 shown in Figure 7.13 b), the standard deviation of the differences reduces to 3.0 cm and the mean difference between SINC2 ZSK and SNCS ZSK becomes -0.6 cm. This means that the variable transform results in more consistent RDSAR and SAR SLA values. The regression slope and the correlation coefficient remains approximately equal.

If the vertical wave particle velocity is introduced in the retracking, the results are comparable to SINCS. As shown in Figure 7.13 c), the differences between the statistic parameters are insignificantly small. This means that SINCS-OV is able to produce SLA values consistent with SINC2 and SINCS.

However, by observing Figure 7.13 d) showing the scatteprlot between SINC2 ZSK and SINCS-OV ZSK, the overall consistency is worse than in Figure 7.13 b). The regression slope becomes 0.905 which is less than for the other retrackers and the mean difference is -1.5 cm. Overall, it can be stated that if comparing all occuring SLA values, SINCS-OV ZSK is the least consistent retracker. However, as shown in Figure 7.8 d) this only applies for small sea states. For SWH greater than two metres, SINCS-OV ZSK produces the most consistent SLA values.

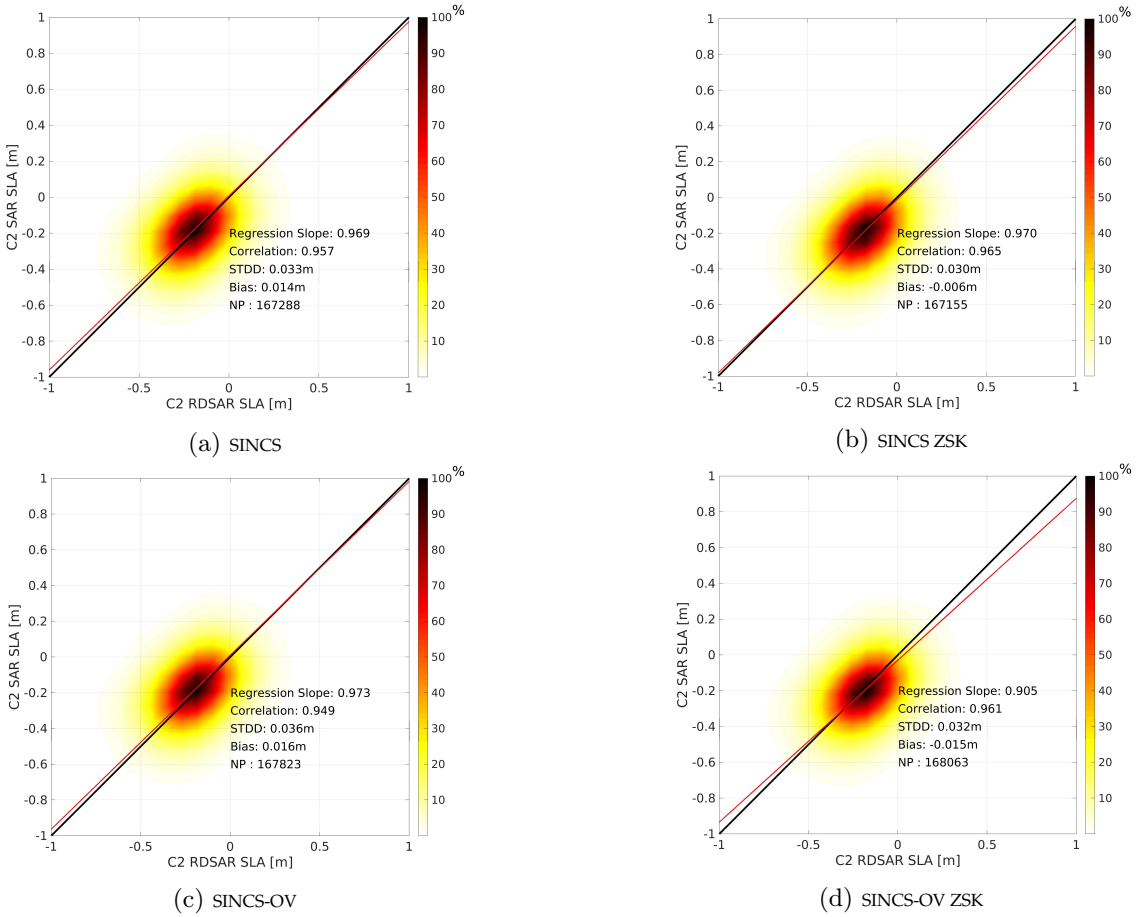

(a) SINCS (b) SINCS ZSK

(c) SINCS-OV (d) SINCS-OV ZSK

Figure 7.13: Scatterplots of RDSAR and SAR SLA and their statistical parameters.

Figure 7.14 shows the scatterplot of retrieved LRMC SLA values with respect to RDSAR SLA. In Figure 7.14 a), the scatterplot between SINCS and SINC2 SLA values is shown. It can be observed that the consistency between both datasets is high due to a regression slope of 0.963 and a empirical correlation coefficient of 0.956. The standard deviation of the differences is 3.3 cm with a bias of 1.6 cm, which is consistent with the result shown in Figure 7.13.

If a variable transform is performed in the L1B processing according to Eq. 7.1 shown in Figure 7.14 b), the standard deviation of the differences becomes 3.2 cm and the mean difference between SINC2 ZSK and SNCS ZSK becomes -1.2 cm. This means that the variable transform for LRMC does not give better results. The regression slope becomes slightly lower, whereas the correlation coefficient remains approximately the same.

If the vertical wave particle velocity is introduced in the retracking, the results are comparable to SINCS. As shown in Figure 7.14 c), the differences between the statistic parameters are insignificantly small. This means that SINCS-OV is able to produce SLA values consistent with SINC2 and SINCS even for LRMC processing.

On the other hand, by observing Figure 7.14 d) showing the scatteprlot between SINC2 ZSK and SINCS-OV ZSK, the overall consistency is worse than in Figure 7.14 b). The regression slope becomes 0.898, which is less than for the other retrackers and the mean difference is -1.6 cm. This means that SINCS-OV ZSK has the same behaviour as SINCS-OV ZSK in SAR mode. However, even for LRMC the worse results occur only for SWH values smaller than two metres as shown in Figure 7.9 d). For a higher sea state, SINCS-OV ZSK gives the most consistent results with SINC2 ZSK.

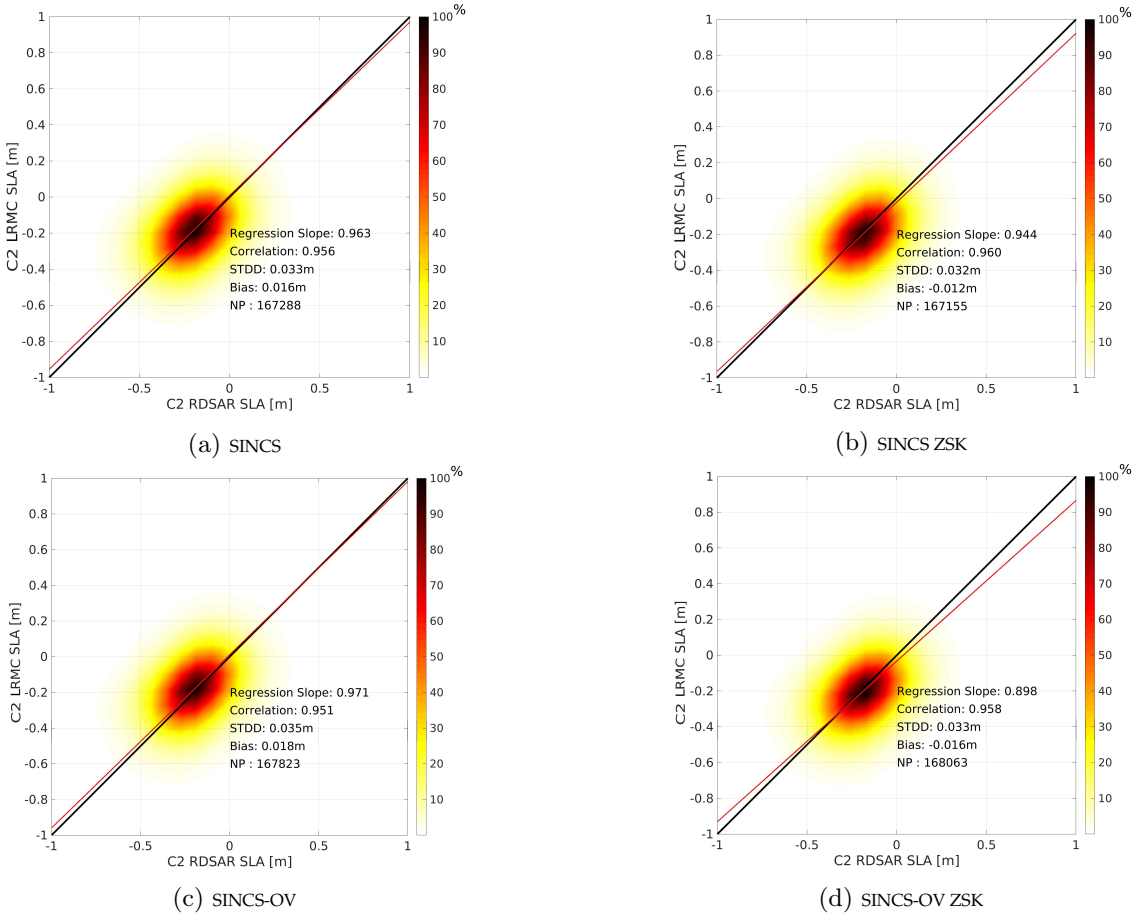

(a) SINCS (b) SINCS ZSK

(c) SINCS-OV (d) SINCS-OV ZSK

Figure 7.14: Scatterplots of RDSAR and LRMC SLA and their statistical parameters.

7.2.2 Cross Comparison of Altimetry-Retrieved SWH

The second considered parameter is the SWH, which is computed by multiplying the estimated σ_s with two times the speed of light (see enumeration on page 37). This parameter holds major interest as the aim of this study is to improve the consistency between the RDSAR and SAR/LRMC sea state parameters.

Histogram

As in the previous subsection, the overall occurrence of SWH values retrieved from different processing modes and retracker is considered in Figure 7.15. Additionally, the histogram of ECMWF SWH is also shown in this figure as an additional reference. Overall, values from zero to ten metres SWH occur in year 2013 in the test area. Whereas SWH values retrieved by RDSAR processing are consistent with ECMWF, this does not apply for SAR and LRMC. It can be observed from Figure 7.15 a) and b) that LRMC and SAR retrackers estimate SWH values with different frequencies than RDSAR and ECMWF. In Figure 7.15 b) showing SINCS ZSK results, even the SAR and LRMC do not overlap and in this plot the worst consistency is observed compared with RDSAR and ECMWF. However, in all other plots they overlap. On the other hand, if the vertical motion of scattering elements is considered by using SINCS-OV or SINCS-OV ZSK (shown in plot c) and d)) at SWH values greater than three metres, the histograms show a better consistency. At low sea states, it appears that these retrackers are unable to estimate small SWH values as these do not occur in Figures 7.15 c) and d).

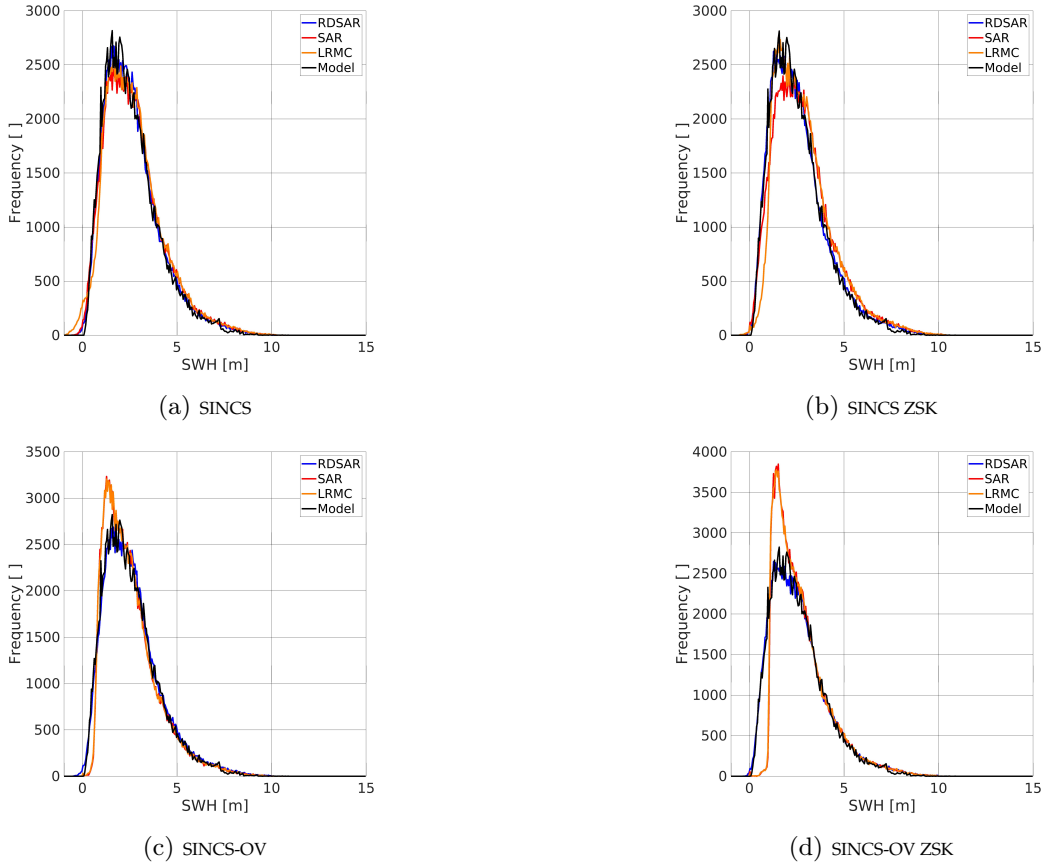

(a) SINCS (b) SINCS ZSK

(c) SINCS-OV (d) SINCS-OV ZSK

Figure 7.15: Histogram of occurring SWH values in the NEA for all considered retracker and processing modes.

Figure 7.16 shows the accuracy of retrieved SAR SWH values with respect to the RDSAR results. It can be observed that each SAR retracker shows different results. For SINCS shown in Figure 7.16 a), a sea state-dependent mean difference is observable, varying from zero cm at SWH of around one metre up to 20 cm for a large sea state.

If a variable transform acording to Eq. 7.1 is applied in the L1B processing, the precision becomes much better observable due to the narrower histogram in y direction. However, on the other hand the mean differences (blue curve) becomes larger, varying from zero at SWH around one up to 30 cm at high wave heights. This means that the overall accuracy worsens.

For SINCS-OV shown in Figure 7.16 c), the precision at SWH larger than two metres is comparable to Figure 7.16 a), although at a lower sea state large mean differences are observable and even at high SWH values a mean difference up to -40 cm is observable. This leads to the result that SINCS-OV gives the worst accuracy with respect to RDSAR.

On the other hand Figure 7.16 d) showing the differences between SINC2 ZSK and SINCS-OV ZSK gives mean differences up to 90 cm for SWH smaller than two metres large, whereas for higher sea state the mean differences rapidly converge towards zero. This leads to the assumption that SINCS-OV ZSK has problems in retrieving consistent SWH estimations at small sea states, whereas for SWH values greater than two metres it gives the best results compared with the other retrackers. Additionally, the observable precision becomes better than in the other cases.

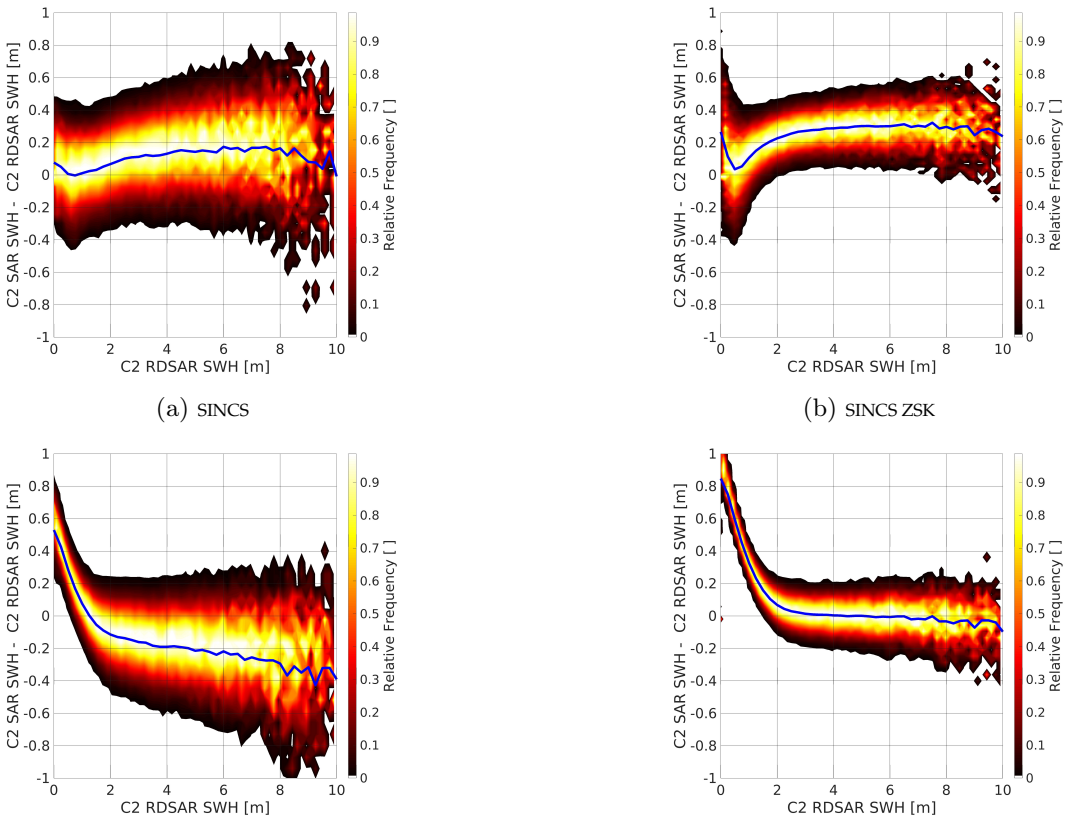

(a) SINCS (b) SINCS ZSK

(c) SINCS-OV (d) SINCS-OV ZSK

Figure 7.16: Two-dimensional histogram of differences between SAR and RDSAR SWH with respect to RDSAR SWH.

For LRMC, the plots shown in Figure 7.17 are similar at SWH larger than two metres to Figure 7.16, which is a good result as it means that the LRMC processing leads to consistent SLA results with respect to SAR processing. However, at smaller sea states SINCS and SINCS ZSK show significant differences, which need to be investigated.

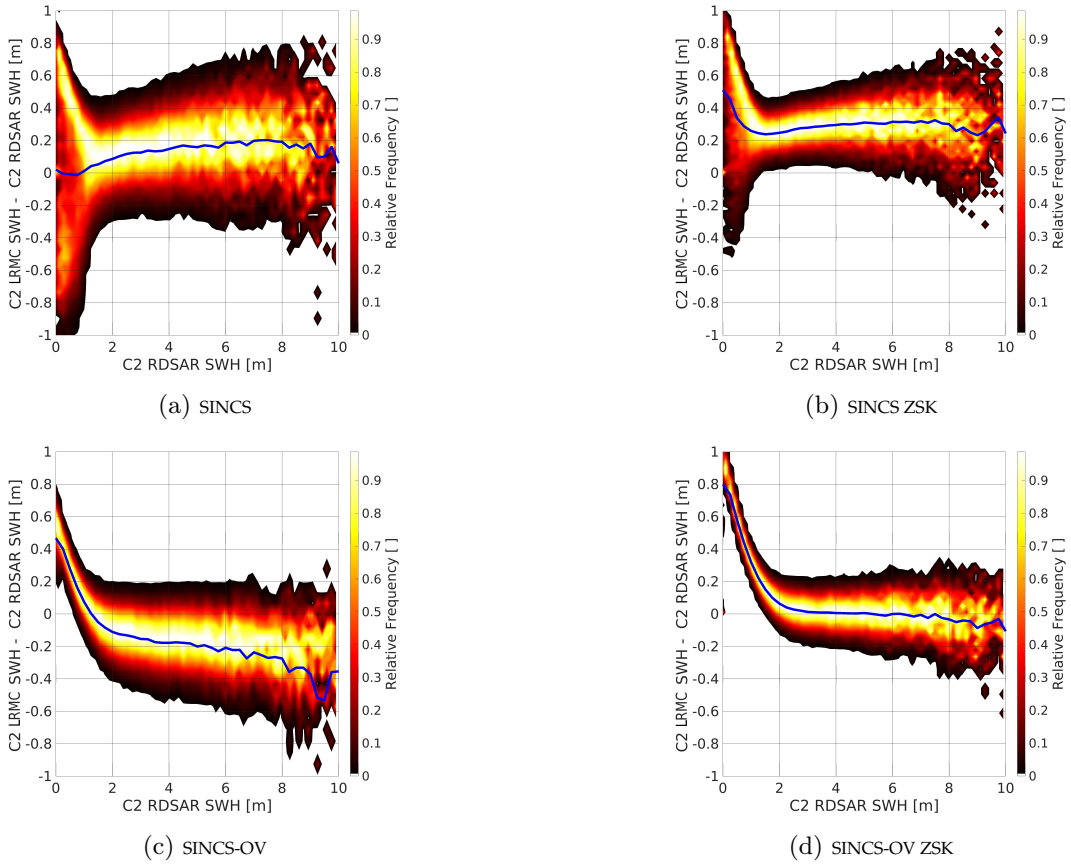

(a) SINCS (b) SINCS ZSK

(c) SINCS-OV (d) SINCS-OV ZSK

Figure 7.17: Two-dimensional histogram of differences of LRMC and RDSAR SWH with respect to RDSAR SWH.

Precision of SWH

Figure 7.18 shows the empirical standard deviations of the retrieved 1 Hz SWH RDSAR values. It can be observed that SINC2 (left plot) and SINC2 ZSK (right plot) produce different SWH standard deviations, varying from 10 to 20 cm for SINC2 and 8 to 10 cm for SINC2 ZSK. This means that RDSAR SWH benefits from the variable transform.

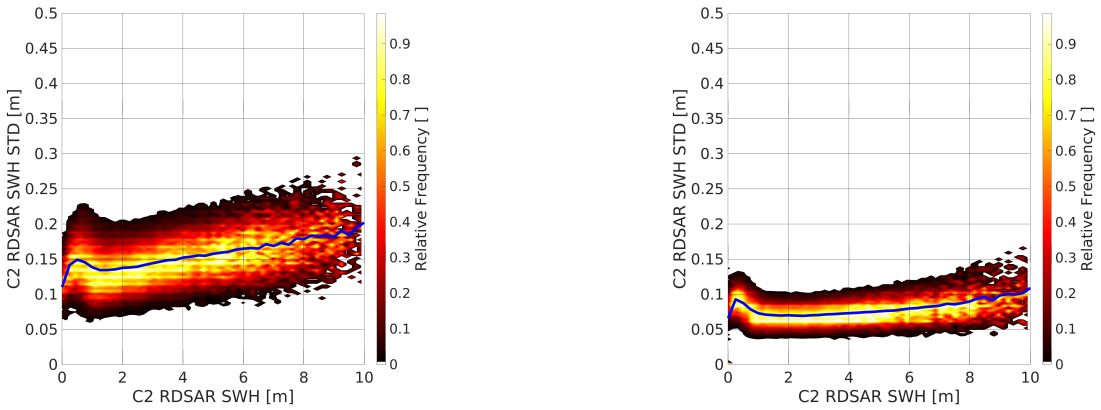

(a) SINC2 (b) SINC2 ZSK

Figure 7.18: Two-dimensional histogram of RDSAR SWH standard deviations with respect to RDSAR SWH.

Figure 7.19 shows the precision of retrieved SAR SWH values with respect to RDSAR SWH results. Overall, for SWH values less than seven metres the SAR results are more precise than corresponding RDSAR results, whereas for higher sea states RDSAR is more precise. The explanation for this phenomena is the same as for the SLA precisions, namely the Walsh limit. By comparing Figure 7.11 a) with c), it can be observed that SINCS SWH values are slightly more precise than SINCS-OV for SWH greater than two metres. For lower sea states, the standard deviations of SINCS-OV are smaller, although as shown in Figure 7.16 at this interval the accuracy of SINCS-OV is worse. The standard deviations of both retrackers varies between 8 and 30 cm.

A similar result can be observed by comparing Figure 7.19 b) and d) showing the results of transformed L1B products, whereby it can be seen that the retrieved standard deviations are similar for SWH larger than two metres. Even in these cases, for smaller sea states the retrieved standard deviation of SINCS-OV ZSK is smaller but the accuracy is worse (see Figure 7.16). The standard deviations of both products vary between 4 to 22 cm, which is less than in Figure 7.19 a) and c) showing results from retracking L1B products that were not transformed according to Eq. 7.1. This means that also SWH estimations benefit from this procedure.

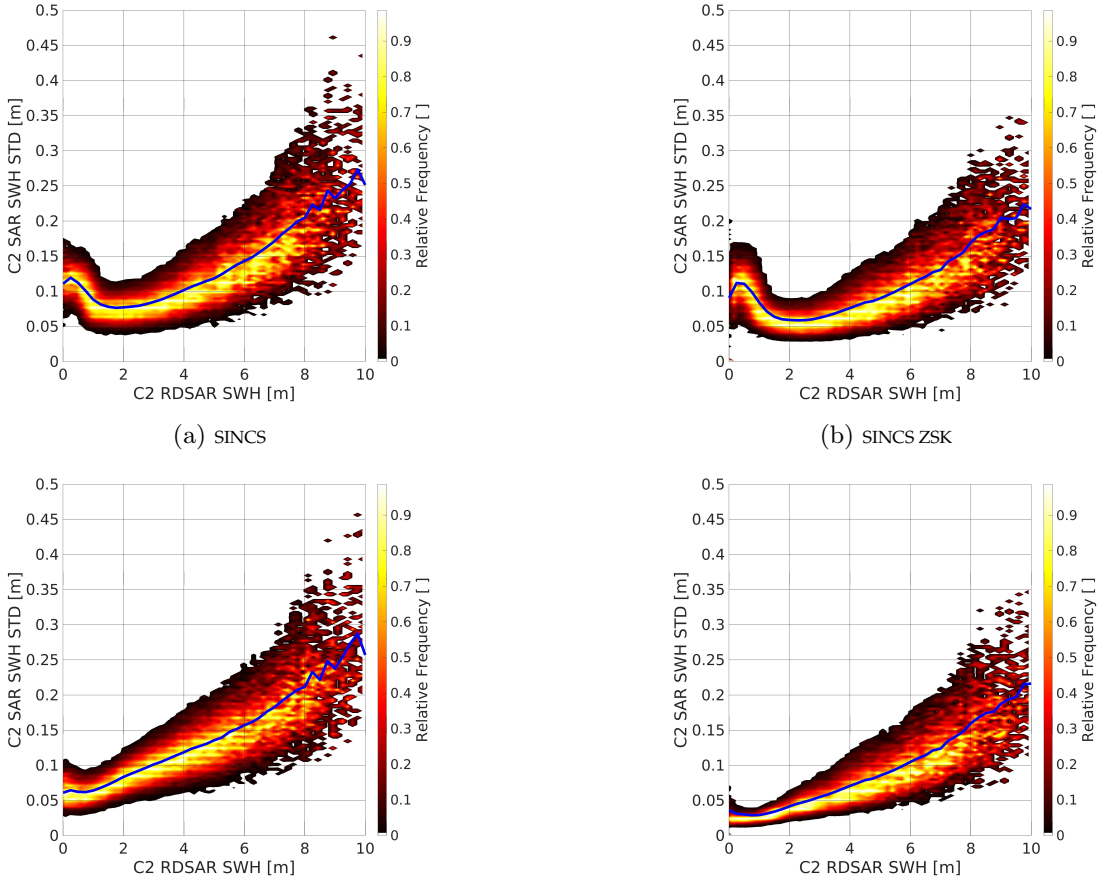

(a) SINCS (b) SINCS ZSK

(c) SINCS-OV (d) SINCS-OV ZSK

Figure 7.19: Two-dimensional histogram of SAR SWH standard deviations with respect to RDSAR SWH.

Compared with the standard deviation retrieved in the SAR processing mode, LRMC shows a different behaviour. Figure 7.20 shows the precision of retrieved SWH values with respect to RDSAR SWH results. It is observable that the SWH precisions of all LRMC retrackerss increases more smoothly than in SAR, which is an interesting result as this means that LRMC benefits from higher possible SNR according to the Walsh limit. For SINCS, the standard deviation varies from 4 to 7 cm, whereas for SINCS-OV it varies from 6 to 13 cm. However, at low sea states a higher variety of occurring standard deviations can be observed for SINCS and SINCS ZSK. Similar behaviour was already seen in Figure 7.17 and needs to be investigated.

For SINCS ZSK shown in Figure 7.20 c), the mean standard deviations (blue curve) is smaller than these from SINCS or SINCS-OV varying from 3 to 9 cm. This means that the variable transform leads to more precise SWH results.

Observing Figure 7.20 d) shows the standard deviations of SINCS-OV ZSK with similar results as SINCS ZSK, giving values varying from 3 to 9 cm. This means that SINCS ZSK and SINCS-OV ZSK are consistent with respect to SWH standard deviations, although - as already stated in the SAR case for small sea state - the accuracy is worse for all retrackers.

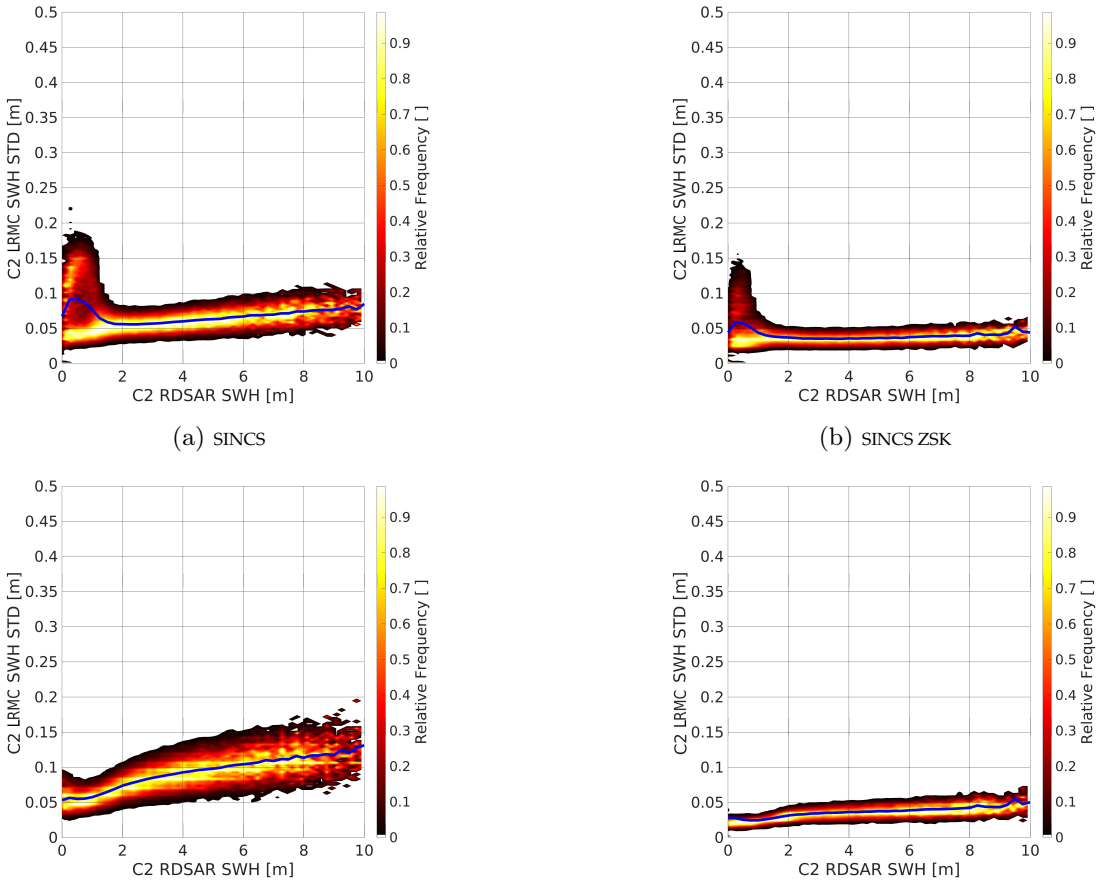

(a) SINCS (b) SINCS ZSK

(c) SINCS-OV (d) SINCS-OV ZSK

Figure 7.20: Two-dimensional histogram of LRMC SWH standard deviations with respect to RDSAR SWH.

Due to the high differences at low sea states, scatter-plots are not discussed as these SWH intervals would worsen the quality of the regression slopes and the overall retrieved statistical parameters so much that a comparison of these would not be helpful in evaluating the quality of the retackers.

7.2.3 Cross Comparison of Altimetry-Retrieved σ_0

The second considered parameter is σ_0, which is computed with Eq. 4.3. As the differences between the procession modes and retrackers are small, only a discussion of the accuracy with respect to RDSAR is performed.

Accuracy of σ_0 with respect to RDSAR

Figure 7.21 shows the accuracy of retrieved SAR σ_0 values with respect to the RDSAR results. The left plots of Figure 7.21 are consistent, showing no significant differences, which leads to the assumption that SINCS-OV behaves well for σ_0. Overall, constant mean differences of 0.04 dB are observable in both cases, which are sufficiently small to be neglected.

For SINCS ZSK shown in Figure 7.21 b), the mean differences (blue curve) show similar behaviour, demonstrating a mean difference of 0.03 dB with respect to SINC2 ZSK.

Observing Figure 7.21 d) showing the differences between SINC2 ZSK and SINCS-OV ZSK gives the best result as the mean differences are close to zero.

However, due to very small differences, a statement about which retracker is the best to estimate σ_0 cannot be made.

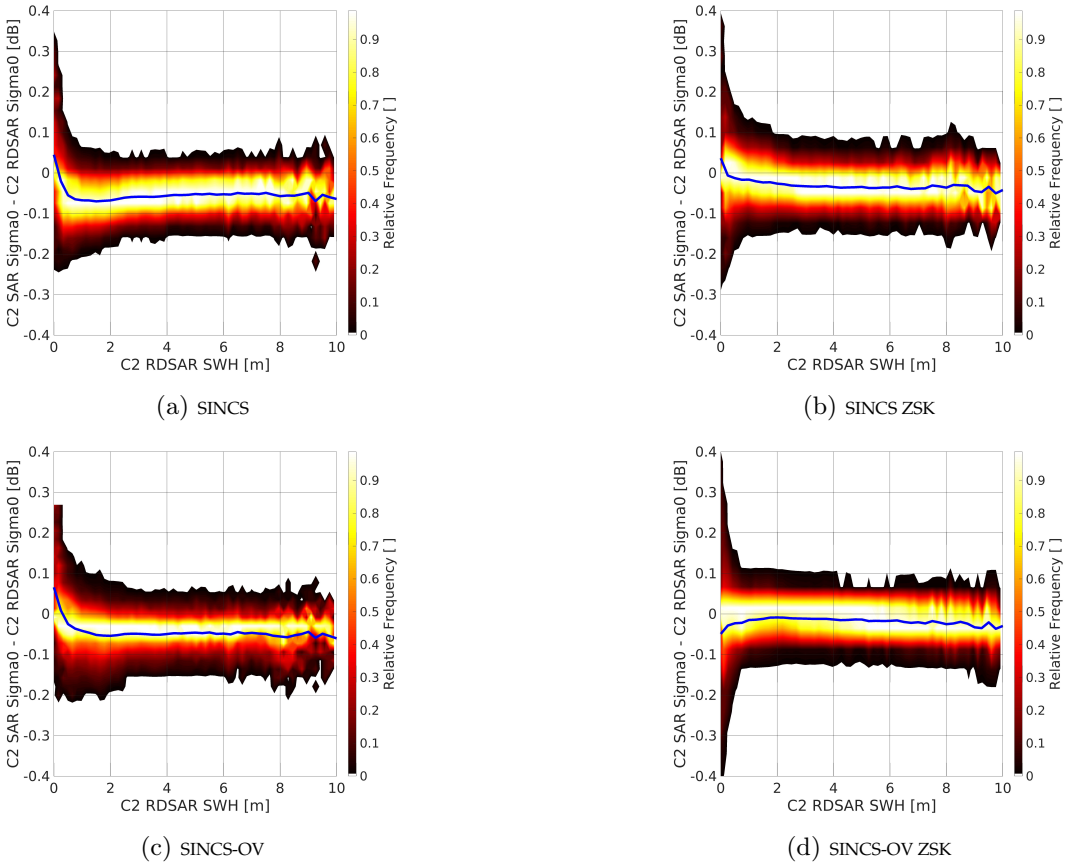

(a) SINCS (b) SINCS ZSK

(c) SINCS-OV (d) SINCS-OV ZSK

Figure 7.21: Two-dimensional histogram of differences between SAR and RDSAR σ_0 values with respect to RDSAR SWH.

For LRMC the plots shown in Figure 7.22 are very similar to Figure 7.21, although the scattering of the differences is smaller than for SAR. This can be explained by the footprint of LRMC, which is the same as for RDSAR. Therefore, the results are slightly more consistent. However, as the differences are small in all cases, it cannot be stated which mode or retracker is superior to the others in the context of σ_0 estimation.

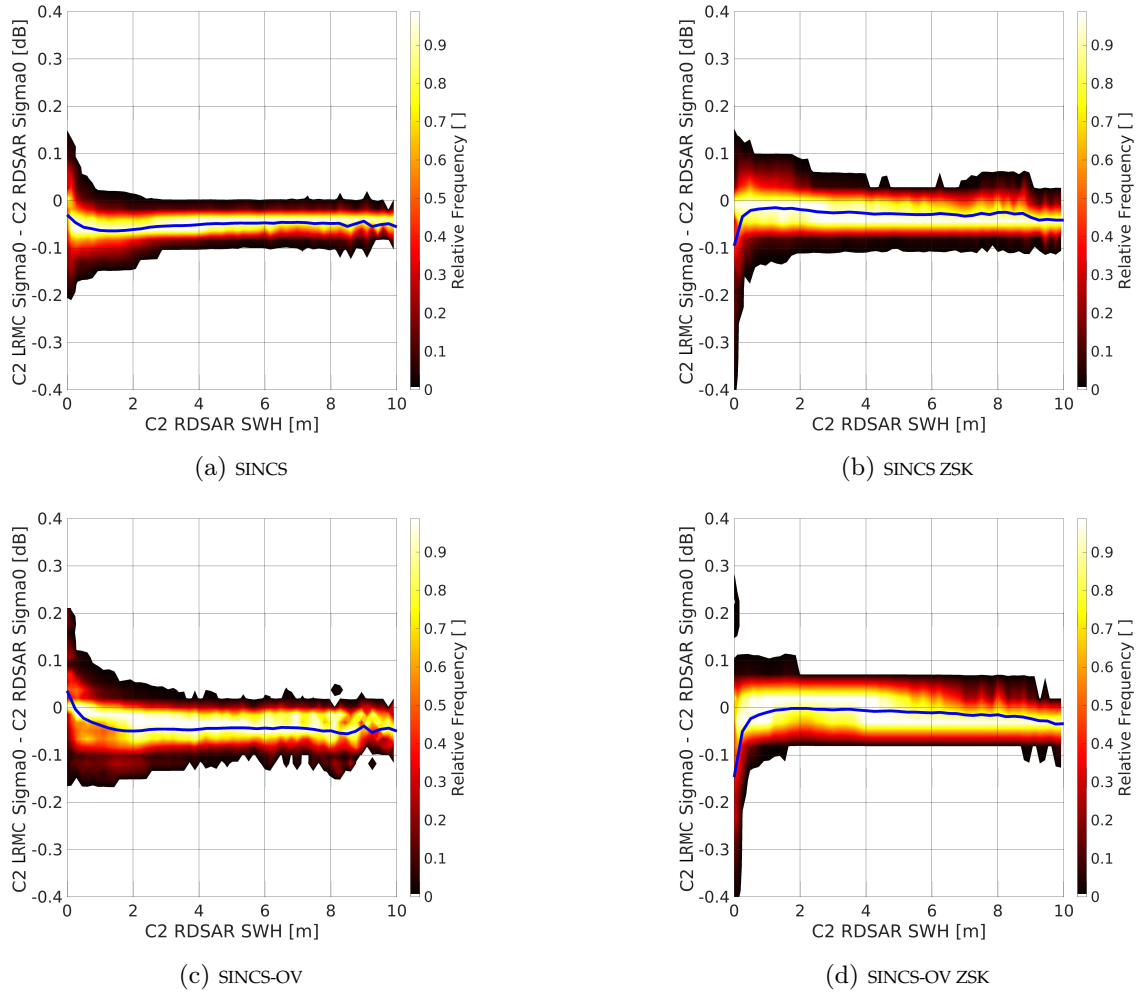

(a) SINCS

(b) SINCS ZSK

(c) SINCS-OV

(d) SINCS-OV ZSK

Figure 7.22: Two-dimensional histogram of differences between LRMC and RDSAR σ_0 values with respect to RDSAR SWH.

7.3 Validation against the ECMWF Wave Model

This section shows the cross comparison results between radar altimetry data and the ECMWF wave model. The parameters of interest in this section are SWH (section 7.3.1) and σ_v (section 7.3.2). Of course, it would be possible to perform a comparison of T_{02}, which is the parameter given by the ECMWF model. However, the computation of this value includes a division between SWH and σ_v, which would result in a poor precision of altimeter-retrieved mean zero up-crossing period values due to the retracker noise. To overcome this issue, σ_v is calculated by computing $\sigma_v = \frac{\pi}{2}\frac{H_s}{T_{02}}$ (see table 2.2) for the ECMWF wave model as these values are noise-free. All figures in this chapter follow the same structure as in section 7.2.

7.3.1 Cross Comparison between ECMWF and Altimetry-Retrieved SWH

The first considered model parameter is the SWH. A first impression about how the modelled SWH behaves compared with values retrieved by radar altimetry was given in Figure 7.15. It was shown there that the histograms of RDSAR and ECMWF are similar, whereby differences could be observed depending on the SAR or LRMC retracker chosen. This subsection shows the accuracy of estimated SWH values compared with modelled data. As the ECMWF wave model and altimetry SWH values show large mean differences of up to more than one metre for wave heights greater than six metre, only SWH results below six metres are discussed.

Accuracy of SWH with respect to the ECMWF Wave Model

Figure 7.23 shows the two-dimensional histogram of differences between RDSAR and ECMWF SWH data with respect to RDSAR SWH. Where the blue curves shown in Figure 7.23 a) and b) showing the mean differences between the model and SINC2 or SINC2 ZSK are comparable, it can be observed that the differences scatter less for Figure 7.23 b), which can be explained by the smaller standard deviation of SINC2 ZSK compared with SINC2. For SWH smaller than four metres and larger than 0.5 metres the model and the altimeter data are consistent, with mean differences between -10 cm and 10 cm. For lower or higher sea states the overall accuracy is poor due to the large mean differences up to one metre.

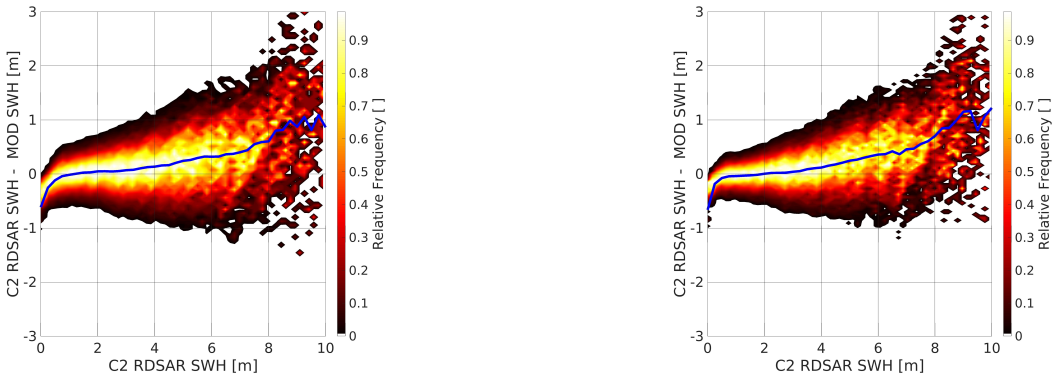

(a) SINC2 (b) SINC2 ZSK

Figure 7.23: Two-dimensional histogram of differences between ECMWF and RDSAR SWH with respect to RDSAR SWH.

Figure 7.24 shows the accuracy of retrieved SAR SWH values with respect to the ECMWF results. It can be observed that each SAR retracker shows different results. For SINCS shown in Figure 7.16 a), a sea state-dependent mean difference is observable, varying from 0 cm at SWH of around one metre up to 50 cm for SWH of about six metres.

If a variable transformation according to Eq. 7.1 is applied in the L1B processing, the precision becomes much better observable due to the narrower histogram in the y direction. However, on the other hand the mean differences (blue curve) becomes larger, varying from zero at SWH around one metre up to 70 cm for SWH of about six metres. This means that the consistency worsens.

For SINCS-OV shown in Figure 7.24 c), the precision at SWH larger than two metres is comparable with Figure 7.24 a), although in the SWH interval between zero and six metres this retracker shows the best agreement, with mean differences below a few centimetres.

On the other hand, Figure 7.24 d) showing the differences between the wave model and SINCS-OV ZSK gives large mean differences of up to 90 cm for SWH smaller than two metres, whereas for higher sea state the mean differences are comparable with those derived by SINCS and SINCS ZSK.

It can be concluded form Figure 7.24 that the overall agreement between the ECMWF wave model and altimeter-derived SWH values is poor for high sea states. However, within an interval of zero to six metres SINCS-OV has the best consistency with respect to the wave model.

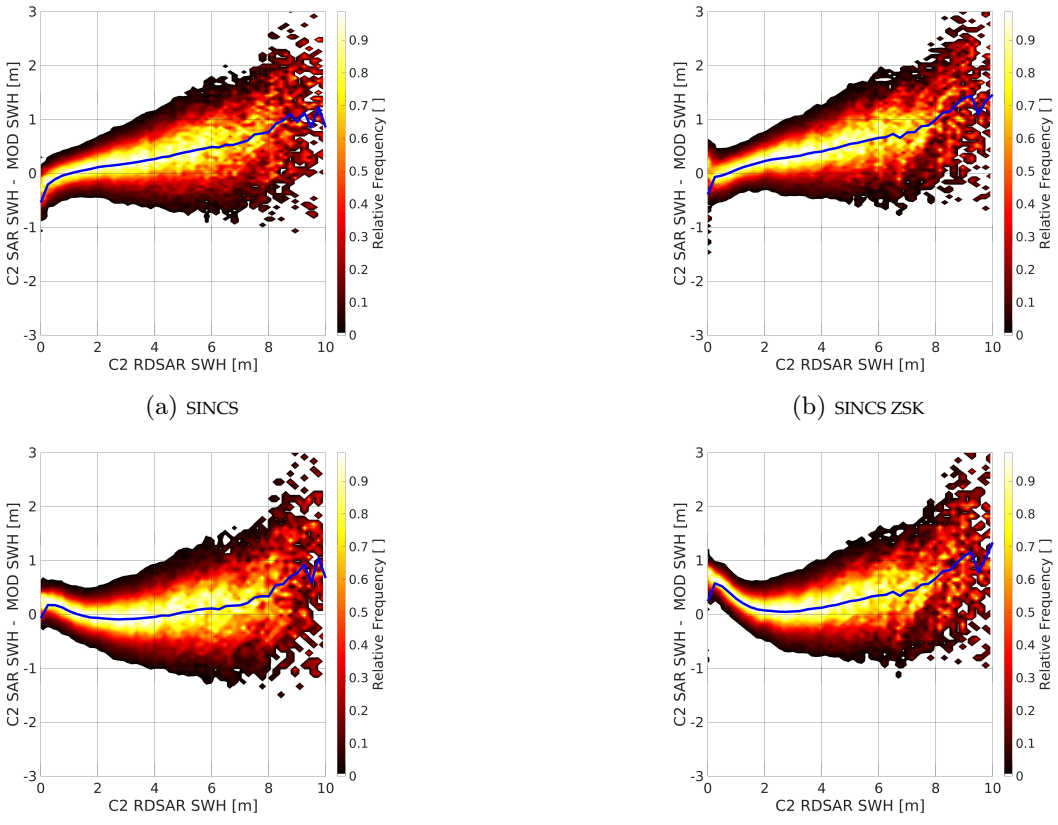

(a) SINCS (b) SINCS ZSK

(c) SINCS-OV (d) SINCS-OV ZSK

Figure 7.24: Two-dimensional histogram of differences between ECMWF and SAR SWH with respect to RDSAR SWH.

For LRMC, the plots shown in Figure 7.25 are similar to Figure 7.24 at SWH larger than two metres. Additionally, SINCS and SINCS ZSK show the same behaviour at small sea states as in Figure 7.17.

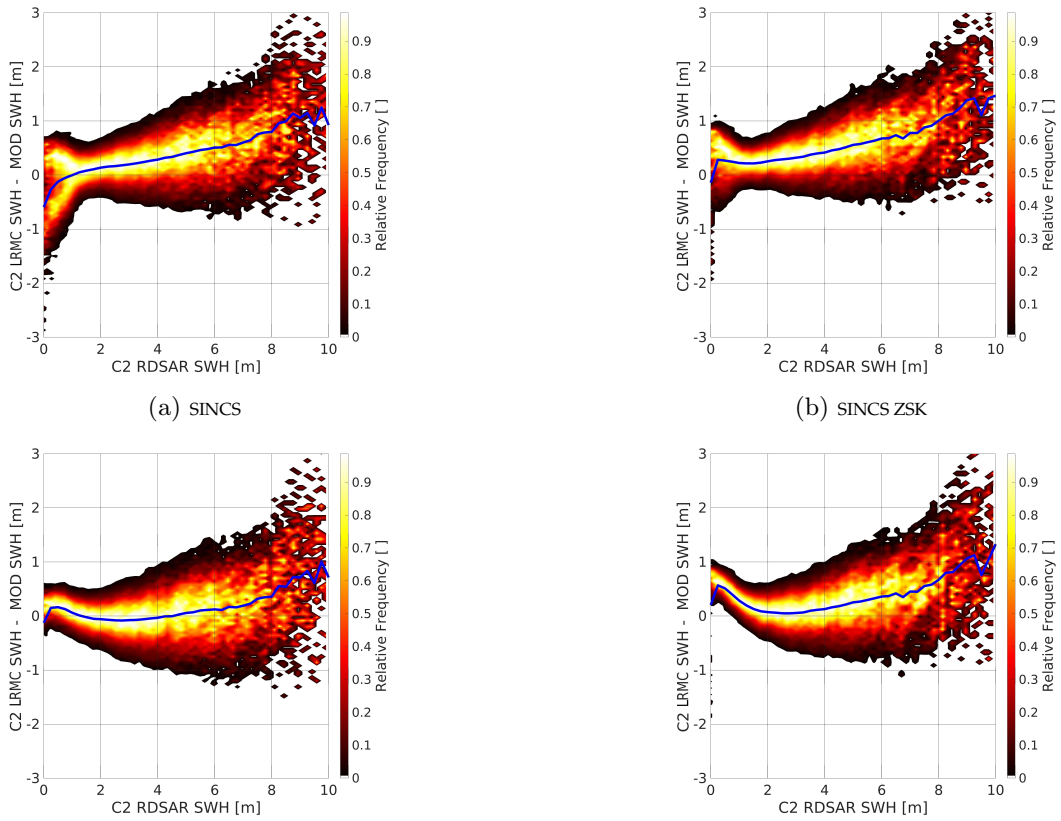

(a) SINCS (b) SINCS ZSK

(c) SINCS-OV (d) SINCS-OV ZSK

Figure 7.25: Two-dimensional histogram of differences of ECMWF and LRMC SWH with respect to RDSAR SWH.

7.3.2 Cross Comparison between ECMWF and Altimetry-Retrieved σ_v

Figure 7.26 provides an overview of the range of occurring σ_v values, which vary between zero and two metres per second in the NEA. It is observable that the SICNS-OV histogram follows well the modelled data. Both SAR and LRMC show the same behaviour in Figure 7.26 a). However, SINCS-OV ZSK shown in plot b) gives a different result as the histograms are narrower than those of the model and differences between SAR and LRMC are observable.

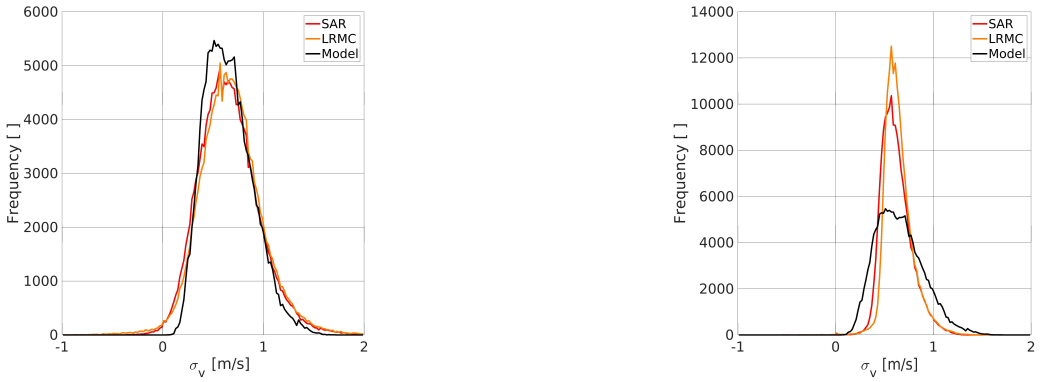

(a) SINCS-OV (b) SINCS-OV ZSK

Figure 7.26: Histogram of occurring σ_v values in the NEA for stack retrackers.

In Figure 7.27, the scattering and the mean of differences between SAR and ECMWF σ_v values are shown for SINCS-OV and SINCS-OV ZSK, giving different results. Whereas in Figure 7.27 a) the differences strongly scatter compared with the range of σ_v the mean differences are approximately zero. On the other hand, for SINCS-OV ZSK shown in Figure 7.27 b) the precision looks better due to the narrower histogram, although the blue curve shows a sea state dependency of the mean differences, which varies between -20 and 20 cm/s. This means that SINCS-OV gives the best results with repsect to trueness, whereas in terms of precision SINCS-OV ZSK is superior. Overall, no statement about which retracker is the best to estimate σ_v can be made for SAR mode.

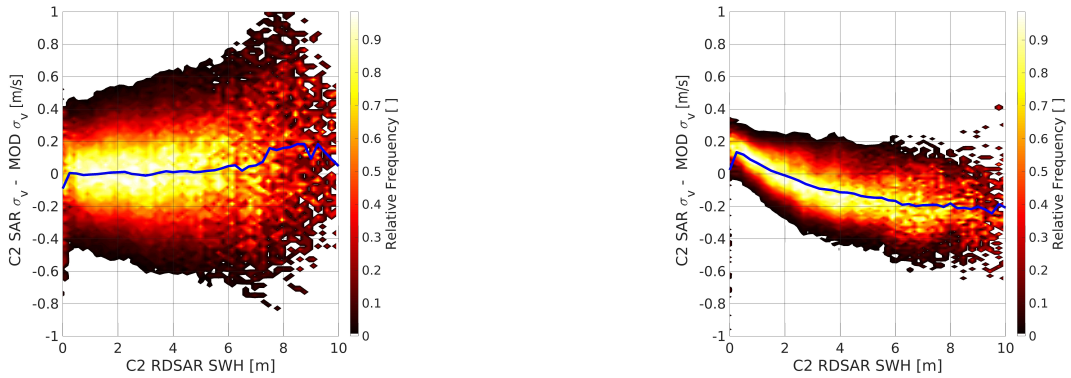

(a) SINCS-OV (b) SINCS-OV ZSK

Figure 7.27: Two-dimensional histogram of differences between ECMWF and SAR σ_v with respect to RDSAR SWH.

Regarding Figure 7.28 showing the differences between ECMWF and LRMC σ_v values, it can be stated that both retrackers behave as in the SAR mode. No significant differences occur, although Figure 7.26 b) showed disagreements between SAR and LRMC.

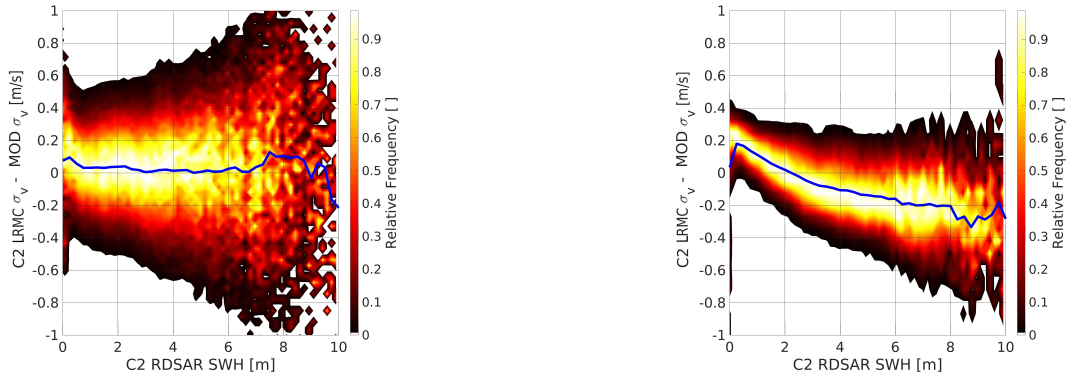

(a) SINCS-OV (b) SINCS-OV ZSK

Figure 7.28: Two-dimensional histogram of differences between ECMWF and LRMC σ_v with respect to RDSAR SWH.

Precision of σ_v

Figure 7.29 shows the empirical standard deviations of the retrieved 1 Hz σ_v SAR values. It can be observed that SINCS-OV (left plot) and SINCS-OV ZSK (right plot) produce different σ_v standard deviations, varying from 10 to 20 cm/s for SINCS-OV and 3 to 8 cm/s for SINCS-OV ZSK. This means that SAR σ_v benefits from the variable transformation, leading to more precise results.

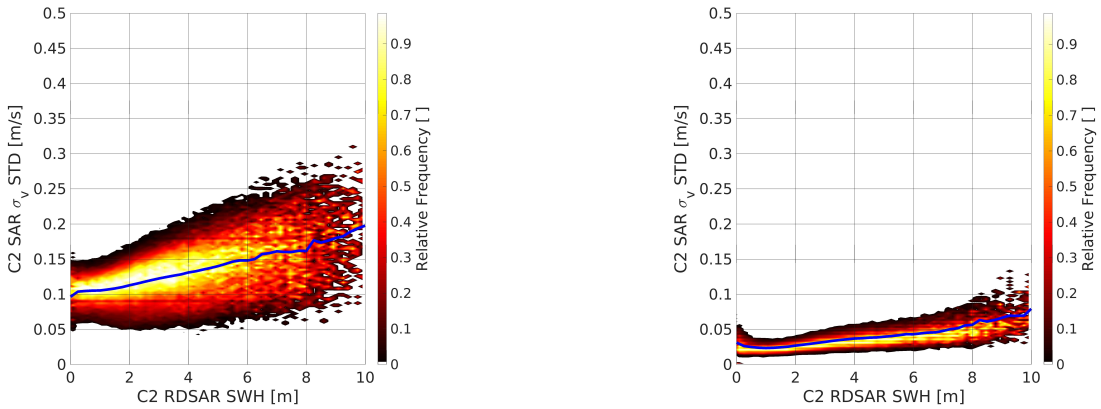

(a) SINCS-OV (b) SINCS-OV ZSK

Figure 7.29: Two-dimensional histogram of SAR σ_v standard deviations with respect to RDSAR SWH.

A similar result can be observed in Figure 7.30 showing the empirical standard deviations for LRMC values. It can be observed that LRMC standard deviations are smaller than those from SAR, varying from 8 to 18 cm/s for SINCS-OV and from 2 to 7 cm/s for SINCS-OV ZSK.

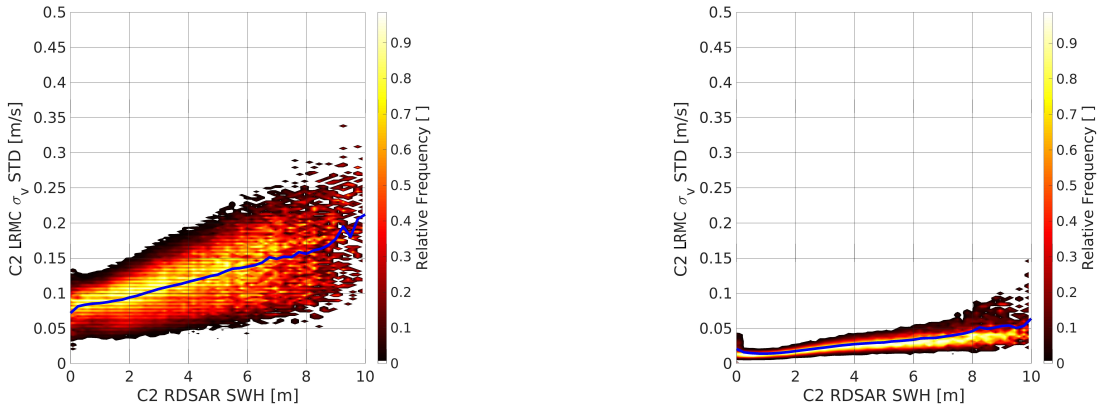

(a) SINCS-OV (b) SINCS-OV ZSK

Figure 7.30: Two-dimensional histogram of LRMC σ_v standard deviations with respect to RDSAR SWH.

However, from the results shown in Figure 7.26 b), it is known that σ_v estimates by SINCS-OV ZSK have a narrower range. Therefore, the standard deviation of Figure 7.30 b) are not representative and cannot be directly compared with SINC-OV.

Scatterplots of Altimetry-Retrieved σ_v Values with Respect to the ECMWF Wave Model

Figure 7.31 shows the scatterplots of retrieved SAR σ_v values with respect to ECMWF σ_v. In Figure 7.31 a), the scatterplot between SINCS-OV and ECMWF σ_v values is shown. It can be observed that the consistency between the two datasets is not good due to a regression slope of 0.567 and a empirical correlation coefficient of 0.686, although it can be stated that a relationship exists between these. The standard deviation of the differences is 21.8 cm/s, with a bias of 0.8 cm/s.

By observing Figure 7.31 b), a different behaviour can be seen. Even for SINCS-OV ZSK, with 1.426 the regression slope is not good, although the correlation coefficient is higher compared with SINCS-OV of 0.864. With 3.2 cm/s the mean difference is higher but more precise, with a standard deviation of 13.3 cm/s compared with 22.8 cm/s for SINCS-OV.

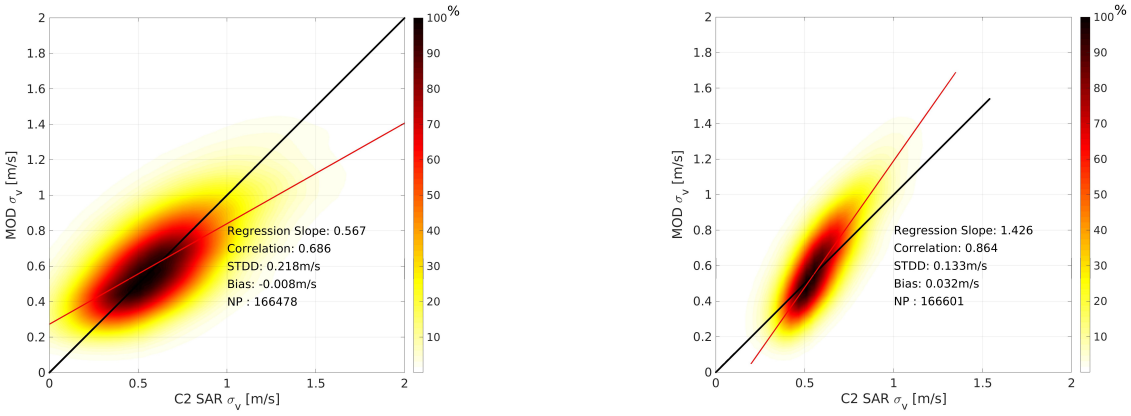

(a) SINCS-OV (b) SINCS-OV ZSK

Figure 7.31: Scatterplots of SAR and ECMWF σ_v and their statistical parameters.

For LRMC, the statistical parameters shown in Figure 7.32 are slightly worse compared with SAR but have comparable magnitudes. Accordingly, this leads to the assumption that LRMC and SAR produce consistent σ_v values.

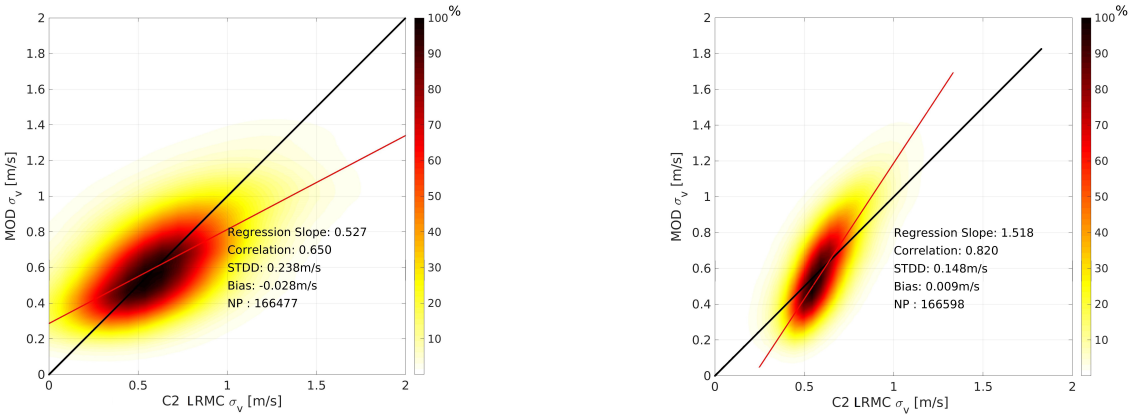

(a) SINCS-OV (b) SINCS-OV ZSK

Figure 7.32: Scatterplots of LRMC and ECMWF σ_v and their statistical parameters.

The object of this chapter is to compare the geophysical parameters retrieved by different processing modes and retrackers with respect to precise reference measurements. In this study, sea state parameters measured at the FINO1 scientific station (see Figure 7.33 red diamond) by using an Acoustic Doppler Current Profiler (ACDP) of AWAC type. The observed statistical measures are averaged over twenty minutes to retrieve representative values. The estimated sea level anomalies are compared with tide gauge water levels measured at Helgoland-Binnenhafen (see green triangle in Figure 7.33). As no Global Navigation Satellity System (GNSS) height of the reference level at the tide gauge Helgoland was available, an absolute calibration cannot be performed, although a relative comparison is possible.

Figure 7.33 shows the German bight as the region of interest of the in-situ validation, which is part of the NEA box. The altimeter data used in this study is CryoSat-2 Full Bit Rate (FBR) data located during the time interval from July 2010 to May 2018.

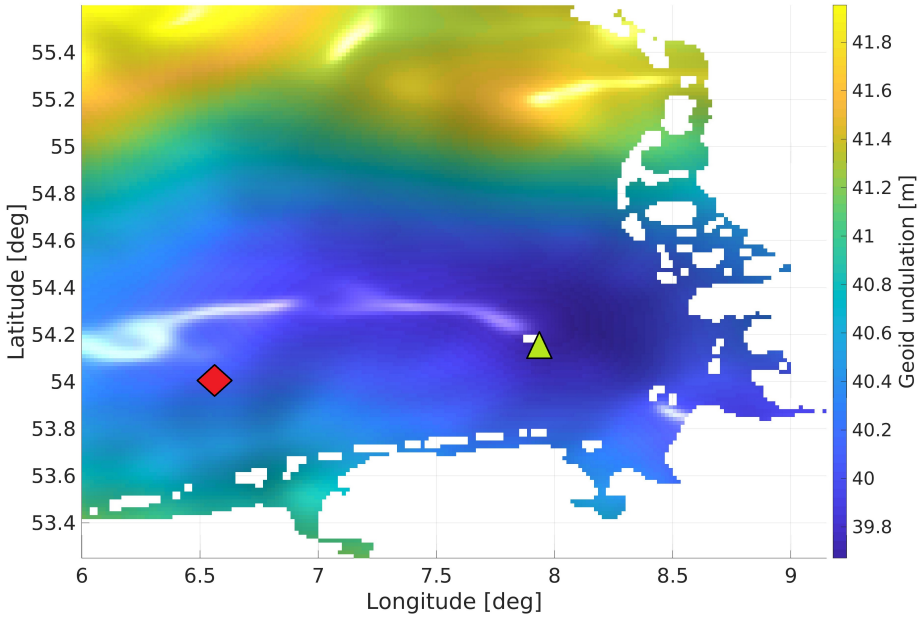

Figure 7.33: Geoid undulations in the German bight. The red diamond denotes the location of the FINO1 scientific station and the green triangle the location of the tide gauge Helgoland-Binnenhafen.

The data criteria used to decide whether a value from the altimeter or reference dataset are considered are applied by the following steps, which were adapted from Fenoglio-Marc et al. [2015].

1. For each altimeter track, find the closest point to the tide gauge or scientific station and ignore all 1 Hz surface locations with distance to the station of smaller than ten kilometres.

2. Find the closest remaining 1 Hz surface location and keep it if its distance to the station is smaller than twenty kilometres.

3. Interpolate the tide gauge or scientific platform time series to the epoch corresponding to the closest 1 Hz surface location.

4. Store both of the geophysical parameters from the station and the altimeter if the closest epoch in the station time series with respect to the altimeter data point is less than thirty minutes away.

7.4.1 Cross Comparison of Altimeter Retrieved and Tide Gauge Measured SLA$_i$ Values

According to Fenoglio-Marc et al. [2015, Eq. 5], the sea level parameter compared with tide gauges SLA_i is defined similar to Eq. 4.1 as

$$SLA_i = h_s - (R - \Delta R) - \Delta h_{app} - h_{mss} \tag{7.3}$$

with Δh_{app} being the height correction due to geophysical and atmospherical measures affecting both the altimeter retrieved sea level and the tide gauge, defined as

$$\Delta h_{app} = \Delta h_{iono} + \Delta h_{dry} + \Delta h_{wet} + \Delta h_{set} + 0.468\Delta h_{pole} + \Delta h_{load} + \Delta h_{ssb} \tag{7.4}$$

with Δh_{iono} the ionospheric correction, Δh_{dry} the dry tropospheric correction, Δh_{wet} the wet tropospheric correction, Δh_{set} the solid earth tide, Δh_{pole} the geocentric polar tide, Δh_{pole} the loading tide and Δh_{ssb} the sea state bias correction. In this study, the corrections mentioned in Eq. 7.4 were extracted from the CryoSat-2 FBR data, with the exception of the sea state bias, which is set to zero and therefore not applied.

In order to level the tide gauge measures closer to the altimeter data and mean sea level, an offset of 5.1 m is subtracted from the whole time series. The following figures show the scatterplots between altimetry-retrieved SLA_i values with respect to adjusted water levels derived at the Helgoland tide gauge, which is located at latitude 54.1750° North and longitude 7.9030° East. The time interval of the tide gauge data considered was from January 2010 to August 2018.

Figure 7.34 shows the comparison between valid RDSAR and tide gauge SLA_i values. It can be seen that SINC2 and SINC2 ZSK have a similar agreement with the tide gauge water levels. In both cases, the slope is approximately one, which is a good result and the standard deviation of differences between tide gauge and altimeter data is circa 12 cm, which is more than in Fenoglio-Marc et al. [2015], who found a standard deviation of 6.6 cm. However, in Fenoglio-Marc et al. [2015] a sea state bias and only 18 points are considered, compared with the 85 used in this study. The main difference between Figure 7.34 a) and b) is that the mean difference with respect to SINC2 ZSK is smaller. This means that compared to SINC2 in average 1.2 cm smaller sea surface heights are estimated by SINC2 ZSK.

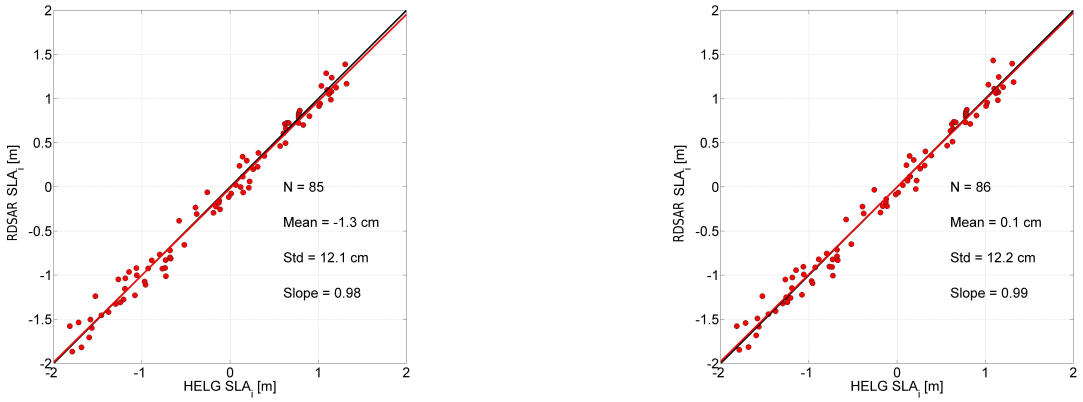

(a) SINC2 (b) SINC2 ZSK

Figure 7.34: Scatterplots of RDSAR and TG Helgoland SLA_i values and their statistical parameters.

The plots in Figure 7.35 show the comparison of SAR SLA_i values with tide gauge measurements. It can be observed that the regression slope for all retrackers is approximately one, given that both datasets (Altimeter and tide gauge) are consistent. However, the results of the four retrackers differ with respect to mean and standard deviations.

Whereas differences of SINCS with the tide gauge shown in Figure 7.35 a) are on average 0.7 cm with SINCS ZSK, the mean is 0.2 cm. The standard deviations for these two retrackers is approximately the same. This means that SINCS ZSK estimated 0.5 cm smaller sea surface heights on average compared with SINCS.

The retracker including vertical wave particle velocities shown in Figure 7.35 c) and d) has higher mean values and standard deviations, whereas the mean differences with respect to tide gauge water levels are 1.8 cm for SINCS-OV and -1.9 cm for SINCS-OV ZSK. The standard deviations are 1 cm larger compared with the corresponding retracker that does not include vertical wave particle velocities. However, this does not mean that these retrackers are overall worse as in the German bight the SWH is smaller than two metres in most cases (see subsection 7.4.2), which is the interval at which the vertical wave particle velocity retrackers do not perform well.

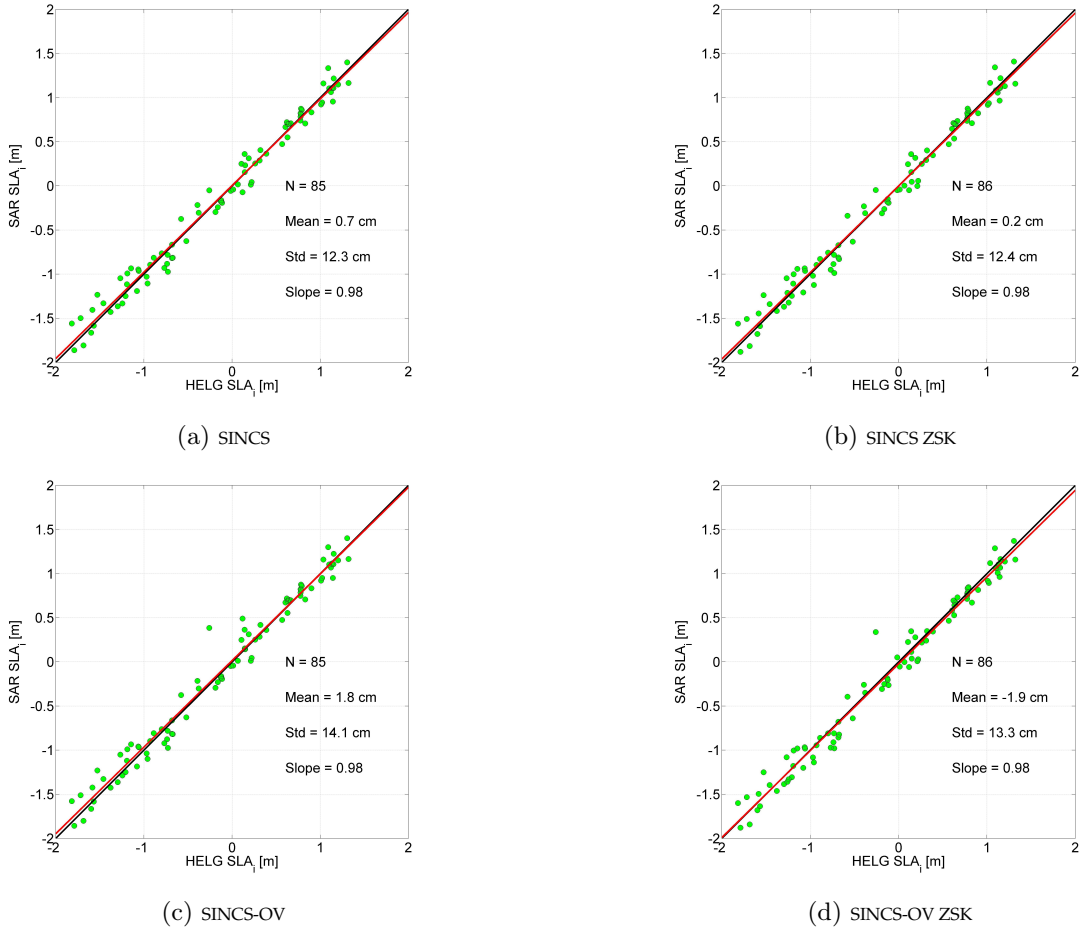

(a) SINCS

(b) SINCS ZSK

(c) SINCS-OV

(d) SINCS-OV ZSK

Figure 7.35: Scatterplots of SAR and TG Helgoland SLA_i values and their statistical parameters.

The plots in Figure 7.36 show the comparison of LRMC SLA_i values with tide gauge measurements. The regression slope for all retrackers is approximately one indicating that the two datasets (Altimeter and tide gauge) are consistent. However, even for LRMC the results of the four retrackers differ with respect to mean and standard deviations.

Whereas differences of SINCS with the tide gauge shown in Figure 7.36 a) are on average 0.7 cm with SINCS ZSK, the mean is -1.0 cm. The standard deviations for these two retrackers is approximately the same. This means that SINCS ZSK estimated 1.7 cm smaller sea surface heights on average compared with SINCS in the case of LRMC processing.

The retrackers including vertical wave particle velocities of scattering surface elements shown in Figure 7.36 c) and d) has similar mean values and standard deviations, whereas the mean differences with respect to tide gauge water-levels are 0.8 cm for SINCS-OV and -2.7 for SINCS-OV ZSK. The standard deviations are slightly smaller compared with the corresponding retracker that does not include vertical wave particle velocities. However, even in this case it needs to be considered that in the German bight the sea state is usually small, leading to SINCS-OV and SINCS-OV ZSK giving slightly worse results for SLA.

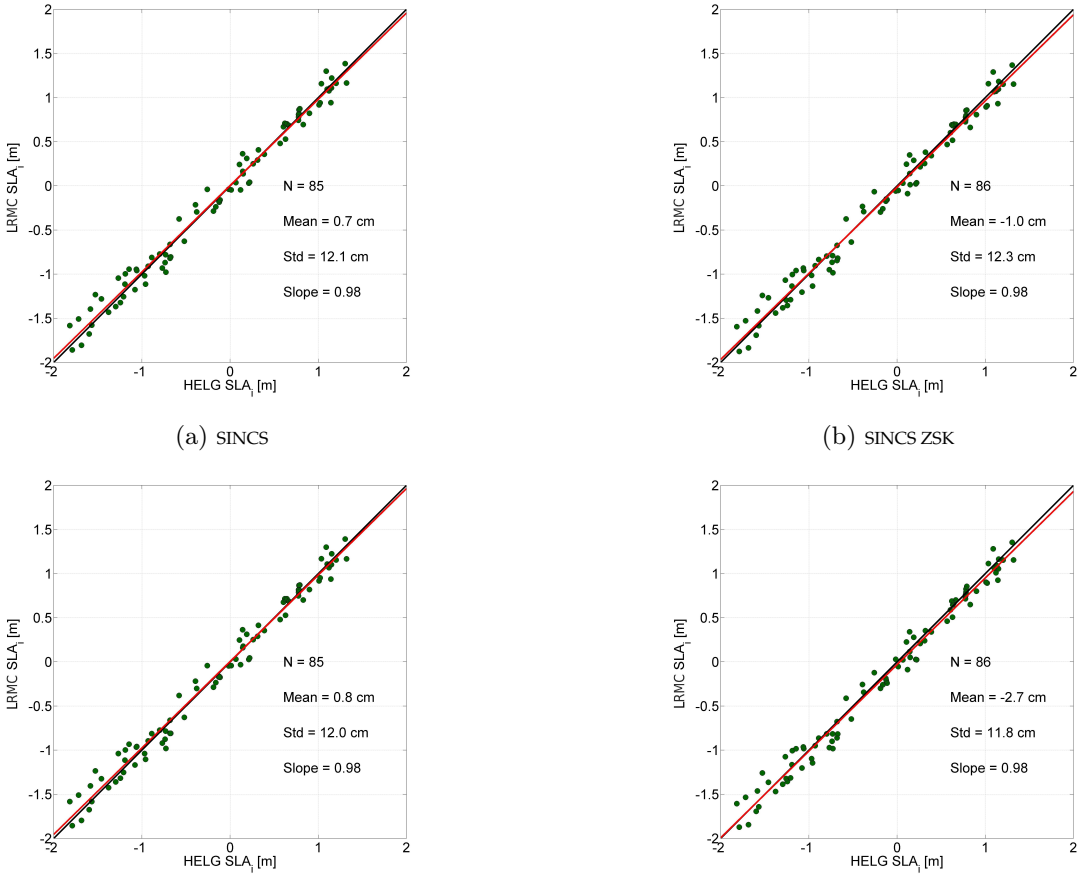

(a) SINCS (b) SINCS ZSK

(c) SINCS-OV (d) SINCS-OV ZSK

Figure 7.36: Scatterplots of LRMC and TG Helgoland SLA_i values and their statistical parameters.

7.4.2 Cross Comparison of Altimeter Retrieved and Buoy Measured SWH Values

The next considered geophysical parameter compared with respect to FINO1 sea state parameters is the SWH. The comparison is performed in the same way as for the water level, with the difference that the buoy data does not need to be adapted. This means that when altimetry data is compared with respect to sea state parameters such as SWH or wave periods, a statement about absolute biases can be made. FINO1 is located at latitude 54.014832437° North and longitude 6.587758232° East. FINO1 data from January 2010 to December 2015 is used in this study.

In Figure 7.37, the cross comparison of FINO1 and RDSAR SWH values is shown. As previously discussed most of the SWH values are below two metres, which will make it difficult to validate the new SAR and LRMC retracker, which works well at higher sea states but is probably poor in the given range of SWH. However, the comparison can still be helpful to evaluate the potential of these retrackers.

By comparing the different statistical parameters of the cross-comparison between FINO1 and the different RDSAR retrackers, it can be observed that SINC2 ZSK shows the best agreement with the buoy measured SWH values. The mean difference reduces from 9.3 cm to 2.9 cm, which means that if the variable transform described in Eq. 7.1 is applied, the estimated SWH values are 6.4 cm smaller compared with SINC2 without the transformation. Additionally, with 14.6 cm, the standard deviation of differences between FINO1 and SINC2 ZSK is around 5.7 cm smaller than for SINC2. Moreover, the regression slope is slightly closer to one, which means that the agreement between SINC2 ZSK and FINO1 SWH is better. This means that overall SINC2 ZSK outperforms SINC2 with respect to SWH accuracy, giving the best agreement with FINO1 data.

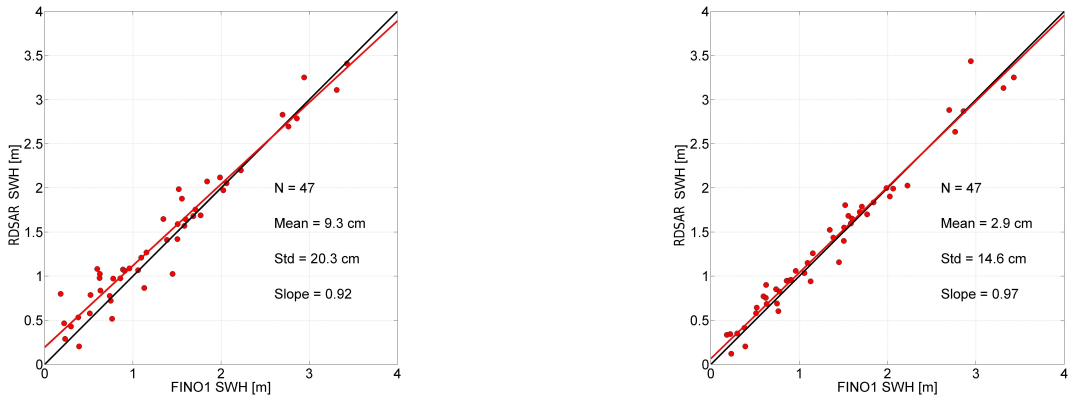

(a) SINC2 (b) SINC2 ZSK

Figure 7.37: Scatterplots of RDSAR and FINO1 SWH values and their statistical parameters.

Compared with the RDSAR SWH results in SAR mode shown in Figure 7.38, the agreement with the buoy data worsens. In Figure 7.38 a) showing the comparison between FINO1 and SINCS, it is observable that for SWH values smaller than two metres the consistency between these two datasets is good, whereas for higher sea states it gets worse. However, with 1.05, the regression slope is quite close to one and the standard deviation of difference is 16.2 with a mean difference of 6.9 cm. Overall, the agreement between SINCS and FINO1 is good.

However, as in the cross comparison with SINC2 ZSK, SINCS ZSK overestimates SWH values compared with FINO1, which results in a higher regression slope of 1.08 and a larger mean difference of 15.8 cm and a worse precision of 17.5 cm standard deviation compared with SINCS. That results in a worse agreement than SINCS.

In Figure 7.38 c), the scatter plot of SINCS-OV SWH values with FINO1 is shown. It can be observed that for SWH values smaller than two metres SINCS-OV overestimates this parameter and values smaller than 0.5 m are not estimated. For higher sea states, this retracker underestimates the SWH compared to FINO1 values. Of course, this leads to worse statistical parameters compared with SINCS or SINCS ZSK.

The results for SINCS-OV ZSK given by Figure 7.38 d) show that the disagreement with respect to FINO increases at SWH values smaller than two metres. Additionally, SINCS-OV ZSK is unable to estimate SWH values smaller than 0.8 m. However, at higher sea states the agreement is better, although given that the statistical parameters are calculated with the whole data population SINCS-OV ZSK has the worst mean, standard deviation and regression slope parameters.

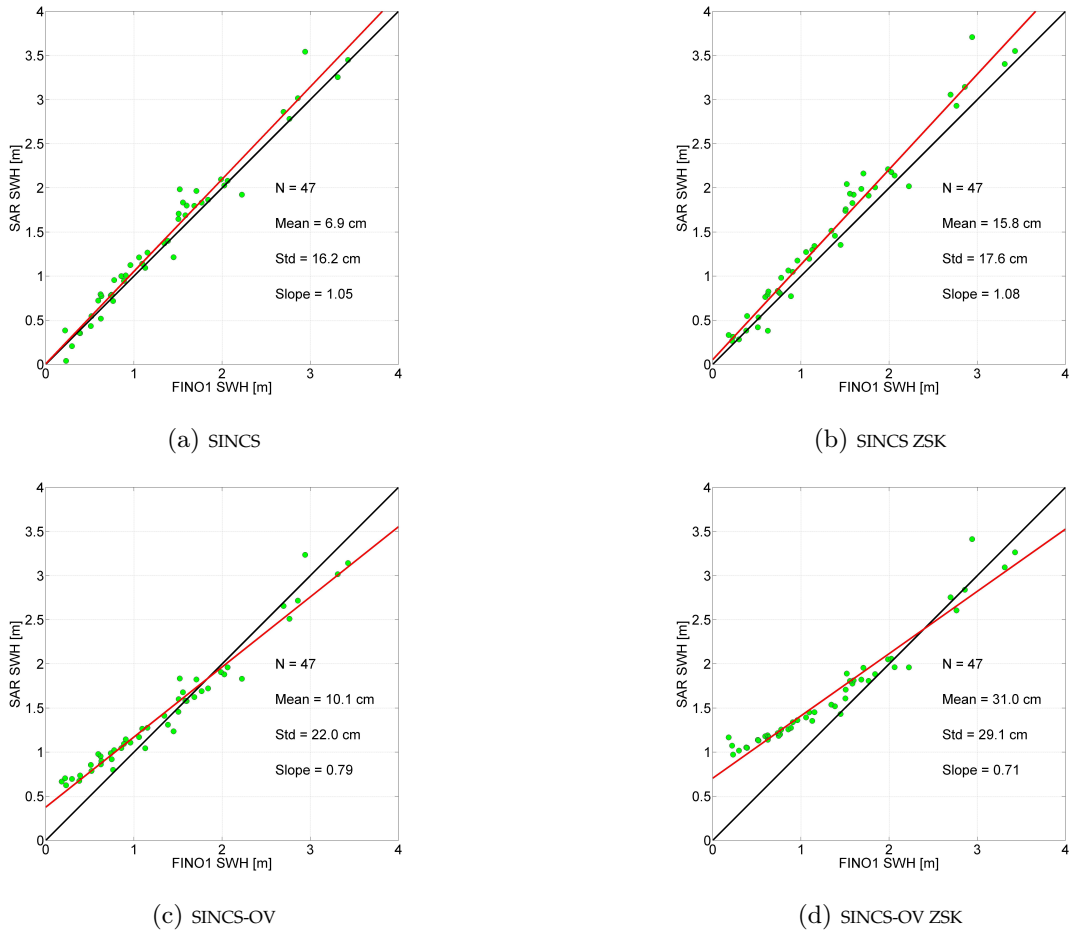

(a) SINCS (b) SINCS ZSK

(c) SINCS-OV (d) SINCS-OV ZSK

Figure 7.38: Scatterplots of SAR and FINO1 SWH values and their statistical parameters.

In the case of LRMC processing, SINCS-OV and SINCS-OV ZSK shown in Figure 7.39 c) and d) yield consistent results compared with SAR processing with approximately equal statistical properties. However, for the other two retrackers this does not apply.

In the case of SINCS shown in Figure 7.38 a), a higher scattering of the data at small SWH can be observed, leading to an overall higher standard deviation of 32.5 cm compared with 16.2 cm in SAR mode. When the distribution of the altimeter L1B LRMC data was additionally changed to symmetric Weibull with Eq. 7.1, it can be observed in Figure 7.38 b) that this retracker overestimates SWH even at small sea states, leading to a bias of 30.6 cm. In this case, the standard deviation of the differences with FINO1 and the regression slope are comparable to SINCS SAR.

At this point, it is difficult to explain this phenomena. One possible effect that can cause significant SWH differences in the LRMC mode was discussed in chapter 6, namely sea surface slopes. It might be possible that time-varying effects such as tides or the dynamic atmosphere cause sea surface slopes close to the FINO1 platform, which can lead to higher differences in LRMC SWH estimations with respect to FINO1. Another possible issue might be that the water depth at FINO1 is about thirty meters, which leads to wave sea floor interactions causing steeper waves. However, this needs to be investigated and proven in a further study.

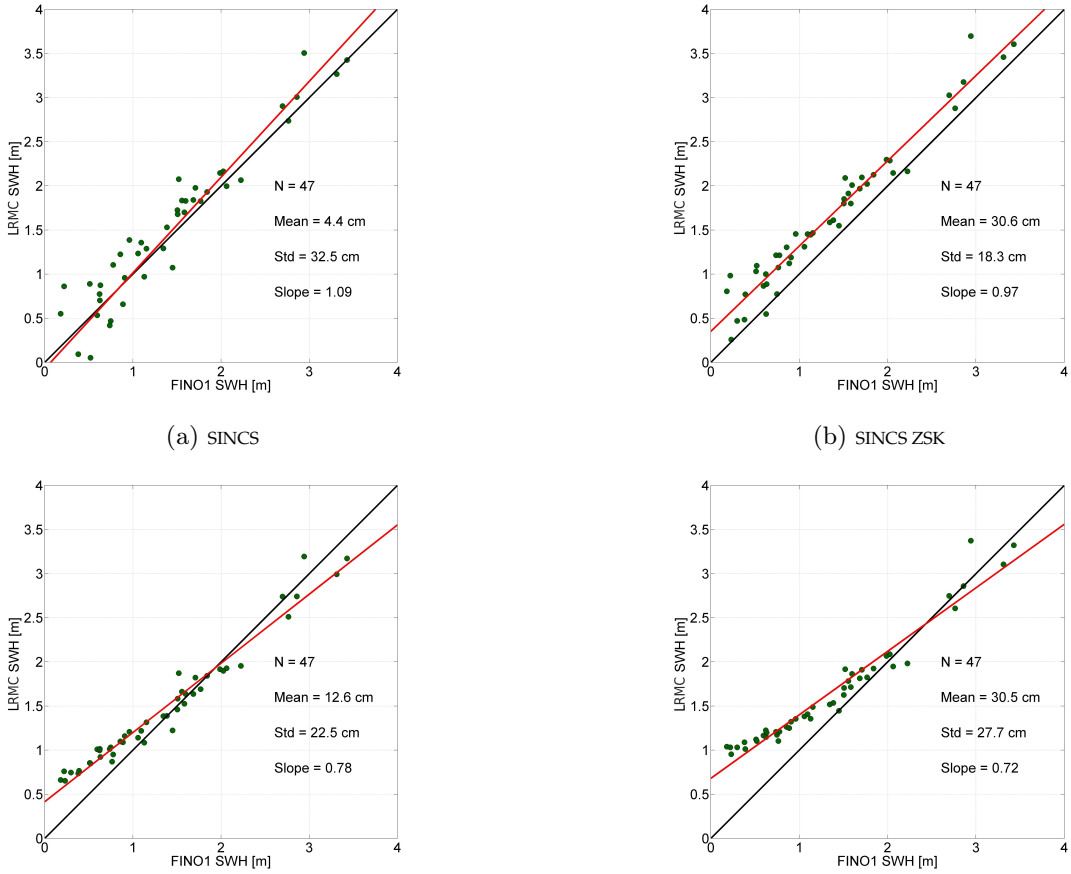

(a) SINCS (b) SINCS ZSK

(c) SINCS-OV (d) SINCS-OV ZSK

Figure 7.39: Scatterplots of LRMC and FINO1 SWH values and their statistical parameters.

7.4.3 Cross Comparison of Altimeter Retrieved and Buoy Measured σ_v Values

The next geophysical parameter to be compared to FINO1 data is the standard deviation of vertical wave particle velocities σ_v. As for the ECMWF model, this parameter needs to be calculated by $\sigma_v = \frac{\pi}{2}\frac{H_s}{T_{02}}$. As SINCS and SINCS ZSK do not estimate this parameter, they are not mentioned in these subsection. The same applies for RDSAR.

Figure 7.40 shows the comparison between FINO1 and SAR altimetry results. Whereas SINCS-OV agrees quite well with FINO1 but has a high standard deviation for SINCS-OV ZSK, the scattering is less but the regression slope of 0.45 is low. For SINCS-OV, the slope is 0.66, although this is probably caused by a few outliers, given that - as for LRMC - it is close to one. It can be seen that SINCS-OV ZSK is unable to estimate σ_v values smaller than 0.3 m/s.

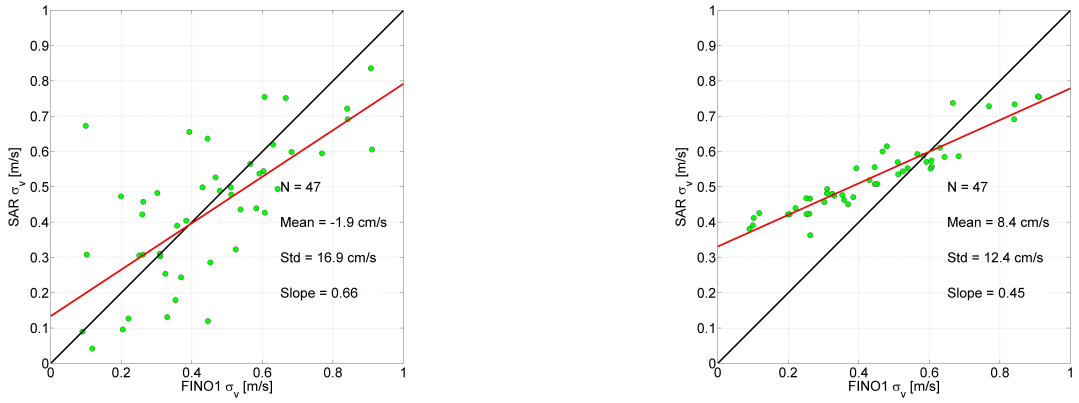

(a) SINCS-OV (b) SINCS-OV ZSK

Figure 7.40: Scatterplots of SAR and FINO1 σ_v values and their statistical parameters.

LRMC - shown in Figure 7.41 - gives similar results as SAR. However the overall precision of LRMC σ_v is better for SINCS-OV (14.6 cm/s) than in SAR (16.9 cm/s). Additionally, the regression slope is close to one with 0.95 and the mean difference is -4.6 cm/s, which is a very good agreement with the FINO1 values. However, in the case of transformed L1B products even LRMC is not capable of estimating values smaller than 0.3 cm/s.

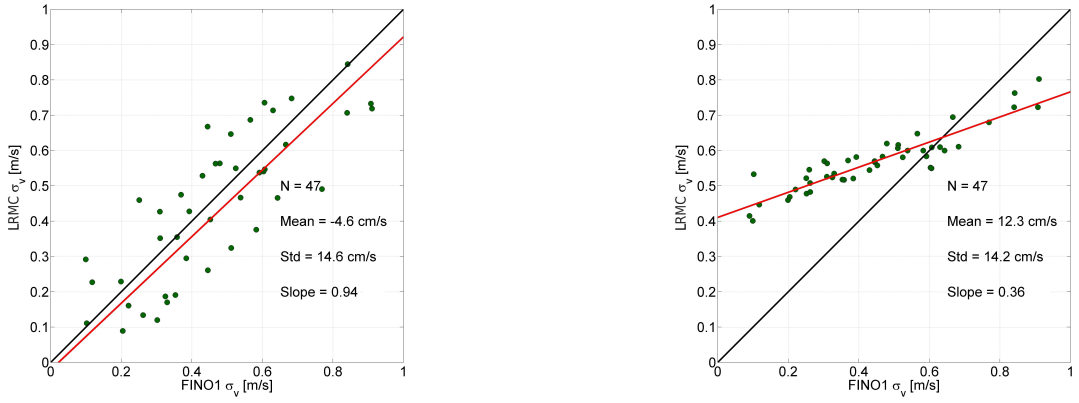

(a) SINCS-OV (b) SINCS-OV ZSK

Figure 7.41: Scatterplots of LRMC and FINO1 σ_v values and their statistical parameters.

It can be concluded that the first results of σ_v estimations look promising as a clear correlation with modelled and measured data is observable. However, further investigations are necessary to improve these results, especially for SINCS-OV ZSK.

In chapter 3, the fast convolution-based waveform model SINC developed in Buchhaupt et al. [2018] was extended to include general sea surface representations due to changing the reference coordinate system from a sphere to a torus, which also contributes to vertical wave particle motions on the sea surface.

In chapter 5, it was shown that 20 Hz sea surface sampling results in aliasing of the SAR processing mode, whereby a higher sampling rate leads to a better retrieval of geophysical signals at high frequencies and the overall precision of the averaged one Hertz parameters improves. On the other hand, LRMC and RDSAR does not benefit from 40 Hz sampling. In fact, the fewer considered pulses or beams in the multi-looking and averaging results in a worse accuracy and precision for these two processing modes.

Chapter 6 has shown that sea surface slopes and curvatures derived by spherical harmonics of the EIGEN-6C4 gravity model significantly affects the level 1B processing of LRMC waveforms or stacks as LRMC SWH estimations has differences with respect to RDSAR up to three metres, whereas the sea surface height differs between minus twenty and plus twenty centimetres. Additionally, has been shown that considering the geoid slopes only still results in curvature depending sea level errors between minus six and plus six centimetres in the area of the Marianna trench. On the other hand, if all of these quantities are considered correctly, LRMC produces consistent and precise geophysical parameters, which are more precise than SAR and RDSAR results in the open ocean. SAR and RDSAR are mainly affected by geoid slopes, leading to SLA differences between minus five and plus five millimetres and SWH differences between minus two and plus two centimetres. Additionally, it was discussed that differences between LRMC and unfocused SAR SWH and SSH values can be used to improve the determination of the mean sea surface as SSH differences are robust against atmospheric and sea state bias effects. Of course, this method needs to be refined by investigating a larger time span including several years and more regions needs to be included in the analysis. This shall be investigated in a future work as this study did not focus on mean sea level determination.

The estimation of vertical wave particle velocities was discussed in chapter 7, where it was shown that the whole stack needs to be considered in the retracking to distinguish between SWH and the standard deviations of these velocities. As a least square optimizer assumes normal distributed samples whereas the samples of the stack are exponentially distributed a variable transform was introduced to change the distribution to a symmetric Weibull distribution which is closer to the assumed normal distribution to reduce retracker biases. This transform is also applied to RDSAR pulses for the sake of consistency. In the cross validation with respect to RDSAR-derived geophysical parameters, it could be shown that including the vertical wave particle velocities in the retracker and applying the variable transform eliminates the mean differences for SLA and SWH estimations if the SWH is larger than two metres. For lower sea states, the inconsistency worsens as the new retracker is not capable of retrieving correct values at a low SWH. By comparing the standard deviations of vertical wave particle velocities with ECMWF, it could be observed that the correlation between these two datasets is high, whereas the overall accuracy is not good. This can also be concluded from the in-situ validation with FINO1 sea state parameters. However, it could be shown that the variable transforms significantly improves the performance of the retrieved geophysical parameters in RDSAR mode. The mean difference between RDSAR and SAR SLA reduces from two centimetres to zero centimetres at high waves, whereas the precision of SWH reduces for RDSAR from fifteen to eight centimetres after the transform. On the other hand, by comparing LRMC SWH with FINO1 SWH it was observed that the precision of this parameter is less than for SAR, which needs to be investigated in a further study. Overall, the retrieval of vertical wave particle velocities and SWH at low sea states needs to be improved. Possible influence factors that could result in a worse accuracy might the real antenna pattern - which was approximated as a Gaussian in this study - the aliasing caused by the lowpass filter - which was not considered here - or wave steepness, which was set to zero as this study focused on the open ocean. All of these factors shall be addressed in further studies.

Abdalla, S. (2012). Ku-Band Radar Altimeter Surface Wind Speed Algorithm. *Marine Geodesy*, 35(sup1):276–298.

Andersen, O., Stenseng, L., Piccioni, G., and Knudsen, P. (2016). The DTU15 MSS (Mean Sea Surface) and DTU15LAT (Lowest Astronomical Tide) reference surface. Poster at the ESA Living Planet Symposium 2016, Prague, Czech Republic.

Anderson, O., Rose, S. K., Knudsen, P., and Stenseng, L. (2018). The DTU18 MSS Mean Sea Surface improvement from SAR altimetry. Presented at GGHS meeting, September 2018, Copenhagen, Denmark.

Balanis, C. A. (2005). *Antenna Theory: Analysis and Design*. Wiley-Interscience, New York, NY, USA.

Banner, M. L. (1990). Equilibrium Spectra of Wind Waves. *Journal of Physical Oceanography*, 20(7):966–984.

Barrick, D. (1968). Rough Surface Scattering Based on the Specular Point Theory. *IEEE Transactions on Antennas and Propagation*, 16(4):449–454.

Bateman, H. (1954). *Table of Integral Transforms Volume 1*. McGRAW-HILL Book Company, INC, New York.

Bjerhammar, A. (1973). *Theory of errors and generalized matrix inverses*. Elsevier, Amsterdam.

Boy, F., Desjonquères, J., Picot, N., Moreau, T., and Raynal, M. (2017). CryoSat-2 SAR-Mode Over Oceans: Processing Methods, Global Assessment, and Benefits. *IEEE Transactions on Geoscience and Remote Sensing*, 55(1):148–158.

Brown, G. S. (1975). Reduced backscattering cross section (σ^0) data from the Skylab S-193 radar altimeter. Technical report, NASA-CR-141401.

Buchhaupt, C., Fenoglio-Marc, L., Dinardo, S., Scharroo, R., and Becker, M. (2018). A fast convolution based waveform model for conventional and unfocused SAR altimetry. *Advances in Space Research*, 62(6):1445 – 1463. The CryoSat Satellite Altimetry Mission: Eight Years of Scientific Exploitation.

Chelton, D. B., Ries, J. C., Haines, B. J., Fu, L.-L., and Callahan, P. S. (2001). Satellite Altimetry - Chapter 1. In Fu, L.-L. and Cazenave, A., editors, *Satellite Altimetry and Earth Sciences*, volume 69 of *International Geophysics*, pages 1 – 131. Academic Press.

Chelton, D. B., Walsh, E. J., and MacArthur, J. L. (1989). Pulse compression and sea level tracking in satellite altimetry. *Journal of Atmospheric and Oceanic Technology*, 6:407–438.

Cullen, R., Wingham, D., Viau, P., Francis, C., and Mavrocordatos, C. (2007). ESA's CryoSat-2 multi-mode level 0 to level 1B science processors - Algorithm design and pre-launch verification with ASIRAS. *Proc. 'Envisat Symposium 2007*.

Devore, J. L. (2011). *Probability and Statistics for Engineering and the Sciences*. Duxbury Press, Belmont, 8th edition.

Dinardo, S., Fenoglio-Marc, L., Buchhaupt, C., Becker, M., Scharroo, R., Fernandes, M. J., and Benveniste, J. (2018). Coastal SAR and PLRM altimetry in German Bight and West Baltic Sea. *Advances in Space Research*, 62(6):1371 – 1404. The CryoSat Satellite Altimetry Mission: Eight Years of Scientific Exploitation.

Egido, A. and Smith, W. H. F. (2016). Fully-Focused SAR Altimetry for Oceanographic Applications. *AGU Fall Meeting Abstracts*.

Fenoglio, L. and Buchhaupt, C. (2017). TB-RDSAR for GPOD. Technical report, Uni Bonn and TU Darmstadt.

Fenoglio-Marc, L., Dinardo, S., Scharroo, R., Roland, A., Sikiric, M. D., Lucas, B., Becker, M., Benveniste, J., and Weiss, R. (2015). The G erman Bight: A validation of CryoSat-2 altimeter data in SAR mode. *Advances in Space Research*, 55(11):2641 – 2656.

Fischer, J., Herklotz, K., Senet, C., Outzen, O., and Hahn, R. (2010). Oceanographic observations at FINO1 and the " alpha ventus " offshore wind farm. In *10th German Wind Energy Conference DEWEK 2010, At Bremen*.

Förste, C., Bruinsma, S., Abrikosov, O., Flechtner, F., Marty, J.-C., Lemoine, J.-M., Dahle, C., Neumayer, H., Barthelmes, F., König, R., and Biancale, R. (2014). EIGEN-6C4 - The latest combined global gravity field model including GOCE data up to degree and order 1949 of GFZ Potsdam and GRGS Toulouse. In *EGU General Assembly Conference Abstracts*, volume 16 of *EGU General Assembly Conference Abstracts*, page 3707.

Giles, K. A., Wingham, D. J., Galin, N., Cullen, R., and Smith, W. H. F. (2013). Precise estimate of ocean surface parameters from the CryoSat-2 synthetic aperture interferometric altimeter. *IEEE Transactions on Geoscience and Remote Sensing*.

Gradshteyn, I. S. and Ryzhik, I. M. (2007). *Table of integrals, series, and products*. Elsevier/Academic Press, Amsterdam, seventh edition. Translated from the Russian, Translation edited and with a preface by Alan Jeffrey and Daniel Zwillinger, With one CD-ROM (Windows, Macintosh and UNIX).

Hayne, G. S. (1980). Radar altimeter mean return waveforms from near-normal-incidence ocean surface scattering. *IEEE Transactions on Antennas and Propagation*, 28:687–692.

ISO 5725-1 (1994). Accuracy (trueness and precision) of measurement methods and results — Part 1: General principles and definitions. Standard, International Organization for Standardization, Geneva, CH.

Janssen, P. A. E. M. (2002). The wave model. *Meteorological Training Course Lecture Series*.

Jean-Raymond, B. (2016). Ocean wave model output parameters. Technical report, ECMWF.

Kitano, T., Mase, H., and Kioka, W. (2002). Theory of Significant Wave Period Based on Spectral Integrals. In *Fourth International Symposium on Ocean Wave Measurement and Analysis*, pages 414–423.

Klausing, H. and Holpp, W. (2000). *Radar mit realer und synthetischer Apertur: Konzeption und Realisierung*. Oldenbourg.

Kodis, R. (1966). A note on the theory of scattering from an irregular surface. *IEEE Transactions on Antennas and Propagation*, 14(1):77–82.

Kuga, H. and Carrara, V. (2013). Fortran-and C-codes for higher order and degree geopotential and derivatives computation. In *Anais XVI Simpósio Brasileiro de Sensoriamento Remoto - SBSR*.

Losch, M. and Seufer, V. (2003). How to Compute Geoid Undulations (Geoid Height Relative to a Given Reference Ellipsoid) from Spherical Harmonic Coefficients for Satellite Altimetry Applications.

Marquardt, D. W. (1963). An algorithm for least-squares estimation of nonlinear parameters. *SIAM Journal on Applied Mathematics*, 11(2):431–441.

Myrhaug, D. (2018). Some probabilistic properties of deep water wave steepness. *Oceanologia*, 60(2):187 – 192.

Papoulis, A. (1977). *Signal Analysis*. McGraw-Hill, New York.

Papoulis, A. and Pillai, S. U. (2002). *Probability, Random Variables, and Stochastic Processes*. McGraw Hill, Boston, fourth edition.

Patrikalakis, N. M. (2002). *Shape Interrogation for Computer Aided Design and Manufacturing*. Springer-Verlag, Berlin, Heidelberg.

Raney, R. K. (1998). The delay/Doppler radar altimeter. *IEEE Trans. Geoscience and Remote Sensing*, 36:1578–1588.

Ray, C., Martin-Puig, C., Clarizia, M. P., Ruffini, G., Dinardo, S., Gommenginger, C., and Benveniste, J. (2015). SAR Altimeter Backscattered Waveform Model. *IEEE Transactions on Geoscience and Remote Sensing*, 53:911–919.

Ray, C., Roca, M., Martin-Puig, C., Escolà, R., and Garcia, A. (2015). Amplitude and Dilation Compensation of the SAR Altimeter Backscattered Power. *IEEE Geoscience and Remote Sensing Letters*, 12(12):2473–2476.

Rosmorduc, V., Benveniste, J., Bronner, E., Dinardo, S., Lauret, O., Maheu, C., Milagro-Pérez, M., and Picot, N. (2016). Radar Altimetry Tutorial.

Sandwell, D. T. and Smith, W. H. F. (2014). Slope correction for ocean radar altimetry. *Journal of Geodesy*, 88(8):765–771.

Scagliola, M. and Fornari, M. (2016). Cryosat Characterization for FBR users. Technical report, Aresys.

Skolnik, M. (2008). *Radar Handbook, Third Edition*. Electronics electrical engineering. McGraw-Hill Education.

Smith, W. H. F. (2011). Notes on the "Walsh limit". Unpublished, personal communication with Remko Scharroo.

Smith, W. H. F. and Scharroo, R. (2015). Waveform Aliasing in Satellite Radar Altimetry. *IEEE Transactions on Geoscience and Remote Sensing*, 53(4):1671–1682.

Socquet-Juglard, H., Dysthe, K., Trulsen, K., Krogstad, H. E., and Liu, J. (2005). Probability distributions of surface gravity waves during spectral changes. *Journal of Fluid Mechanics*, 542:195–216.

Su, P. and Drysdale, R. L. S. (1997). A comparison of sequential Delaunay triangulation algorithms. *Computational Geometry*, 7(5):361 – 385. 11th ACM Symposium on Computational Geometry.

Trujillo, A. P. and Thurman, H. V. (2010). *Essentials of oceanography*. Prentice Hall, Boston, 10th edition.

Walsh, E. J. (1982). Pulse-to-pulse correlation in satellite radar altimeters. *Radio Science*, 17:786–800.

Weisstein, E. W. (2019). Exponential distribution. From MathWorld—A Wolfram Web Resource. Last visited on 19/8/2019.

Wessel, P. and Smith, W. H. F. (1996). A global, self-consistent, hierarchical, high-resolution shoreline database. *Journal of Geophysical Research: Solid Earth*, 101:8741–8743.